ELECTROSTATIC AND PIEZOELECTRIC MICRO ENERGY HARVESTERS FOR ENVIRONMENTAL VIBRATIONAL ENERGY SCAVENGING

by

YI LI

Presented to the Faculty of the Graduate School of

The University of Texas at Arlington in Partial Fulfillment

of the Requirements

for the Degree of

DOCTOR OF PHILOSOPHY

THE UNIVERSITY OF TEXAS AT ARLINGTON

December 2015

Acknowledgements

I would express my deepest appreciation to my advisor, Dr. Zeynep Celik-Butler who continuously guides and supports me during my whole Ph.D. study. Her insightful guidance and ability to access the key of problem helps me overcome many difficulties and in the end makes this dissertation possible. Her encouragement and faith in me means a world to me. I would also place my sincere gratitude to Dr. Donald Butler for his valuable comments and suggestions. His broad and solid knowledge always inspires me. I gained a lot from his devotion to teaching, willingness to encourage and help students unconditionally when I work as undergraduate teaching assistant for him.

I would like to take this opportunity to thank my graduate committee members, Dr. J. C. Chiao, Dr. Samir Iqbal, and Dr. Dereje Agonafer. They provide valuable suggestions not only for my dissertation, but also worthy courses which help to build foundation of my knowledge system. Especially I would thank Dr. J. C. Chiao for nominating me GTA award of electrical engineering department as recognition for my undergraduate teaching assistant work.

I also thank my many friends and colleagues from NanoFAB staff members or my research group. Especially Dr. Nader Hozhabri, Richard Chambers, Dennis Bueno, Paul Logan, Bhargav Nabar, Mohamed Nour, Md Sajeeb Rayhan, Md Sohel Mahmood. I am so thankful that I can always receive your unselfish help whenever I need it. Every discussion will stay as inerasable memory of my life.

I am also grateful to my parents: Youcai Li, Chunlan Liu, my husband Guoliang Chen and my sister Xi Li. You are the sources of my energy and confidence to fight through this long and uneasy journey.

October 27, 2015

Abstract

ELECTROSTATIC AND PIEZOELECTRIC MICRO ENERGY HARVESTER

Yi Li, PhD

The University of Texas at Arlington, 2015

Supervising Professor: Zeynep Celik-Butler

Nowadays wireless sensors are widely used in all kinds of fields such as biomedical, commercial and military. Micro energy harvesters converting the wasteful energy from environment into electricity enable the possibility of self-powered wireless sensor systems. This dissertation aims to develop micro energy harvesters to harness wasted mechanical vibrational energy.

An electrostatic micro energy scavenger was designed to incorporate MEMS comb-drive in-plane overlap as well as in-plane gap closing topologies into one hybrid structure. The device geometry and dimensions were optimized to maximize the energy harvesting efficiency. UV-LIGA process combined with nickel electroplating was utilized to fabricate the devices. A shaker platform in conjunction with a calibrated accelerometer was used to measure the harvested AC voltage with varying acceleration. A peak to peak value of 0.800 V was generated under an external acceleration magnitude of 78.4 m/s^2 at a vibration frequency of 1.90 kHz. The electromechanical simulations agreed with the measured data.

Design, fabrication and characterization of a piezoelectric zinc oxide nanowire (ZnO NW) micro energy generator was performed. Low temperature hydrothermal growth of vertically aligned nanowires was integrated with MEMS surface micromachining technology to fabricate the membrane proof-mass structure and the piezoelectric sensor

structure. Zinc oxide nanowires were compressed or released by the top layer of membrane proof-mass in response to external vibration. A peak output power of 70 pW was observed across an optimal 7 MΩ load when the device was excited with a peak acceleration of 1.4 g at 40 Hz which is the structural resonant frequency of the helicopter. The corresponding output voltage between the top and the bottom electrodes was 21.4 mV.

Table of Contents

List of Illustrations

List of Tables

List of symbols

a	radius of a single nanowire (m)
A	magnitude of acceleration (m/s^2)
A_{ol}	overlapping or the effective area of the electrodes of a MEMS parallel plate capacitor (m^2)
A_{pm}	area of proof-mass (m^2)
a_x	acceleration in x direction (m/s^2)
a_z	acceleration in z direction (m/s^2)
b_e	electrical damping coefficient (Ns/m)
b_m	mechanical damping coefficient (Ns/m)
B_{m1}	slide film damping coefficient between the proof-mass and substrate (Ns/m)
B_{m2}	slide film damping coefficient between the overlap fingers (Ns/m)
B_{m3}	squeeze film damping coefficient between gap closing fingers (Ns/m)
c	elastic constant matrix (Pa)
C_1 , C_2	two variable capacitors changing in opposite direction (F)
C_{bias}	bias capacitor (F)
C_D	equivalent capacitor of the piezoelectric micro energy harvester (F)
C_{gc2}, C_{gc1}	in-plane gap closing capacitors (F)
C_{max}	the max capacitance of the variable capacitor (F)
C_{min}	the min capacitance of the variable capacitor (F)
C_{ol2}, C_{ol1}	in-plane overlap capacitors (F)
C_{para}	parasitic capacitor (F)
C_{store}	storage capacitor (F)
C_v	variable capacitor (F)
d	gap distance between the electrodes of a MEMS parallel plate capacitor (m)
D	electric displacement (C/m^2)
d_{3i}	piezoelectric strain constant (m/V)

d_{gc}	distance between two adjacent gap closing finger groups (m)
e	piezoelectric coefficient matrix (C/m^2)
E	electric filed coupled in the piezoelectric effect (V/m)
E_1	electric field between the side walls of the stationary and moving fingers (V/m)
E_2, E_3	fringing electric fields (V/m)
E_{c1}	energy in the first step of charge-constrained mechanism (J)
E_{c2}	energy in the second step of charge-constrained mechanism (J)
E_i	induced electric field in a conventional piezoelectric microgenerator (V/m)
emf	magnitude of the electromagnetic force (V)
E_{v1}	energy in the first step of voltage-constrained mechanism (J)
E_{v2}	energy in the second step of voltage-constrained mechanism (J)
f	resonant frequency (Hz)
F_1 , F_2	electrostatic force across two variable capacitors (N)
F_e	electrostatic force for an in-plane gap closing, in-plane overlap or out-of-plane gap closing converter (N)
f_y	lateral bending force on nanowire tip (N)
g	initial gap between fingers of an in-plane overlap or gap closing converter (m)
g_{3i}	piezoelectric constant (Vm/N)
g_{gc}	gap between the gap closing fingers (m)
g_{ol}	gap between overlap fingers (m)
h	overlap length of the fingers for an in-plane overlap or gap closing converter (m)
h_{gc}	overlap length of gap closing fingers (m)
H_{gc}	length of gap closing fingers (m)
h_{ol}	initial overlap of overlap fingers (m)
H_{ol}	length of overlap fingers (m)
I_{xx}	area moment of inertia (m^4)
k	spring constant of a spring in the generic vibration generator (N/m)

k_l	lateral spring constant (N/m)
k_v	vertical spring constant (N/m)
L	length of the plate of an out-of-plane gap closing converter (m)
l	length of a single nanowire (m)
L_i	distance between the electrodes for a conventional piezoelectric microgenerators (m)
L_{pm}	proof-mass length (m)
l_s	spring length (m)
m_{pm}	mass of proof-mass (kg)
N_g	number of gaps formed per side by fingers for an in-plane overlap or gap closing converter
N_{gc}	number of gap closing fingers on one side of the proof-mass
N_{ol}	number of overlap fingers on one side of the proof-mass
N_s	No. of springs in parallel
P_{RL}	power across the load (W)
Q	charges on the MEMS parallel plate capacitor (C)
q_1 , q_2	charges across two variable capacitors of micro electrostatic energy harvester (C)
R_1, R_2	load resistors (Ω)
R_A,C_A	input impedance of SR560 low noise amplifier (Ω)
R_L	load resistor (Ω)
R_{th}	Thevenin resistor (Ω)
S_{gc}, S_{ol}	scaling factors
t	thickness of the device for an in-plane overlap or gap closing converter (m)
t_{PI}	gap between proof-mass and substrate (m)
t_{pm}	proof-mass thickness (m)
u	viscosity of the medium (Pa s)
V	voltage across the MEMS parallel plate capacitor (V)
V_1 , V_2	voltages across two variable capacitors (V)

V_{3i}	electrical potential difference between the electrodes of a conventional piezoelectric microgenerators (V)
V_{bias}	bias voltage source (V)
V_{in}	original voltage source (V)
V_{max}	the max voltage cross the variable capacitor (V)
V_{RL}	voltage across the load (V)
V_{th}	Thevenin voltage (V)
W	width of the plate of an out-of-plane gap closing converter (m)
w_{ol}, w_{gc}	width of overlap or gap closing fingers (m)
W_{pm}	proof-mass width (m)
w_s	spring width (m)
x	displacement of the proof-mass in X direction (m)
$y(t)$	input vibration displacement for a generic vibration generator (m)
y	displacement of the proof-mass in Y direction (m)
Y	Young's modulus for the electroplated nickel layer (Pa)
z	displacement of the proof-mass in Z direction (m)
$z(t)$	the relative displacement of mass for a generic vibration generator (m)
Z_{CD}, Z_{CA}	impedances of capacitors C_D, C_A at 40 Hz (Ω)
z_v	gap distance of the two parallel plates for an out-of-plane gap closing converter (m)
ε	mechanical strain matrix
ε_0	permittivity of the vacuum (F/m)
ε_3	mechanical strain in axis 3 direction
ζ_e	electrical damping ratio
ζ_m	mechanical damping ratio
ζ_T	electrical damping ratio plus mechanical damping ratio
κ	dielectric constant matrix (F/m)
ρ	density of nickel layer (kg/m^3)

σ	mechanical stress matrix (Pa)
σ_3	mechanical stress in axis 3 direction (Pa)
φ	the electrical potential along the cross section surface of nanowire (V)
Φ_B	magnetic flux through the circuit (Wb)
ω	Input vibration frequency for a generic vibration generator (rad/s)
ω_n	resonant frequency of a generic vibration generator (rad/s)

Chapter 1

Introduction

1.1 Overview of Wireless Sensor Networks (WSNs) and Necessity of Energy Harvesting Technology

Wireless sensor networks (WSNs) have many wireless sensor nodes which can sense the physical signals and transmit the converted electrical signals to the outside. A typical wireless sensor node includes power generating, sensing, computing and communication subsystems. Generally speaking, the communication subsystem consumes ~ 60% of the total power. Sensing subsystem consumes 6-20% [1]. The rest is consumed by the computing subsystems. Table 1-1 lists the power specifications for several common sensors.

Table 1-1 Power specifications for several common sensors [1].

Sensor	**Voltage (V)**	**Current (mA)**	**Power (mW)**
Temperature	3.3	0.008	0.026
Light	3.3	0.03	0.099
Humidity	3.3	0.3	0.99
Vibration	3.3	0.6	1.98
Barometric pressure	5	7	35

Nowadays, batteries are still the dominant power sources for the wireless sensor nodes. Since batteries have a limited lifetime which requires periodic replacing or recharging, continuous operation of the sensing system is compromised. Table 1-2 lists the power density of several energy storage technologies over the lifetime [2]. Figure 1-1 depicts the improvement of several important computing technologies such as disk

capacity and battery energy density from 1990 to 2003 [3]. The power density of batteries needs to be improved to catch up the growth of other technologies.

Table 1-2 Power density for several energy storage technologies [2]

	Power density ($\mu W/cm^3$), 1 year life time	**Power density ($\mu W/cm^3$), 10 year life time**
Batteries (non-recharge, lithium)	90	7
Batteries (rechargeable, lithium)	15	0
Micro heat engine (hydrocarbon fuel)	320	32
Fuel cells (methanol)	220	22

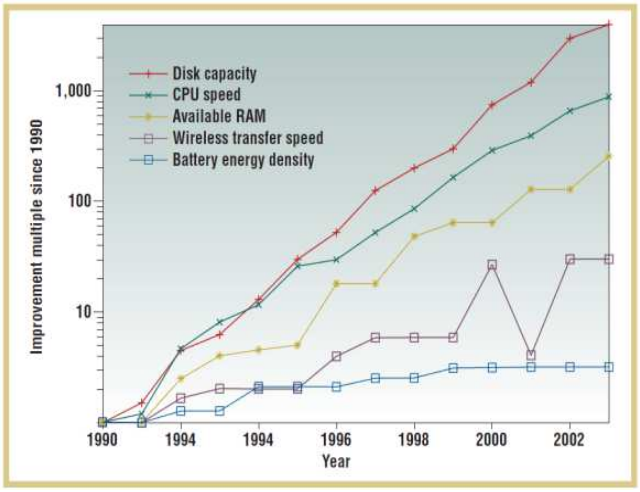

Figure 1-1 Improvements in the computing technologies from 1990-2003 [3] (Reprinted with permission. Copyright © 2005, IEEE)

To alleviate this issue, two approaches are explored: one is to develop a low power-consuming sensing system by improving the design and fabrication techniques; the other is the possibility of incorporating energy harvesters into the sensing system. The idea of energy harvesting is not new. Windmills, hydroelectric generators and solar

panels have been widely employed over the past decades. The real challenge is to integrate the harvesters into the modern electronic systems without failing to meet the power requirements.

1.2 Available Energy Sources for WSNs and Overview of Energy Harvesters

The ambient energy sources are mainly of four forms: radio frequency energy, light, thermal energy and mechanical vibrations. Much effort has been spent to convert these energies into electricity. For example, solar cell has been successfully used in outer space and daily lives by scavenging the sunlight based on the photovoltaic effect. The thermoelectric generators usually employ the structure of thermocouples and follow the principle of “Seebeck effect” [4]. The Seebeck coefficient of material denotes the efficiency of conversion of the electrical potential difference from a temperature difference. Table 1-3 lists several energy harvesting sources and their achievable power densities [1].

Table 1-3 Energy harvesting sources and their corresponding power densities [1]

Energy source	**Efficiency**	**Power density**	**Comments/challenges**
Radio frequency	50%	<1 μW/cm^2	The ambient radiation level is very low and has been spread out in a wide range.
Light	10~25%	100 mW/cm^2(outdoor), 100 μW/cm^2 (indoor)	Scaling down the size of the harvester is hard since power depends on the surface area of solar panels.
Thermal	0.1%, 3%	60 μW/cm^2 (human), 100 mW/cm^2 (industrial)	Efficiency is relatively low. High temperature difference is desired.
Vibration	25~50%	4 μW/cm^2 (human, Hz), 800 μW/cm^2 (machine, kHz)	Harvesters are compatible with the MEMS fabrication process.

Among all the above energy sources, the mechanical vibrations occur in numerous places such as common household goods, industrial plant equipment,

vibrating structures like buildings and bridges (Table 1-4) [5]. The widely available vibration sources make the vibration-to-electricity conversion a promising method.

Table 1-4 Acceleration magnitude and frequency of fundamental vibration modes for various sources [5]

Vibration source	Acceleration (m/s^2)	f_{peak} (Hz)
Car engine compartment	12	200
Base of 3-axis machine tool	10	70
Blender casing	6.4	121
Clothes dryer	3.5	121
Person nervously tapping his heel	3	1
Car instrument panel	3	13
Door frame just after door closes	3	125
Small microwave oven	2.5	121
HVAC vents in office building	0.2-1.5	60
Windows next to a busy road	0.7	100
CD on notebook computer	0.6	75
Second story floor of busy office	0.2	100

1.3 Mechanical Vibrational Energy Harvesters

1.3.1 General Theory of Vibration-to-Electricity Conversion Model

A simple linear model for the vibration-to-electricity conversion is presented in Figure 1-2 [5]. The inertial mass is mechanically attached to an inertial frame through the springs. The inertial frame accepts the outer vibrations *y(t)*. Hence, the suspended inertial mass has the relative displacement *z(t)*. This model is described by equation below according to the Newton's law [5]:

$$m_{pm}\ddot{z}(t) + (b_e + b_m)\dot{z}(t) + kz(t) = -m_{pm}\ddot{y}(t) \tag{1.1}$$

where, m_{pm} is the mass of the proof-mass, *z(t)* is the relative displacement of mass, b_e is the electrical damping coefficient, b_m is the mechanical damping coefficient, k is the

spring constant, *y(t)* is the input vibration displacement with typical frequency *ω* and magnitude.

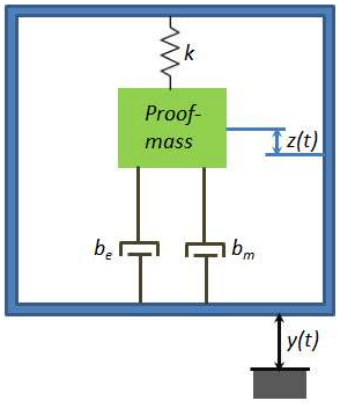

Figure 1-2 Schematic of the generic vibration generator [5]

Here, the electrical and mechanical damping force are simply assumed to be linearly proportional to the velocity *v*. The work done by the electrical damping contributes to the generated power and is given as [6]:

$$P = \int_0^v b_e v dv = \frac{1}{2} b_e v^2 = \frac{1}{2} b_e \dot{z}^2. \tag{1.2}$$

The magnitude of relative displacement can be solved by using the Laplace transformation of Eq. 1.1. The damping coefficients b_e and b_m are replaced by the damping ratios ζ_e and ζ_m : $b = 2m\zeta\omega_n$. k is replaced by the resonant frequency ω_n : $k = m\omega_n^2$. The magnitude of relative displacement is given by:

$$|Z| = \left| \frac{-\omega^2}{-\omega^2 + 2(\zeta_e + \zeta_m) j\omega\omega_n + \omega_n^2} \right| |Y|. \tag{1.3}$$

The magnitude of power is then derived as:

$$|P| = \frac{m\zeta_e \omega_n \omega^2 (\frac{\omega}{\omega_n})^4 Y^2}{(2\zeta_T \frac{\omega}{\omega_n})^2 + (1-(\frac{\omega}{\omega_n})^2)^2} \tag{1.4}$$

where, $\zeta_T = \zeta_e + \zeta_m$.

If the resonant frequency ω_n of this mass system matches the input vibration frequency ω, the maximum magnitude of power is achieved :

$$|P|_{\max} = \frac{m\zeta_e \omega^3 Y^2}{4\zeta_T{}^2}. \tag{1.5}$$

The magnitude of displacement *Y* can be expressed as: $Y = A / \omega^2$. (*A* is the magnitude of acceleration). Therefore, the magnitude of power can be expressed by the acceleration from the vibration sources. It is apparent that the power is proportional to the acceleration and mass.

$$|P|_{\max} = \frac{m\zeta_e A^2}{4\omega\zeta_T{}^2}. \tag{1.6}$$

The following conclusions can be drawn: The generator should be designed to resonate with the input vibration frequency. The power is optimized with lower ζ_m. The power is inversely proportional to the frequency with the defined acceleration, so the generator should be designed to resonate with the low frequency of the source spectrum. The power is proportional to the square of acceleration magnitude and mass of the proof mass.

Generally three types of generators utilize the vibrational energy. They are electromagnetic [7], piezoelectric and electrostatic [8] energy harvesters.

1.3.2 Electromagnetic Energy Harvester

The operation principle of the conventional electromagnetic energy convertor is based on Faraday's law. The induced electromotive force in any closed circuit equals to the rate of change of the magnetic flux. It can be quantitatively described as following:

$$emf = \left| \frac{d\varphi_B}{dt} \right| \tag{1.7}$$

where, *emf* is the magnitude of the electromotive force and Φ_B is the magnetic flux through the circuit. The conventional configuration of the converter consists of a moving rotor and an inductive coil shown in Figure 1-3 [9]. As the external vertical vibration is exerted, the magnet will oscillate in the *z* direction with respect to the coil and hence the change of the magnetic flux is induced in the coil. As a result, voltage is generated across the coil. The device described in [9] generates a voltage with the peak to peak value of 18 mV at the resonant frequency of 55 Hz with the acceleration of 14.9 m/s^2. The corresponding output power is 0.61 μW. One challenge with the small scale electromagnetic harvester is that magnet is hard to be realized using a micro fabrication process. Furthermore, the strong magnetic field may interfere with the operation of the other electronic components [10].

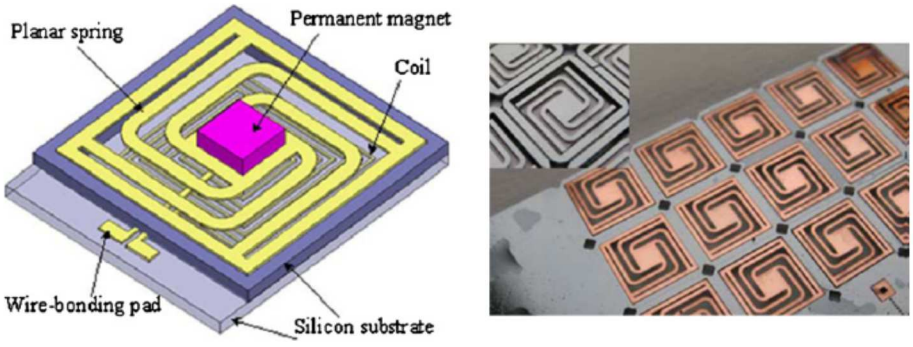

Figure 1-3 An electroelectromagnetic generator [9] (Reprinted with permission. Copyright © 2009, Springer-Verlag)

1.3.3 Electrostatic Energy Harvester

The electrostatic harvester is based on the movement of variable capacitors. An advantage of the electrostatic generator is that the device structures can be fabricated by MEMS process and thus easily integrated with other microelectronic components. An example of this type of generator is shown in Figure 1-4 [11]. The structure consists of a moving proof-mass with comb drive fingers as the movable electrode. The stationary fingers are anchored on the substrate as the fixed electrodes. Mechanical guidance is used to aid the motion of proof-mass. The maximum rms power is about 3.5 μW with the acceleration of 13g. There are two limitations for this kind of generator: an initial voltage source is needed to charge the capacitor, or electrets are desired which can permanently store charges in the ideal case [12, 13 ,14]. The other disadvantage is that pull in effect might occur if a high polarizing voltage is applied to the capacitor.

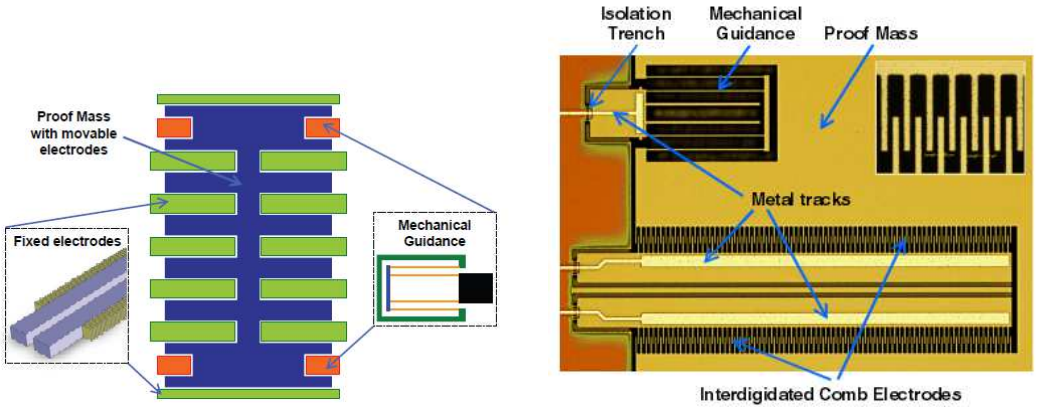

Figure 1-4 An electrostatic energy harvester [11] (Reproduced with permission.

1.3.4 Piezoelectric Energy Harvester

1.3.4.1 Piezoelectric Effect and Piezoelectric Materials

The word “piezoelectricity” comes from the Greek word “piezo” which means pressure. The piezoelectric effect was first discovered by the brothers Pierre and Jacques Curie in 1880. Piezoelectric effect is related to the interaction between the mechanical stress and electric dipole moments in the solid. It is a reversible process. When the material is deformed by the mechanical stress, the electric charges and fields are induced. On the other hand, when the electric field is applied to the piezoelectric material, the material will respond to it with mechanical deformation. Piezoelectric energy harvester utilizes the direct piezoelectric effect to convert the mechanical strain into electricity.

Three types of materials are commonly used for the piezoelectric energy harvesters: ceramics [15], polymers and nanostructures of some semiconductors. The first two types are normally used for the conventional piezoelectric microgenerators. The most common piezoelectric ceramic materials are lead zirconate titanate ($PbZr_xTi_{1-x}O_3$, PZT), barium titanate ($BaTiO_3$) and lead titanate ($PbTiO_3$, PCT). Most piezoelectric ceramics have the perovskite structure ABO_3. It is a simple cubic structure with a large cation-A on the corner, a smaller cation-B in the body center and oxygen-O in the centers of the faces [16]. PZT is widely utilized due to its excellent piezoelectricity. However, it cannot handle large strain since it is very brittle. Polymer polyvinylidene fluoride (PVDF) is a common piezoelectric polymer material. The piezoelectric effects of zinc oxide (ZnO) or gallium nitride (GaN) nanowires have been demonstrated in many piezoelectric nanogenerator designs [17, 18].

1.3.4.2 Conventional Piezoelectric Microgenerators

The most common design for the conventional piezoelectric microgenerator is the cantilever structure coated with piezoelectric ceramics [19]. There are usually two mechanisms: the d_{33} mode or the d_{31} mode [20]. d_{33} and d_{31} denote the piezoelectric strain coefficients. The schematic of these two modes are shown in Figure 1-5 [20]. In the d_{33} mode, the electric field direction is parallel to the mechanical stress/strain direction, while in the d_{31} mode, the electric field direction is perpendicular to the mechanical stress/strain direction. The mathematical expression can be modeled as [20]:

$$\varepsilon_3 = d_{3i} E_i \tag{1.8}$$

$$V_{3i} = \sigma_3 g_{3i} L_i \tag{1.9}$$

where, ε_3 is the mechanical strain, σ_3 is the mechanical stress (N/m^2). E_i is the electric field (V/m). d_{3i} (m/V) equals to the product of the piezoelectric constant g_{3i} (Vm/N) and dielectric constant of piezoelectric materials. V_{3i} (V) is the electrical potential difference between the electrodes. L_i (m) is the distance between the electrodes. The common design structures for these two modes are shown in Figure 1-6. In the d_{31} mode, PZT cantilever structure is realized by SOI wafer with Si as the proof-mass. Pt is used as the electrode. The average power is 0.32 μW. The corresponding power density is 416 μW/cm^3 [21]. In the d_{33} mode, cantilever structure is realized by the bulk micromachining process. SiO_2 and/or SiN_x works as the membrane layer, while ZrO_2 is used as the diffusion barrier layer. The Pt/Ti interdigitated electrode layer is on top of the PZT thin film layer. The proof-mass is made of SU-8 photoresist. This device generates 1 μW power across a 5.2 MΩ load resistor [20].

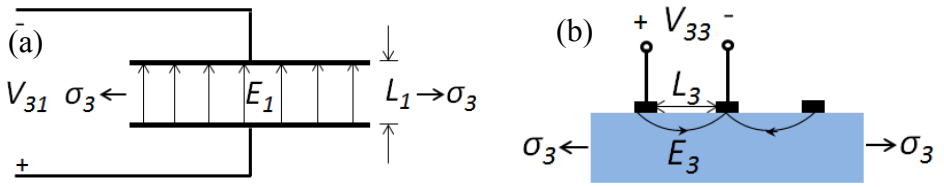

Figure 1-5 Schematics for (a) the d_{31} mode and (b) the d_{33} mode [20]

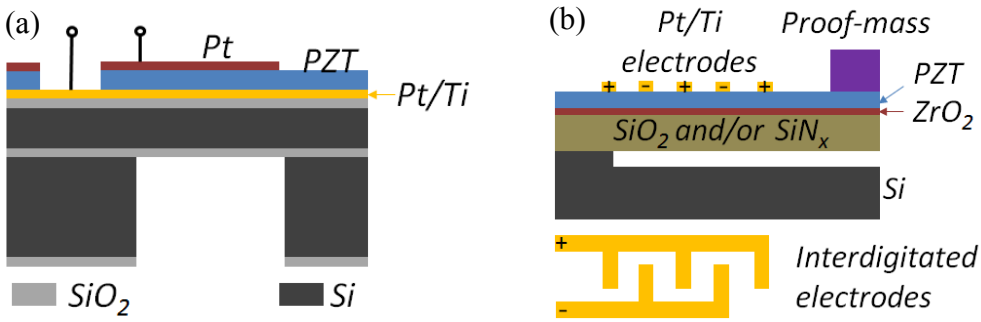

Figure 1-6 The design structures for (a) the d_{31} mode [21] (Reprinted with permission. Copyright © 2009 Elsevier B.V.) and (b) the d_{33} mode [20] (Reprinted with permission. Copyright © 2005 Elsevier B.V.)

The typical values of d_{33} and d_{31} for several piezoelectric materials are shown in Table 1-5 [22]. d_{33} is usually higher than d_{31}. Moreover, L_3 can also be larger than L_1 due to the interdigitated electrode design, while the L_1 is limited by the thickness of piezoelectric film. It concludes that the d_{33} mode is a better choice.

Table 1-5 Piezoelectric strain coefficient of several materials [22]

	d_{33}	d_{31}
PZT-5A	450 x 10^{-12}	180 x 10^{-12}
PZT-5H	380 x 10^{-12}	260 x 10^{-12}
PVDF	33 x 10^{-12}	23 x 10^{-12}

1.3.4.3 Piezoelectric Nanogenerators Utilizing Nanostructure of Materials

The piezoelectric nanogenerator utilizing nanostructure of ZnO has been first demonstrated by Z. L. Wang. Electric current is generated when the atomic force microscope (AFM) tip deflects a single nanowire. The complete structure of nanogenerator has been further achieved by either compressing/stretching or bending the nanowires. In Figure 1-7 (a), ZnO nanowires grow laterally on the flexible substrate. The nanowires have tensile strain when the substrate is bent, and therefore, the electrical potential is built at two ends of the nanowires. This device demonstrated an open circuit voltage of ~1.2 V and a short circuit current of ~ 26 nA [23]. Another structure was that the vertically standing nanowires were bent by a wafer coated with pyramid-shaped ZnO nanotips (Figure 1-7 (b)). The whole device was excited by an external ultrasonic wave. This device could be stacked together to form a four-layer structure which then generated power density of 0.11 μW/cm^2 at 62 mV [24].

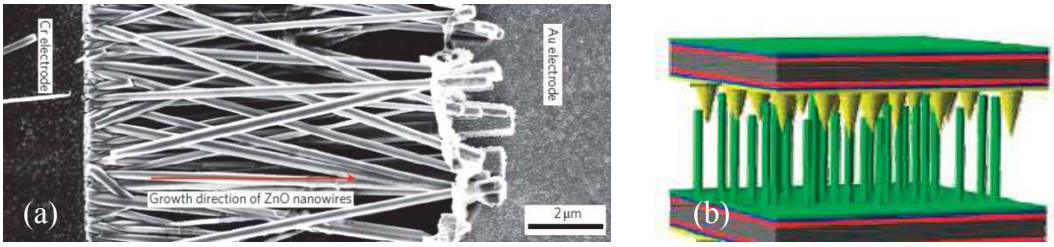

Figure 1-7 Piezoelectric nanogenerators. (a) Nanowires are stretched on a flexible substrate [23] (Reprinted with permission from Macmillan Publishers Ltd). (b) Nanowires are bent by the nanotips [24] (Reprinted with permission from ACS publications. Copyright © 2008 American Chemical Society).

1.3.4.4 Comparison of Conventional Microgenerators and Nanogenerators

Compared to the conventional piezoelectric material PZT, ZnO has a relatively lower piezoelectric coefficient. However, ZnO has some favorable properties. First, ZnO

nanowire can be deformed by a very large scale without cracking due to the high elasticity. This is superior compared to the brittle PZT. Second, from fabrication point of view, ZnO nanowires can grow in the chemical solution at low temperature, while fabrication of PZT usually needs a higher temperature process. Third, considering the application fields, ZnO can be used as biosensors due to its biocompatibility. ZnO is a green material, while PZT has heavy metal ions which are not environmental friendly.

1.4 Challenges and Opportunities for Energy Harvesters

For a wireless sensor node which is powered by an energy harvester, one key requirement is that the power generated from the harvesters must at least equal to the consumed power by the systems. Electrostatic energy harvesters always require an initial voltage to polarize the capacitors which is less attractive than the self-exciting piezoelectric energy harvesters. The power generated by the piezoelectric energy harvester still needs to be improved by either utilizing the advanced piezoelectric materials with better piezoelectricity or more superior design structures. In addition, the wireless sensors can be equipped with the advanced power management systems. The storage elements such as capacitors can store the generated energy from harvesters while sensors are in a sleep state. When sensors are in active state, the stored energy will be utilized for the proper operation of the sensors.

1.5 Summary

Wireless sensor nodes have been widely used in military, medical and civil fields to sense the physical signals and translate into the electrical signals. Batteries provide the power for the wireless sensor nodes in most cases. Wireless sensor nodes with the embedded energy harvesters are superior compared to the conventional battery-supported supported ones since the periodic replacement of batteries has been avoided. There are different kinds of waste energy from the environment such as thermal, light,

radio frequency or vibration. Based on the practical conditions and the availability of the energy sources, a specific energy harvester for that energy source can be utilized. The vibrations from the car engine, helicopter skin or bridge are all stable sources for the vibrational energy harvesters. Electromagnetic, electrostatic or piezoelectric are the three principles for the vibration energy harvesters. The usage of electromagnetic energy harvester is limited since the magnet may interfere with the other electronic components of wireless sensor nodes. Electrostatic energy harvester is favorable due to the compatibility with the traditional MEMS fabrication process, whereas the initial charging to the system is required. Piezoelectric energy harvester is self-powered due to the direct piezoelectric effect of materials. Piezoelectric nanogenerators utilizing the piezoelectricity of nanostructures such as ZnO nanowires have several attractive properties compared to the conventional piezoelectric micro energy harvesters.

Chapter 2

Hybrid Electrostatic Energy Harvester Incorporating In-Plane Overlap and In-Plane Gap Closing Mechanisms

2.1 Overview of Conversion Mechanisms and Topologies for Electrostatic Energy Harvester

2.1.1 Conversion Mechanisms

In an electrostatic energy harvester, MEMS capacitor is the device which converts the vibrational to electrical energy. The input vibrational energy is converted to electrical energy stored in the capacitor and then transported to the load via the external circuitry. This process, in which either the charge or voltage remains constant, is called a charge constrained or voltage constrained conversion cycle. It is well known that for a MEMS parallel plate capacitor, the capacitance *C* and charge *Q* can be given by the below equations:

$$C = \frac{\varepsilon_0 A_{ol}}{d} \tag{2.1}$$

$$Q = CV \tag{2.2}$$

where, ε_0 is the permittivity of the vacuum, A_{ol} is the overlapping or the effective area of the electrodes, *d* is the gap distance between the electrodes and *V* is the voltage across the capacitor.

2.1.1.1 Charge Constrained Conversion Cycle

The charges on the variable capacitor are held constant for the charge constrained conversion cycle. The vibration induces a change in the overlap area or gap distance which results in the capacitance change. Subsequently, the newly gained voltage is applied to a storage capacitor that stores the generated energy. The circuit diagram is shown in Figure 2-1 [5].

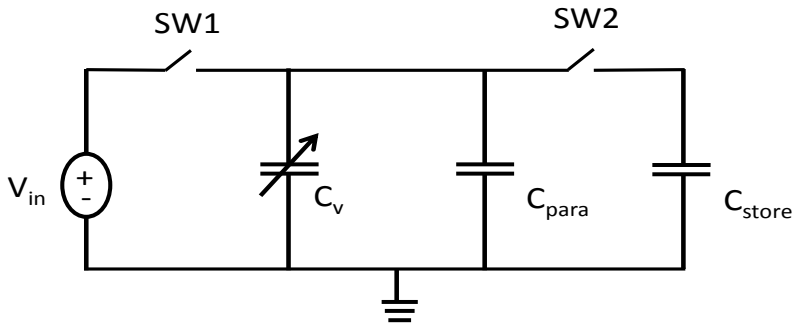

Figure 2-1 Circuit model for charge constrain conversion [5]

V_{in} is an original voltage source, C_v is the variable capacitor, C_{para} is the parasitic capacitance, C_{store} is the storage capacitor. *SW1* and *SW2* are switches that are employed to control the operation of the system. The system operates in three steps. The first step is called pre-charge of the variable capacitor: an external vibration causes C_v to reach its maximum value $C_{max,}$ then pre-charge happens once switch *SW1* closes and *SW2* opens. The charge and energy stored on the variable capacitor are given as:

$$Q = C_{\max} V_{in} \tag{2.3}$$

$$E_{c1} = \frac{1}{2} V_{in}{}^{2} C_{\max}. \tag{2.4}$$

During the second step, the energy harvesting occurs. The switch *SW1* is immediately opened, so the charges are constrained on the variable capacitor. At the same time, vibration takes place to make the variable capacitor change to the minimum value C_{min}. Therefore, voltage increases to the maximum value V_{max} and energy stored in the variable capacitor increases to E_{c2} which are given as below:

$$Q = C_{\min} V_{\max} \tag{2.5}$$

$$E_{c2} = \frac{1}{2} V_{\max}{}^{2} C_{\min}. \tag{2.6}$$

Energy transfer occurs in the third step. The switch *SW2* is closed and *SW1* remains open. Therefore, the charges stored in the variable capacitor will be shared with C_{store} and C_{par}. So the energy has now been successfully transferred to C_{store}.

It is apparent that the net energy harvested by the system from the vibration is just the energy difference between the first step and second step given as below: [5].

$$\begin{aligned} E_{harvested} &= E_{c2} - E_{c1} = \frac{1}{2} V_{\max}{}^2 C_{\min} - \frac{1}{2} V_{in}{}^2 C_{\max} \\ &= \frac{1}{2} V_{\max} \left(\frac{C_{\max} V_{in}}{C_{\min}} \right) C_{\min} - \frac{1}{2} V_{in} \left(\frac{C_{\min} V_{\max}}{C_{\max}} \right) C_{\max} \\ &= \frac{1}{2} V_{in} V_{\max} (C_{\max} - C_{\min}). \end{aligned} \tag{2.7}$$

2.1.1.2 Voltage Constrained Conversion Cycle

In a voltage constrained conversion cycle, the voltage on the variable capacitor is kept constant using a constant voltage source, while the charge on the capacitor varies based on the change of capacitance [25].

During the first step, the variable capacitor with the maximum capacitance of C_{max} is pre-charged by the voltage source V_{max}. Therefore the energy is given by:

$$E_{v1} = \frac{1}{2} V_{\max}^2 C_{\max}. \tag{2.8}$$

Next, a mechanical force causes the capacitance to decrease to C_{min} while voltage remains constant. At this step, energy is given by:

$$E_{v2} = \frac{1}{2} V_{\max}{}^2 C_{\min}. \tag{2.9}$$

The net harvested energy is given by:

$$E_{harvested} = E_{v2} - E_{v1} = \frac{1}{2} V_{\max}^2 (C_{\max} - C_{\min}). \tag{2.10}$$

These two possible energy conversion cycles can also be shown in the charge-voltage plane in Figure 2-2 [25].

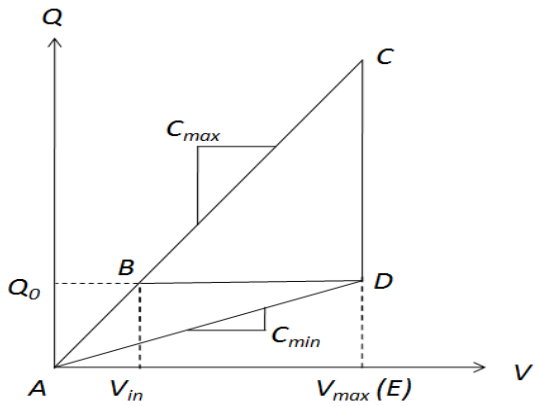

Figure 2-2 Two types of conversion cycle [25]

In the charge constrained case, the variable capacitor with the maximum capacitance is charged by the initial voltage V_{in}, which corresponds to the path segment A-B. During the segment B-D, the energy conversion occurs with the charge constrained. The voltage increases as the capacitance decreases until its minimum value. The net generated energy is the area enclosed by the path A-B-D-A, which is the area difference of triangular ADQ_0 and ABQ_0.

$$\begin{aligned} E_{harvested} &= A_{ADB} = A_{ADQ_0} - A_{ABQ_0} \\ &= \frac{Q_0 V_{\max}}{2} - \frac{Q_0 V_{in}}{2} = \frac{C_{\max} V_{in} V_{\max}}{2} - \frac{C_{\min} V_{\max} V_{in}}{2} \\ &= \frac{(C_{\max} - C_{\min}) V_{\max} V_{in}}{2} \end{aligned} \tag{2.11}$$

where, Q_0 is the constant charges on the variable capacitor.

For the voltage constrained case, the variable capacitor retains its maximum capacitance value C_{max} during segment A-C. The energy conversion occurs in the path C-D where the variable capacitor changes to its minimum capacitance value C_{min} with a

constant voltage. The total energy generated is the area enclosed by the path A-C-D-A, which is the area difference of triangular ACE and ADE.

$$E_{harvested} = A_{ACD} = A_{ACE} - A_{ADE} = \frac{1}{2} V_{\max}^2 (C_{\max} - C_{\min}). \quad (2.12)$$

It is clear that the energy available from the charge constrained case is less than that of the voltage constrained case. Both systems require the careful design of the power circuitry which controls the operation of components. Both conversion systems require an external voltage source to polarize the variable capacitor. One basic constraint for both cycles is the maximum allowable voltage, which is limited by the breakdown voltage of the switches in the charge constrained cycle or the pull in voltage of the variable capacitor.

2.1.2 Topologies

The key factor of electrostatic energy conversion is the change in the variable capacitor induced by the external vibration source. There are three basic topologies for a MEMS capacitor: out-of-plane gap closing, in-plane gap closing and in-plane overlap.

2.1.2.1 Out-of-plane Gap Closing Converter

Figure 2-3 Out- of-plane gap closing converter [5]

The side view of an out-of-plane gap closing converter is shown in Figure 2-3. Two large parallel electrode plates are used to construct the variable capacitor. The upper plate is mechanically anchored to the substrate through the springs, therefore it is free to move. The black arrow marks its vibration direction. The variable capacitance of the device is simply shown below:

$$C_v = \frac{\varepsilon_0 WL}{z_v} \tag{2.13}$$

where, W denotes the width of the large plate, L denotes the length of the plate and z_v denotes the gap distance of the two parallel plates. If the charge constrained system is employed, the electrical damping force also called electrostatic force F_e can be expressed by the below equation:

$$F_e = \frac{d(Q^2 / 2C_v)}{dz_v} = \frac{Q^2}{2\varepsilon_0 WL} \tag{2.14}$$

where, Q denotes the charge on the variable capacitor.

In order to acquire a large capacitance change, the upper plate must move a significant amount, possibly coming too close to the substrate. The electrostatic pull-in would probably happen in this situation. The device might be damaged if permanent attachment to the substrate were to occur. The additional design of the mechanical stop would help to alleviate this issue.

2.1.2.2 In-plane Gap Closing Converter

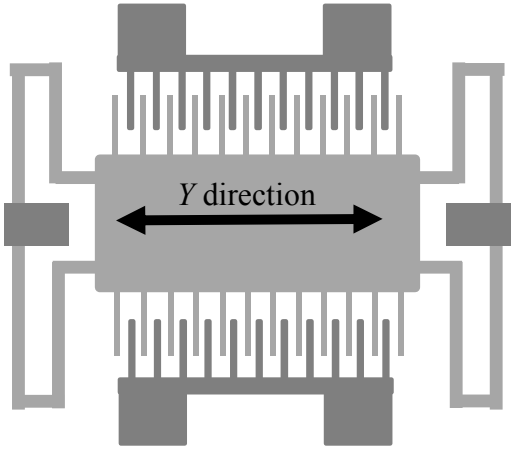

Figure 2-4 In-plane gap closing converter [5]

Figure 2-4 depicts the top view of an in-plane gap closing converter. Many comb drive fingers are connected in parallel to form the variable capacitor. The darkest portions represent the stationary fingers anchored on the substrate. The lighter grey portions denote the proof- mass and moving fingers anchored to the substrate through springs. The dark arrow shows the vibration direction. Thus the gap between the fingers is changing with vibration. Mechanical stops can be incorporated in the standard fabrication processes for protection. The variable capacitor's capacitance is given as:

$$C_v = N_g \varepsilon_0 th \left(\frac{2g}{g^2 - y^2} \right) \tag{2.15}$$

where, N_g is the number of gaps per side formed by fingers, h is the overlap length of the fingers, t is the thickness of the device, g is the initial gap between fingers and y is the displacement of the proof-mass in Y direction. The derived electrostatic force is given by [26]:

$$F_e(z) = \frac{Q^2 y}{2N_g g \varepsilon_0 th}. \tag{2.16}$$

The electrostatic force is proportional to the displacement of the proof-mass, and thus acts like a mechanical spring.

2.1.2.3 In-plane overlap converter

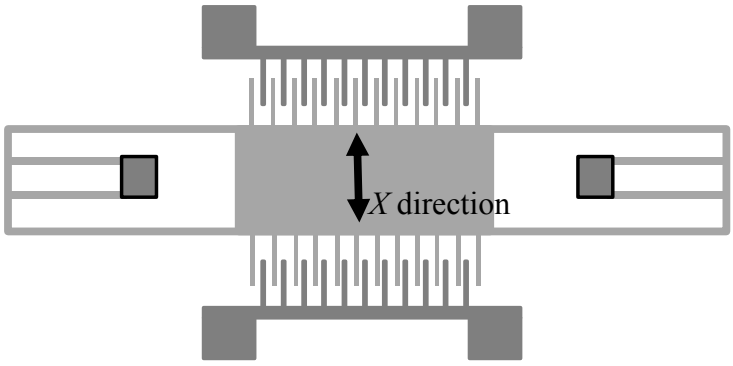

Figure 2-5 In-plane overlap converter [5]

For the in-plane overlap converter, a similar topology to the in-plane gap closing converter is used (Figure 2-5). The differences between them are the vibration direction and spring design. For the in the in-plane overlap converter, the overlap areas of the comb drive fingers change with vibration. The capacitance of variable capacitor is given as:

$$C_v = \frac{N_g \varepsilon_0 t(h+x)}{g} \tag{2.17}$$

where, x is the displacement of the proof-mass in X direction. The expression for the electrostatic force is given by [26]:

$$F_e = \frac{Q^2 g}{2N_g \varepsilon_0 t(h+x)^2}. \tag{2.18}$$

2.1.2.4 Comparison of three topologies

In summary, it is difficult to incorporate the mechanical stopper in the out-of-plane converter, while it is dangerous to device due to the possibility of electrostatic pull-in. For the other two converters, the implementation of a mechanical stopper would not be an issue from the fabrication point of view. The in-plane overlap converter requires a large displacement to gain the large capacitance change which might cause potential instability of the system. When it reaches to the maximum deflection, the system might have the out-of-plane displacement; whereas the gap closing converters require relatively smaller spring deflection which helps to improve the stability of the system [5].

2.2 Design and Simulation

2.2.1 Design Structure

The novelty of work presented here lies in the simultaneous use of in-plane overlap and in-plane gap closing capacitance variation modes with the vibration of the proof-mass. The device is built on a silicon substrate as shown in Figure 2-6 (a).

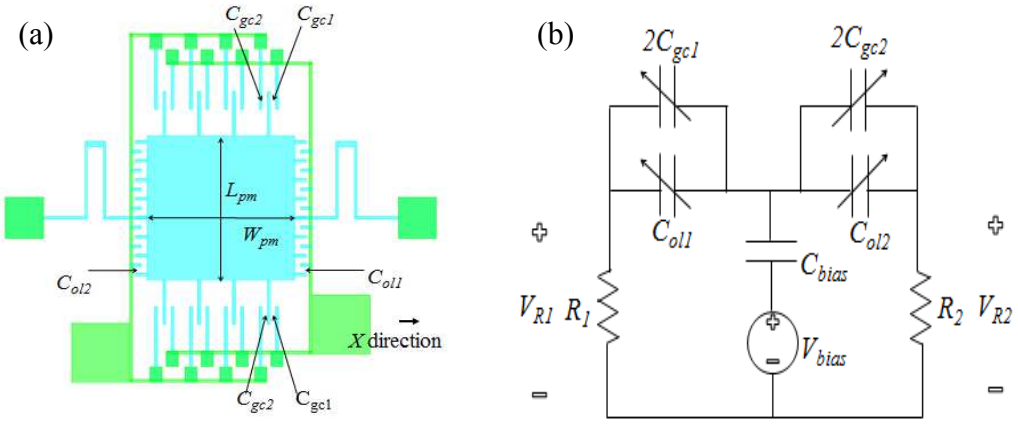

Figure 2-6 (a) Design schematic for the in-plane overlap and in-plane gap closing energy harvester. (b) Equivalent electrical circuit model.

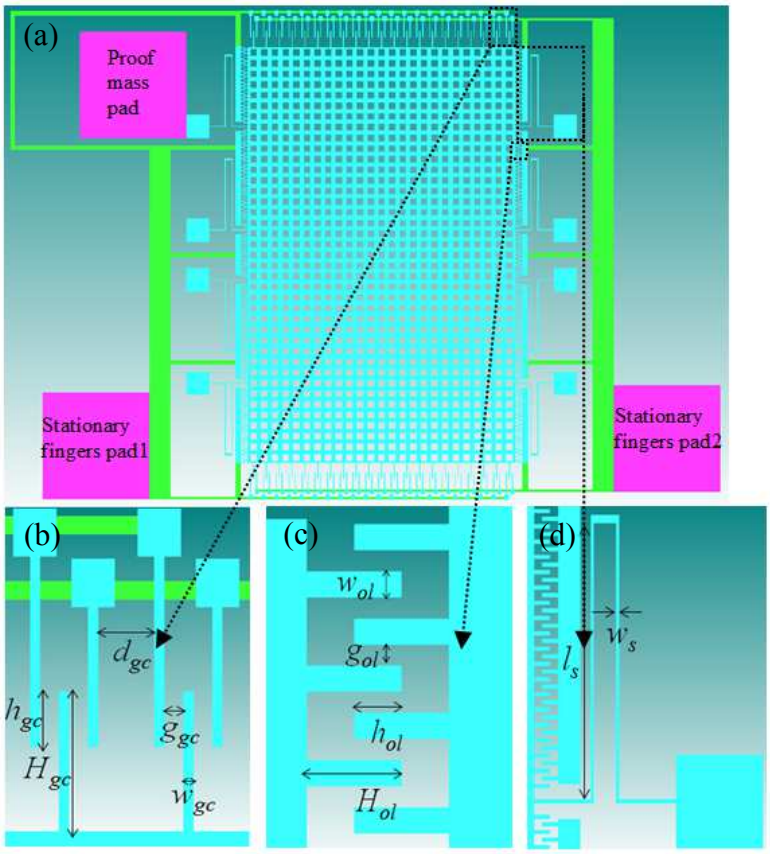

Figure 2-7 (a) Device structure. (b) Definition of parameters for overlap fingers, (c) gap closing fingers, and (d) springs.

Table 2-1 Design Parameters Summary

Parameter	Symbol	Design	Design consideration
Proof-mass length	L_{pm}		
Proof-mass width	W_{pm}		optimized
Proof-mass thickness	t_{pm}	7 μm	max set by UV-LIGA restrictions
Gap between proof-mass and substrate	t_{Pl}	2 μm	
Initial overlap of overlap fingers	h_{ol}		optimized
Length of overlap fingers	H_{ol}	$2\ h_{ol}$	
Gap between overlap fingers	g_{ol}	4 μm	UV-LIGA definition limit
Width of overlap or gap closing fingers	w_{ol}, w_{gc}	5 μm	UV-LIGA definition limit
Overlap length of gap closing fingers	h_{gc}	30 μm	
Length of gap closing fingers	H_{gc}	75 μm	
Gap between the gap closing fingers	g_{gc}	9 μm	
Distance between two adjacent gap closing finger groups	d_{gc}	27 μm	
Resonant frequency	f	0.80 or 1.50 kHz	vibrations on aircraft skin [27]
Number of springs in parallel for one device	N_s		
Length of spring	l_s	335 μm	
Width of spring	w_s	4 μm	

Electroplated nickel is chosen to be the material for the proof-mass and springs due to its resistance to corrosion as well as the relative ease of electroplating [28]. The proof-mass is suspended by serpentine springs from the substrate. Capacitive comb fingers construct either in-plane overlap capacitors C_{ol2} and C_{ol1} on two opposing sides of the proof-mass (left/right in Figure 2-6 (a)), or in-plane gap closing capacitors C_{gc2} and C_{gc1} on the other two opposite sides (top/bottom of Figure 2-6 (a)). An equivalent electrical circuit is used to analyze the harvested power (Figure 2-6 (b)). R_1, R_2 are 65 MΩ load resistors. A 50 V dc voltage source V_{bias} is employed to charge the 1 μF bias

capacitor C_{bias} to provide the initial charge for the system and to emulate an electret. Two variable capacitors C_1 ($C_1 = C_{ol1} + 2C_{gc1}$) and C_2 ($C_2 = C_{ol2} + 2C_{gc2}$) are formed between the proof-mass pad and the stationary finger pad1 or between the proof-mass pad and the stationary finger pad2 (Figure 2-7). They vary in opposite directions when the proof-mass oscillates from side to side. Charges stored in these variable capacitors flow through R_1 and R_2, and therefore ac currents with a 180° phase difference are generated. Structural parameters of the device shown in Figure 2-7 are listed in Table 2-1.

2.2.2 Power Simulation and Optimization

Based on the above definition for design parameters, variable capacitor C_1 can be written in terms of the displacement x in X direction:

$$C_1(x) = C_{ol1} + 2C_{gc1} = \frac{2N_{ol}\varepsilon_0 t_{pm}(h_{ol} - x)}{g_{ol}} + \frac{2N_{gc}\varepsilon_0 t_{pm} h_{gc}}{g_{gc} + x} \tag{2.19}$$

where N_{ol} is the number of overlap fingers on one side of the proof-mass, N_{gc} is the number of gap closing fingers on one side of the proof-mass. Voltage across capacitors V_1 can be expressed as [29] :

$$V_1 = \frac{q_1}{C_1(x)} = \frac{q_1}{\frac{2N_{ol}\varepsilon_0 t_{pm}(h_{ol} - x)}{g_{ol}} + \frac{2N_{gc}\varepsilon_0 t_{pm} h_{gc}}{g_{gc} + x}} \tag{2.20}$$

where q_1 is the charge stored in C_1. Electrostatic force F_1 existing in C_1 is given by:

$$F_1 = \frac{d(q_1 V_1 / 2)}{dx} = -\frac{{q_1}^2}{2} \frac{-\frac{2N_{ol}\varepsilon_0 t_{pm} h_{ol}}{g_{ol}} - \frac{2N_{gc}\varepsilon_0 t_{pm} h_{gc}}{(g_{gc} + x)^2}}{(\frac{2N_{ol}\varepsilon_0 t_{pm}(h_{ol} - x)}{g_{ol}} + \frac{2N_{gc}\varepsilon_0 t_{pm} h_{gc}}{g_{gc} + x})^2} \tag{2.21}$$

Similar equations for C_2, V_2 and F_2 can be derived by replacing x with $-x$ in Eqs. (2.19) - (2.21). Based on Kirchhoff's voltage law and Newton's second law, the characterization circuit is modeled as [30]:

$$\begin{cases} R_1 \dfrac{dq_1}{dt} = -V_1(q_{1,}x) - \dfrac{q_1 + q_2}{C_{bias}} + V_{bias} \\ R_2 \dfrac{dq_2}{dt} = -V_2(q_{2,}x) - \dfrac{q_1 + q_2}{C_{bias}} + V_{bias} \\ m_{pm} \dfrac{d^2x}{dt^2} = F_2(q_{2,}x) - F_1(q_{1,}x) - k_l x - (B_{m1} + B_{m2} + B_{m3}) \dfrac{dx}{dt} - m_{pm} a_x \end{cases} \tag{2.22}$$

where, m_{pm} is the mass of proof-mass, a_x is the external acceleration in x direction and k_l is the lateral spring constant of the device.

Mechanical damping due to internal friction is responsible for the energy loss in the system. Mechanical damping force is modeled to be proportional to the velocity of proof-mass. B_{m1} defined as the slide film damping coefficient between the proof-mass and the substrate is given by [2] :

$$B_{m1} = \frac{uA_{pm}}{t_{PI}} = \frac{um_{pm}}{\rho t_{pm} t_{PI}} \tag{2.23}$$

where, A_{pm} is area of proof-mass, u is the viscosity of the medium and ρ is the density of nickel layer. Similarly, B_{m2} is the slide film damping coefficient between the overlap fingers [2]:

$$B_{m2} = \frac{4uN_{ol} t_{pm} h_{ol}}{g_{ol}}. \tag{2.24}$$

B_{m3} defined as squeeze film damping coefficient between gap closing fingers is given [2]:

$$B_{m3} = \frac{32uN_{gc} {t_{pm}}^3 h_{gc}}{(g_{gc} - x)^3}. \tag{2.25}$$

Among the above three damping coefficients, slide film damping between the proof-mass and the substrate is the dominant one due to the large area of the proof-mass. In order to minimize mechanical damping induced energy loss, according to previous analysis, a larger gap between the proof-mass and the substrate or a thicker proof-mass is desired.

The latter will increase the inherent stress of the proof-mass. Both will complicate the fabrication of the device.

Under the external acceleration of 1gsin(2πft), the expected power was optimized with respect to W_{pm} and h_{ol}. The resonant frequencies are chosen as 1.50 or 0.800 kHz based on the aircraft fuselage and wing vibrational modes [27]. Solving Eq. (2.22) for $q_1(t)$ and $q_2(t)$, the harvested power from load resistors can be written as:

$$P(W_{pm}, h_{ol}) = R_1(\frac{dq_1}{dt})^2 + R_2(\frac{dq_2}{dt})^2. \quad (2.26)$$

Finally, four types of designs are chosen (Figure 2-8). The naming of the devices is based on two design parameters: the resonant frequency and spring constant. The device named as F1500K10 has a resonant frequency of 1500 Hz and a spring constant of 10 N/m. “F” denotes the resonant frequency. “K” denotes the spring constant. There are other three devices: F1500K15, F800K15 and F800K20.

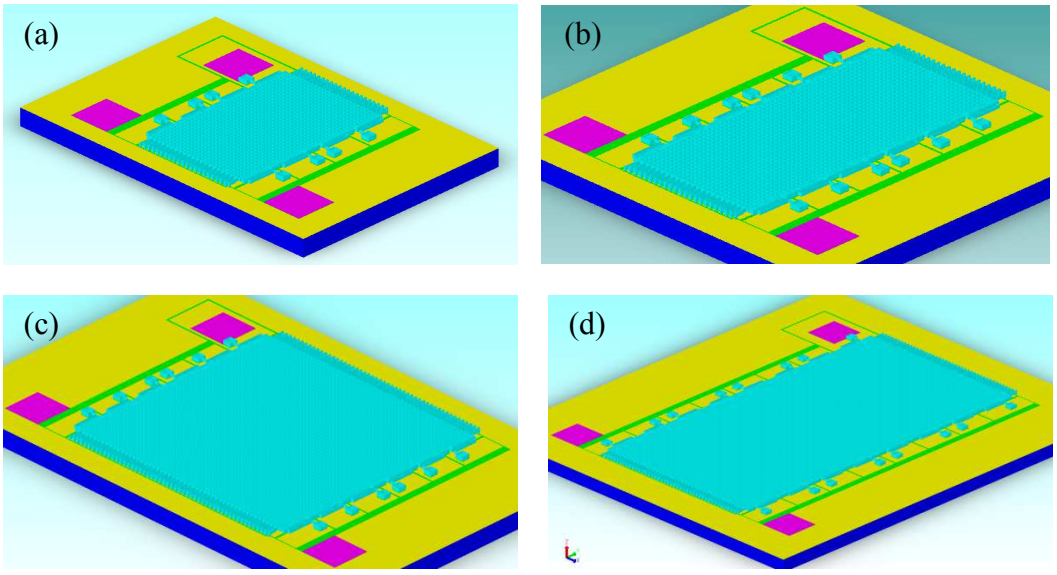

Figure 2-8 Solid models for device (a) F1500K10, (b) F1500K15, (c) F800K15, and (d) F800K20.

Table 2-2 Summary for power optimization results.

Device	Options	Resonant Frequency (Hz)	k_l (N/m)	L_{pm} (mm)	W_{pm} (mm)	h_{ol} (μm)	Power (nW)	Power Density (W/m^3)
F1500K10	Optimal	1500	10	1.95	1.26	10	6.24	534
F1500K15	Optimal	1500	15	2.93	1.31	11.2	11.7	650
	Final	1500	15	2.93	1.31	10	11.6	643
F800K15	Optimal	800	15	2.93	3.06	10.4	16.3	305
	Final	800	15	2.93	3.09	10	15.2	280
F800K20	Optimal	800	20	5	2.54	10	30.4	402
	Final	800	20	5	2.56	10	29.2	383

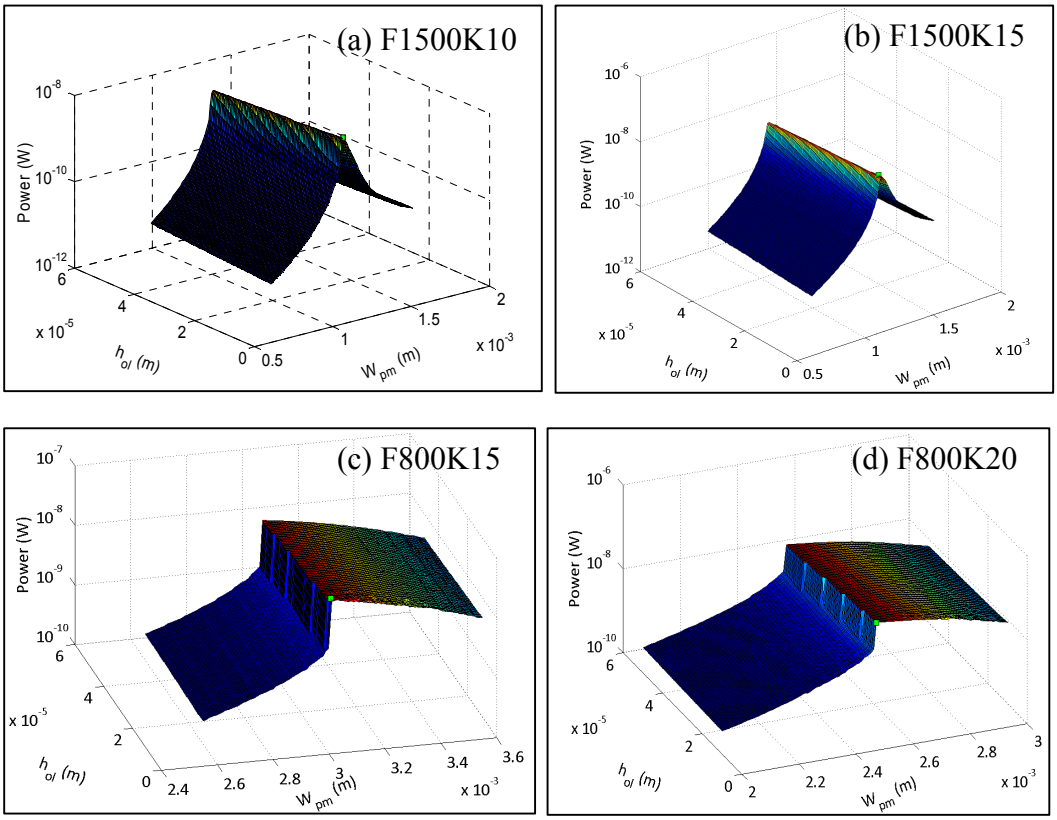

Figure 2-9 Power optimization contour for device (a) F1500K10, (b) F1500K15, (c) F800K15, and (d) F800K20.

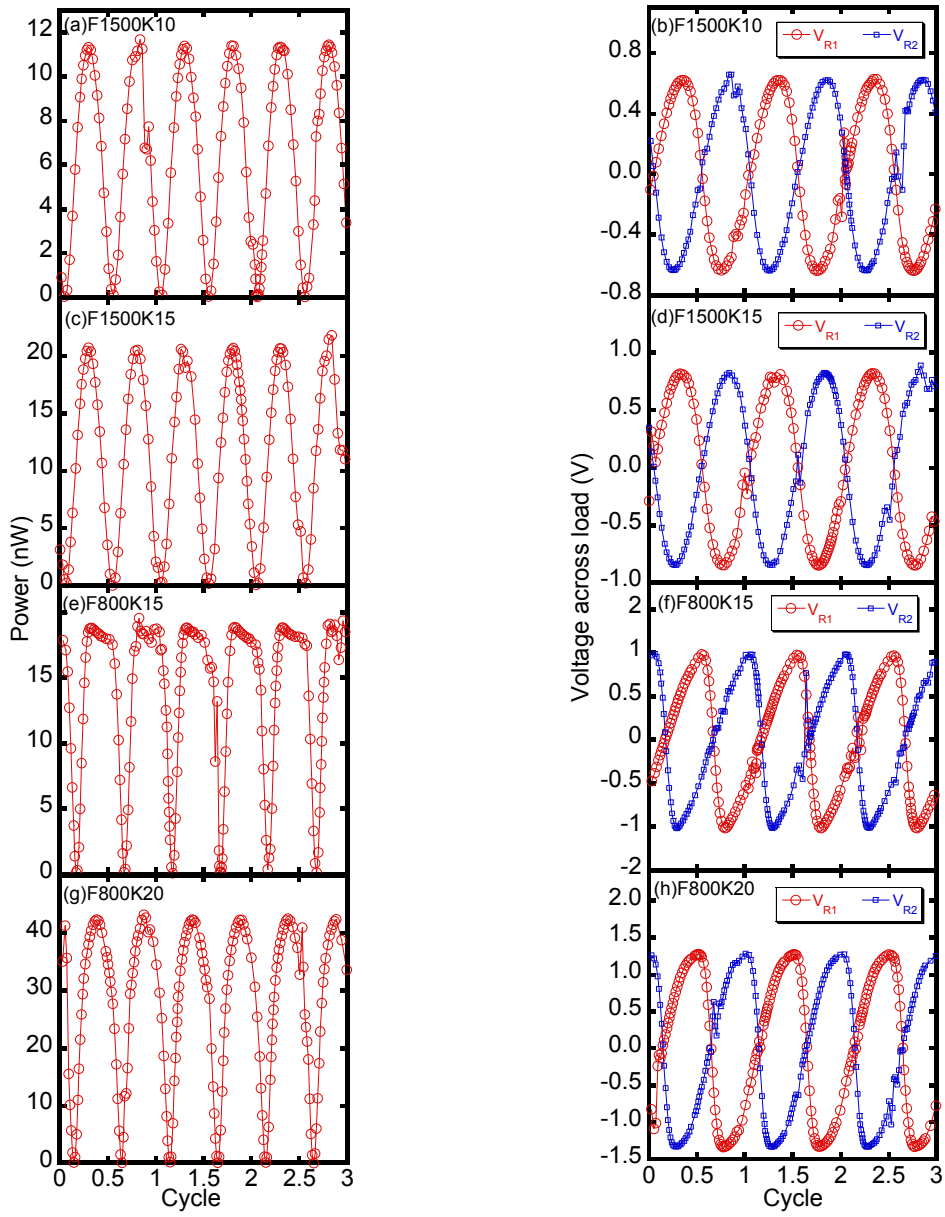

Figure 2-10 Transient plots of power across the loads with the final design parameters for device (a) F1500K10, (c) F1500K15, (e) F800K15, and (g) F800K20. Transient plots of voltage across the loads with the final design parameters for device (b) F1500K10, (d) F1500K15, (f) F800K15, and (h) F800K20.

Table 2-2 lists the optimal values for the initial overlap of overlap fingers h_{ol} and the width of proof-mass W_{pm}. Moreover, the corresponding power and power density have been presented. The final design parameters for W_{pm} and h_{ol} are carefully chosen based on the optimal values. Since power is a weak function of h_{ol}, the smaller h_{ol} is desired due to the fabrication considerations. W_{pm} is chosen carefully as well in order to avoid those values at which the power changes abruptly. Power contours with respect to h_{ol} and W_{pm} are shown in Figure 2-9. The transient performances of power and voltages across the loads with the final design parameters are shown in Figures 2-10.

In order to understand the effects of bias voltage and bias capacitor, power optimization simulation is performed for device F1500K10 with different voltage and capacitance values. The output power increases in an exponential manner with $V_{bias,}$ but does not change when C_{bias} changes (Figure 2-11). If load resistors are varied, the optimal W_{pm} or h_{ol} values obtained for the maximum power remain the same for all practical purposes, while the output power shows a modest increase (Table 2-3).

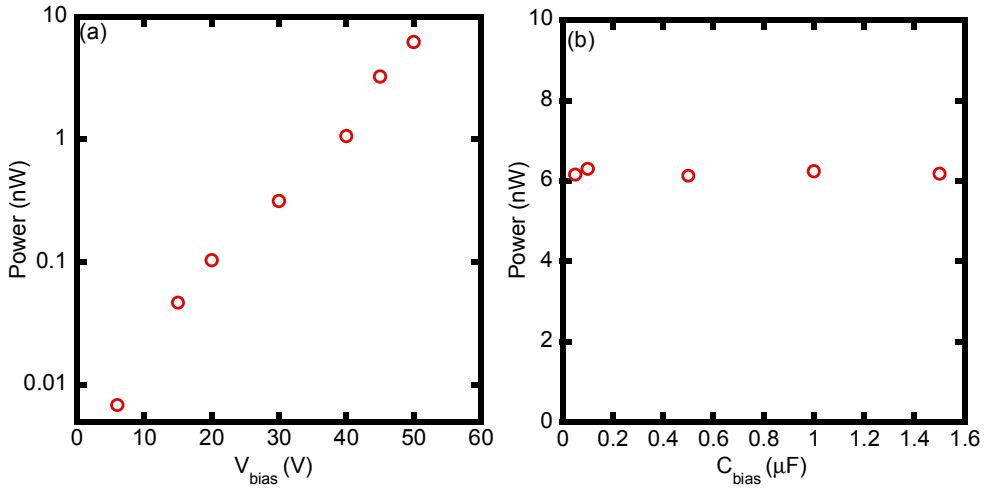

Figure 2-11 The output power with respect to (a) V_{bias} (C_{bias} = 1 μF), and (b) C_{bias} (V_{bias} = 50 V). R_1 = R_2 = 65 MΩ for both cases.

Table 2-3 Power optimization with respect to load resistors (V_{bias} = 50 V, C_{bias} = 1 μF)

R_1 , R_2 (MΩ)	W_{pm} (mm)	h_{ol} (μm)	Power (nW)	Power density (W/m^3)
5.00	1.25	11.20	3.96	340.54
12.00	1.26	10.00	3.98	340.35
20.00	1.24	11.20	5.35	463.18
27.00	1.24	10.80	5.51	477.53
35.00	1.25	10.00	5.14	442.93
42.00	1.25	10.40	5.79	498.92
50.00	1.25	10.00	6.43	554.34
57.00	1.25	11.20	6.41	551.00
65.00	1.26	10.00	6.24	534.00

In order to investigate the benefit of the hybrid structure, simulation is repeated with single vibrational mode designs for device F1500K10. For example, with only in-plane gap closing capacitors, the output power is 1.06 nW, while the output power is 0.217 nW if only in-plane overlap capacitors are considered. In fact, the hybrid structure results in more power than the sum of power from each mode.

2.2.3 FEM Analysis

2.2.3.1 Mechanical Simulation

CoventorWare is utilized to simulate the mechanical performance of the devices excited by a_z = 1g acceleration in the negative Z direction and a_x = 20g acceleration in the positive X direction. The proof-mass is anchored to the substrate by the springs. Therefore, the anchor surfaces of the springs are fixed mechanically as boundary conditions. The mechanical simulation results for each device are shown in Figures 2-12, 2-13. To save the simulation time, the proof-mass can be modeled as a solid plate without etch holes as long as the mass of proof-mass remains constant. Therefore, a smaller value of equivalent density of nickel is used to set up the simulation models. However, due to the small size of device F1500K10, the complete model with etch holes is utilized for simulation.

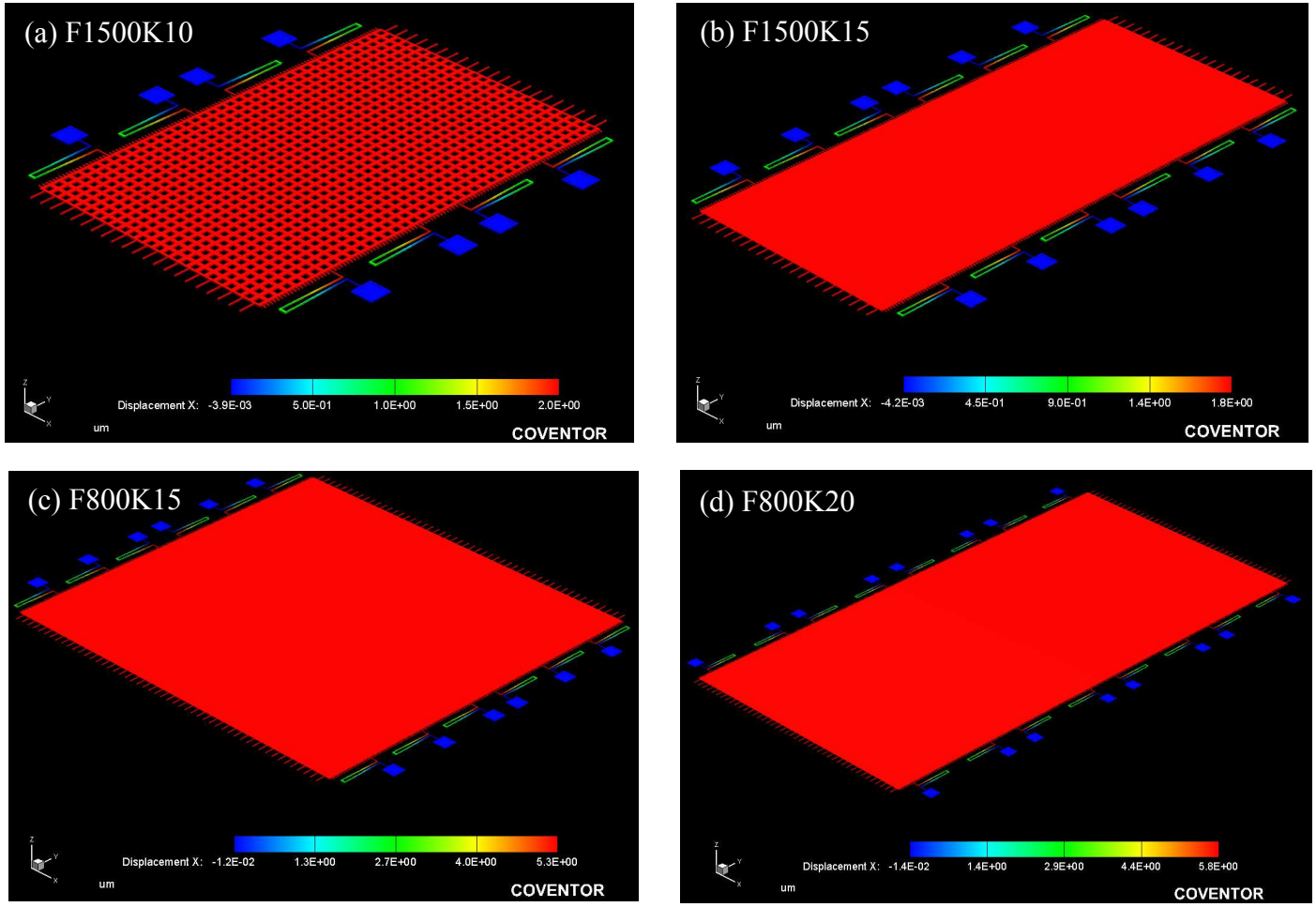

Figure 2-12 The displacement in *X* direction for (a) F1500K10, (b) F1500K15, (c) F800K15, and (d) F800K20. (a_z = -1g, a_x = 20g)

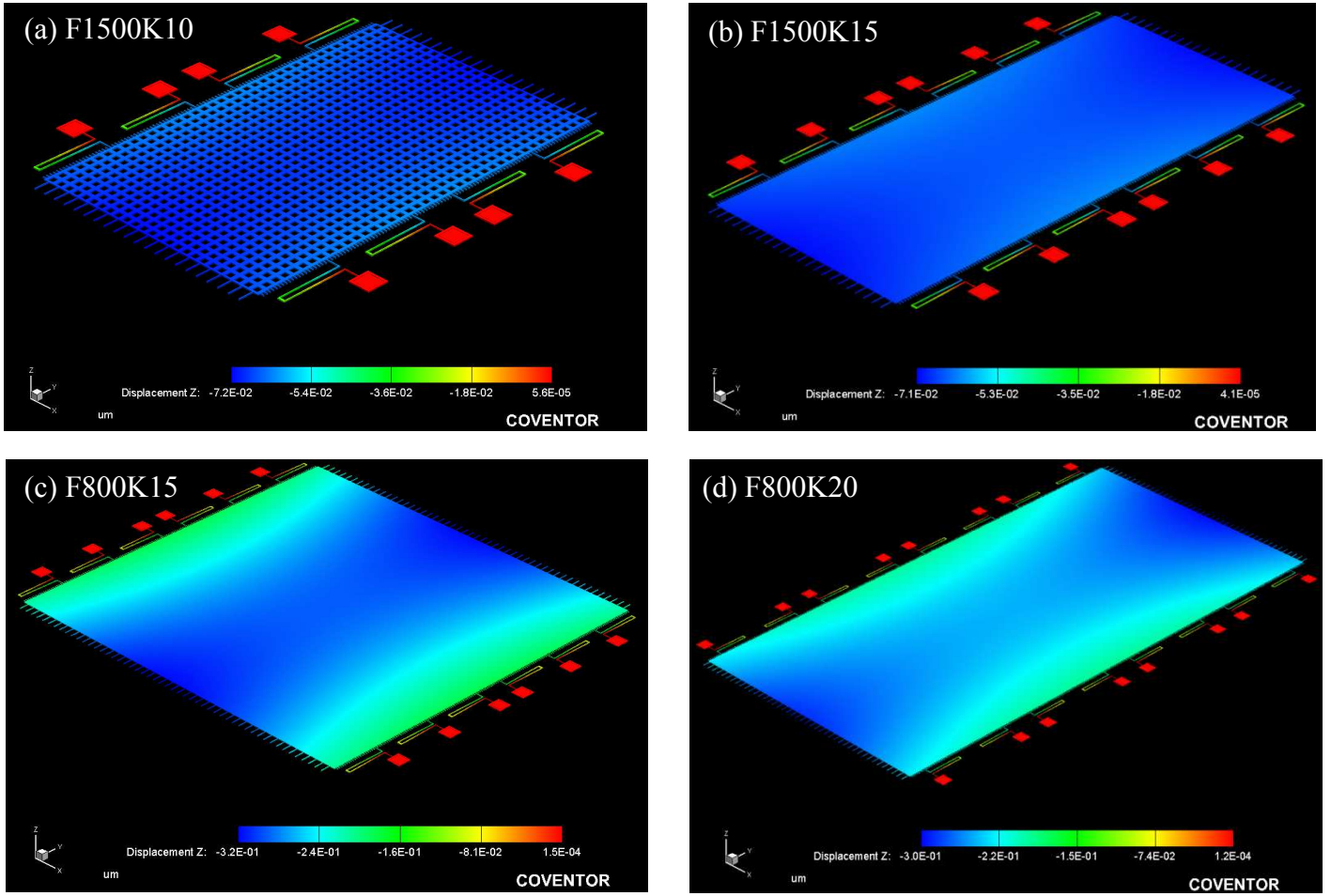

Figure 2-13 The displacement in *Z* direction for (a) F1500K10, (c) F1500K15, (e) F800K15, and (g) F800K20. (a_z = -1g, a_x = 20g)

Based on the proof-mass displacement *x* or *z*, the equivalent lateral and vertical spring constants k_l and k_v are given as:

$$k_l = \frac{m_{pm} a_x}{x} \tag{2.27}$$

$$k_v = \frac{m_{pm} a_z}{z}. \tag{2.28}$$

The theoretical calculations for the spring constants are given: [31, 32, 33, 34]:

$$k_l = N_s \frac{Y t_{pm} w_s^{\,3}}{2 l_s^{\,3}} \tag{2.29}$$

$$k_v = N_s \frac{Y w_s t_{pm}^{\,3}}{2 l_s^{\,3}} \tag{2.30}$$

where *Y* is the Young's modulus for the electroplated nickel layer (*Y* = 220 GPa) [35]. Spring length l_s and width w_s were carefully chosen to maximize the k_v/k_l ratio such that other modes of motions besides that in X direction are negligible.

Table 2-4 lists the values of k_l and k_v based on theoretical calculation as well as FEM simulation. The lateral spring constants agree with each other. From FEM simulation, displacement of the proof-mass in *z* direction is not uniform, while the maximum value is used in Eq. (2-28) to find out k_v. This explains that the values based on the FEM simulation are lower than that from the theoretical calculation.

Table 2-4 Calculation and simulation for spring constants

Device	N_s	m_{pm} (kg)	Calculation (N/m)		FEM simulation			
			k_l	k_v	*x* (μm)	*z* (μm)	k_l (N/m)	k_v (N/m)
F1500K10	8	1.04×10^{-7}	10.5	32.1	2.00	0.072	10.2	14.2
F1500K15	12	1.67×10^{-7}	15.7	48.2	1.80	0.071	18.2	23.1
F800K15	12	4.82×10^{-7}	15.7	48.2	5.30	0.32	17.8	14.8
F800K20	16	6.93×10^{-7}	21.0	64.2	5.80	0.30	23.4	22.6

2.3.3.2 Modal Harmonic Simulation

Modal harmonic simulation is done to find out the dominant vibration mode of the proof-mass. The same meshed solid model as in the previous mechanical simulation is employed for this analysis. The anchored surfaces of the springs are fixed as the surface boundary conditions. 1g acceleration is applied in the negative *Z* direction to emulate the gravity as the volume boundary condition. Additional harmonic acceleration between the frequencies of 600 Hz and 3000 Hz with 1g magnitude is applied to the movable proof-mass in the *X* direction.

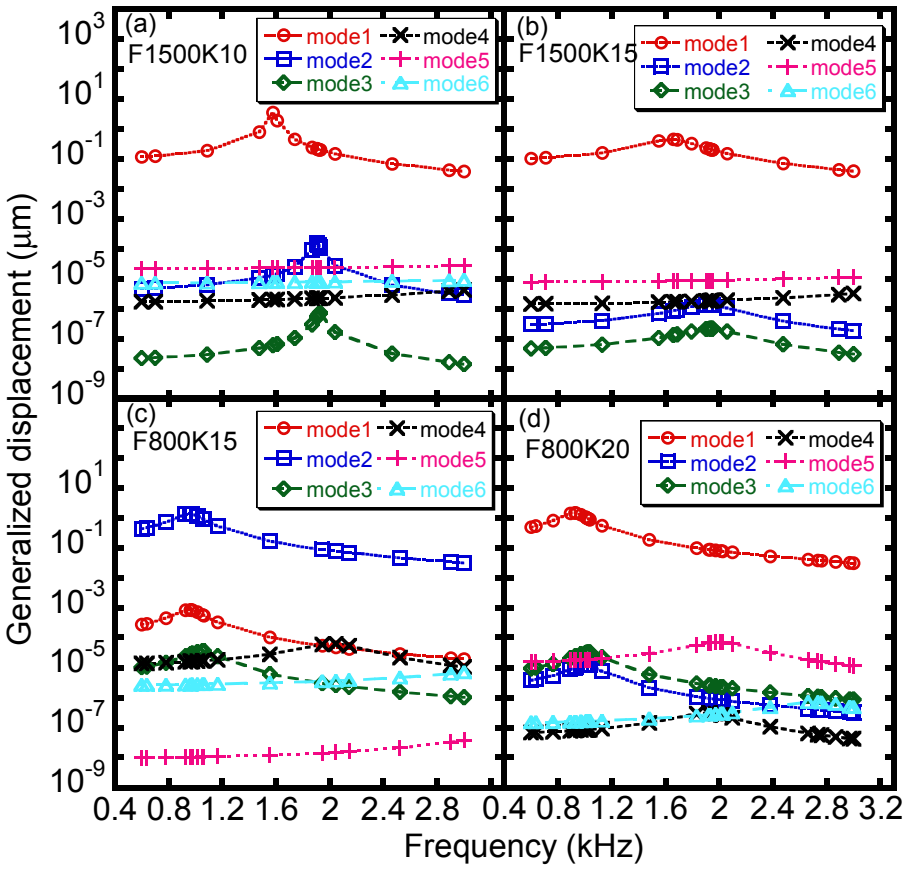

Figure 2-14 The generalized displacements of six modes for device (a) F1500K10, (b) F1500K15, (c) F800K15, and (d) F800K20.

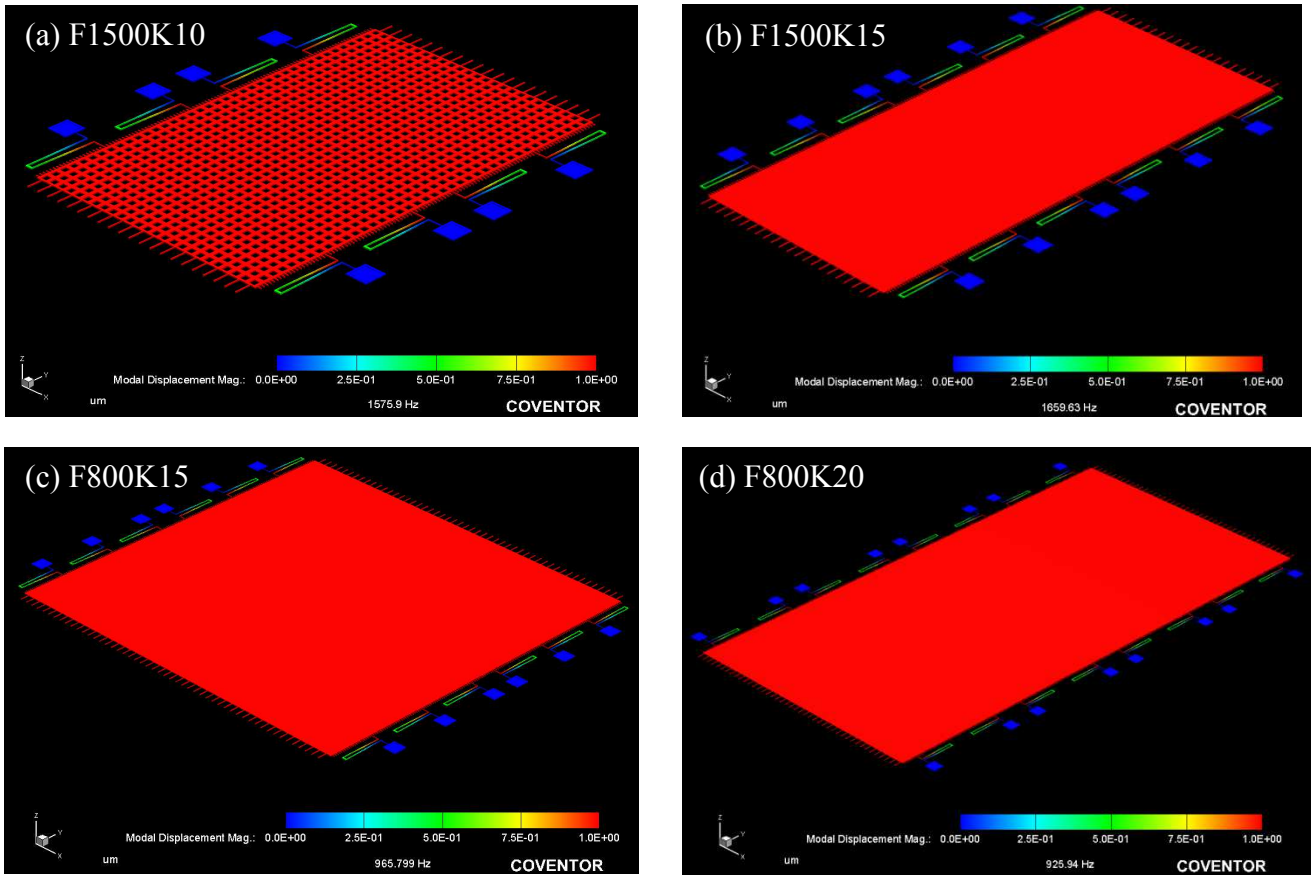

Figure 2-15 The vibrating modes with the highest generalized displacements for device (a) F1500K10 (mode1), (b) F1500k15 (mode1), (c) F800K15 (mode2), and (d) F800K20 (mode1).

The generalized displacements of six vibration modes are shown in the Figure 2-14 with respect to frequency for each device. Except for device F800K15 that has the highest generalized displacement for mode2, all other devices have the highest generalized displacement for mode1. The mode with the highest generalized displacement vibrates in the expected *X* direction (Figure 2-15). The simulated natural frequencies of these modes are close to the design values.

2.3.3.3 Capacitance Simulation

In order to reduce the computing time, half symmetry is utilized to simulate the capacitance between the proof-mass pad and the stationary finger pad1 or between the proof-mass pad and the stationary finger pad2. The stationary finger pad1 lies on the same side of the device as the proof-mass pad. The meshed model for device F800K20 is presented in Figure 2-16. The voltage of 6 V, 0 V, 0 V are applied to proof-mass pad, stationary finger pad1 and stationary finger pad2 respectively. The simulated capacitances are listed in the below Table 2-5. The theoretical values are fairly smaller than the simulated values due to the contribution of parasitic capacitance.

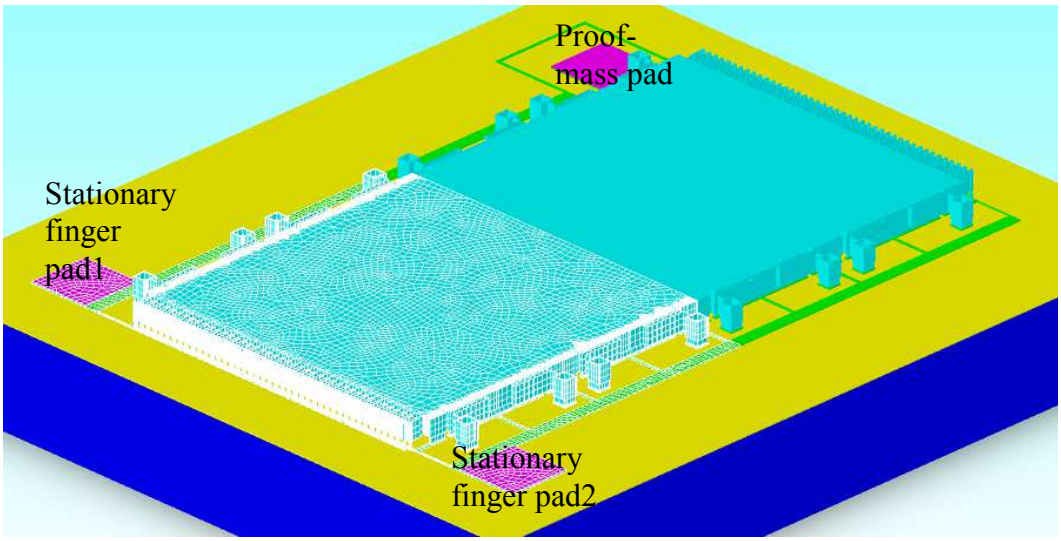

Figure 2-16 The meshed model of device F800K20 for capacitance analysis

Table 2-5 The simulated and calculated capacitance

Device	Capacitance between proof-mass pad and stationary finger pad1 (pF)	Capacitance between proof-mass pad and stationary finger pad2 (pF)	Capacitance of theoretical value (pF)
F1500K10	0.243	0.224	0.0843
F1500K15	0.331	0.311	0.0119
F800K15	0.381	0.411	0.0142
F800K20	0.540	0.526	0.207

2.3.3.4 Damping Simulation

DampingMM solver is used to simulate the damping coefficient.

In case of the slide film damping of the proof-mass with respect to the substrate, the quartered symmetry of a solid model without the stationary fingers is utilized for device F800K20 (Figure 2-17). The simulated damping coefficient value of 1.01 x 10^{-4} N/(m/s) is close to the calculated value of 1.03 x 10^{-4} N/(m/s) based on the previously discussed equation under the conditions of viscosity of air = 18.6 x 10^{-6} Pa·s; density of nickel = 8.91 x 10^{-15} kg/μm^3; mass of proof-mass = 6.85 x 10^{-7} kg.

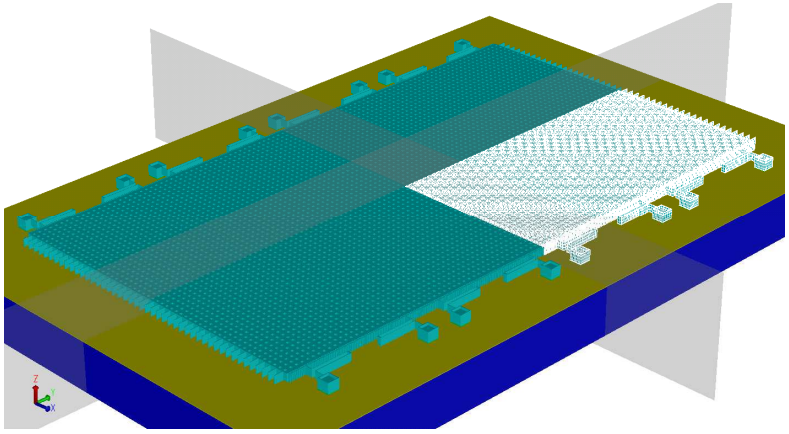

Figure 2-17 F800K20 meshed model for the proof-mass slide film damping simulation.

As for the slide film damping between the overlap fingers, it is proportional to the number of gaps between the fingers. To simplify the simulation, here only several comb drive fingers are built into the simulation model (Figure 2-18). The mesh type is Manhattan brick with the size of 1x1x1 μm in every direction. Similar to the slide film damping between the proof-mass and the substrate, the sidewalls are defined as the damping surfaces and the gap between overlap fingers is 4 μm. According to Table 2-6, the damping coefficient per gap remains the same for these two cases. So the total damping coefficient of the device is easily extrapolated by multiplying the number of gaps with unit damping coefficient (Table 2-7). According to Eq. (2.24), the overlap areas of the fingers should be used, while in simulation the area of sidewall defined as damping surface is twice the overlap area. Therefore, half of the simulated values are used to extrapolate the overall damping coefficient which agrees with the theoretical calculation.

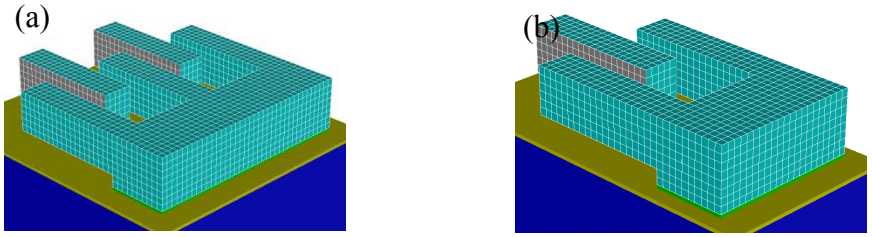

Figure 2-18 FEM Model of the overlap fingers for slide film damping simulation. (a) 4 gaps (b) 2 gaps.

Table 2-6 Simulation for slide film damping coefficient between the overlap fingers

Case	# of gap	Damping Coefficient (N/(m/s))	Damping coefficient/gap (N/(m/s))
2 movable figures, 3 stationary figures	4	1.302×10^{-9}	3.26×10^{-10}
1 movable figures, 2 stationary figures	2	0.651×10^{-9}	3.26×10^{-10}

Table 2-7 The extrapolated and MATLAB computed slide film damping coefficient between overlap fingers

Device	# of gaps	Damping coefficient/gap (N/(m/s))	Extrapolated Damping coefficient from CoventorWare (N/(m/s))	Theoretical value (N/m/s))
F1500K10	432	3.26×10^{-10}	1.41×10^{-7}	1.41×10^{-7}
F1500K15	648	3.26×10^{-10}	2.11×10^{-7}	2.11×10^{-7}
F800K15	648	3.26×10^{-10}	2.11×10^{-7}	2.11×10^{-7}
F800K20	1108	3.26×10^{-10}	3.61×10^{-7}	3.61×10^{-7}

In the case of squeeze film damping of the gap closing fingers, the same method has been employed. The damping coefficient can be extrapolated by multiplying the damping coefficient per gap with the number of gaps (Table 2-8). Among the six surfaces of one movable finger (Figure 2-19 (a)), the two sidewalls are defined as the damping surfaces. The surface connecting to the proof-mass is defined as a non-free surface. The other three surfaces are defined as free surfaces. The summary and comparison of the extrapolated and calculated values are listed in Table 2-9.

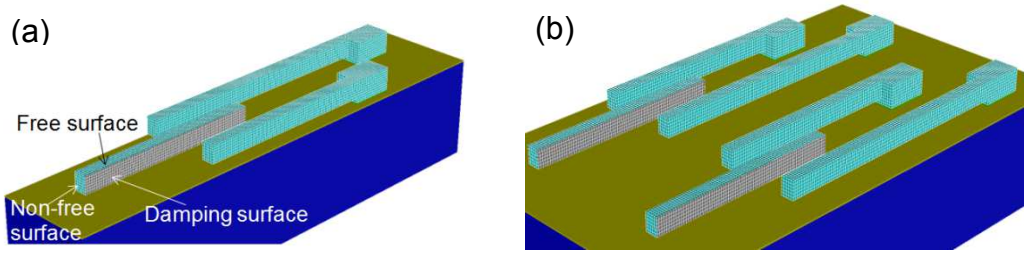

Figure 2-19 FEM model of gap closing fingers for squeeze film damping simulation. (a) 1 group. (b) 2 groups.

Table 2-8 Summary of squeeze film damping between the gap closing fingers

Case	Damping Coefficient (N/(m/s))	# of gap	Damping coefficient/gap (N/(m/s))
1 group figures	6.81×10^{-9}	2	3.41×10^{-9}
2 group figures	1.36×10^{-8}	4	3.41×10^{-9}

Table 2-9 The extrapolated and MATLAB computed squeeze film damping coefficients between gap closing fingers

Device	# of gaps	Damping coefficient/gap (N/(m/s))	Extrapolated Damping coefficient from CoventorWare (N/(m/s))	Theoretical value (N/m/s))
F1500K10	42	3.41×10^{-9}	1.43×10^{-7}	1.76×10^{-7}
F1500K15	44	3.41×10^{-9}	1.50×10^{-7}	1.85×10^{-7}
F800K15	102	3.41×10^{-9}	3.47×10^{-7}	4.24×10^{-7}
F800K20	86	3.41×10^{-9}	2.93×10^{-7}	3.61×10^{-7}

2.3 Fabrication

Based on the optimized device parameters and design, the energy harvester was fabricated using UV-LIGA. First, a 0.5 μm thick Si_3N_4 was deposited on a silicon wafer as an isolation layer. Aluminum interconnection lines and the pad layer were sputtered and subsequently patterned by a liftoff process (Figure 2-20 (a)). A photo-definable polyimide was chosen as the sacrificial layer, which was patterned by traditional lithography to create anchor openings for the suspended proof-mass (Figure 2-20 (b). A 0.1 nm gold layer was evaporated as a seed layer followed by a mold layer made of negative photoresist with a high aspect ratio. Nickel sulphamate solution was utilized to electroplate the proof-mass. In order to minimize the internal tensile stress, an organic stress reducer was added into the plating solution. Electroplating was processed at 45 ^{o}C

with a current density of 13 mA/cm^2 [35, 36]. An nickel layer of 8.8±1 μm thick was obtained at an approximate growth rate of 0.16 μm/min over 50 minutes of electroplating. The mold layer was removed in acetone. The evaporated gold layer was subsequently etched by argon-plasma anisotropic sputtering (Figure 2-20 (c)). As a final step, the sacrificial layer was ashed in an oxygen plasma to release the proof-mass. The fabricated device is shown in Figure 2-20 (d).

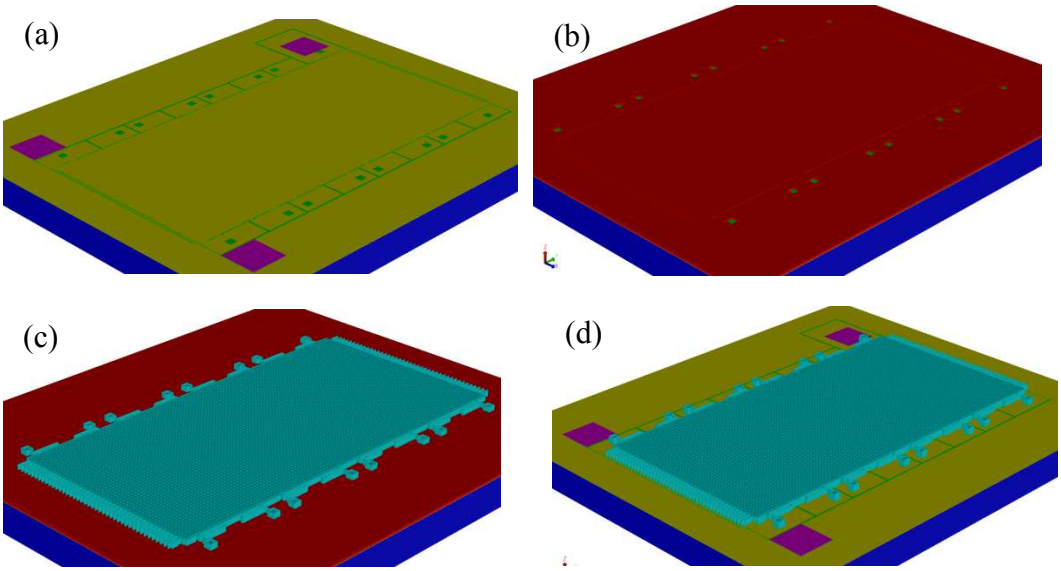

Figure 2-20 (a) Aluminum interconnection lines and pad layer. (b) Sacrificial layer. (c) Electroplated nickel layer. (d) The final released device.

SEM and microscope images of the fabricated devices are presented in Figure 2.21. The aluminum interconnection lines and pad layer are shown in Figure 2-21 (a). Sacrificial layer opening at the anchoring areas, mold pattern around the stationary finger area and electroplated nickel layer are depicted in Figures 2-21 (b)-(d), respectively. The final released device F1500K10 is shown in Figure 2-22 (a). Due to the stress in the electroplated nickel layer, the proof-mass bows up from the substrate (Figure 2-22 (b)). This issue is even worse for the larger size devices.

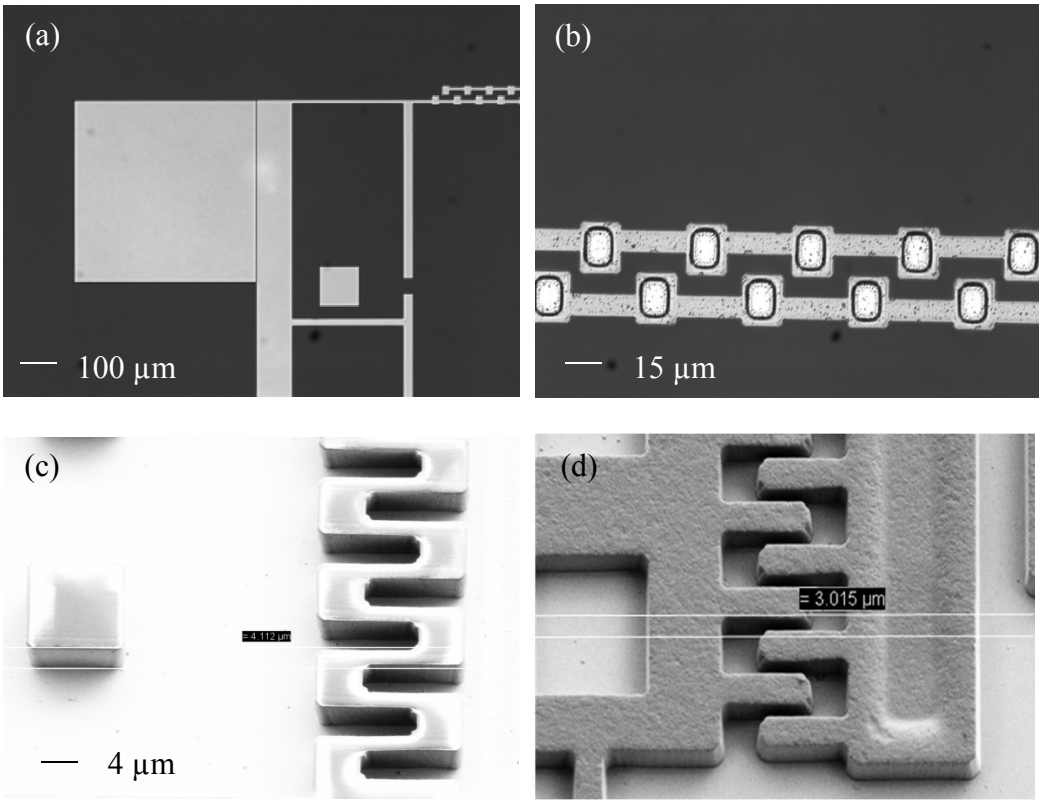

Figure 2-21 SEM and microscope images of fabricated devices. (a) Aluminum interconnection lines and pad layer. (b) Sacrificial layer opening at the anchoring areas (c) Mold pattern around the stationary finger area. (d) Electroplated nickel layer.

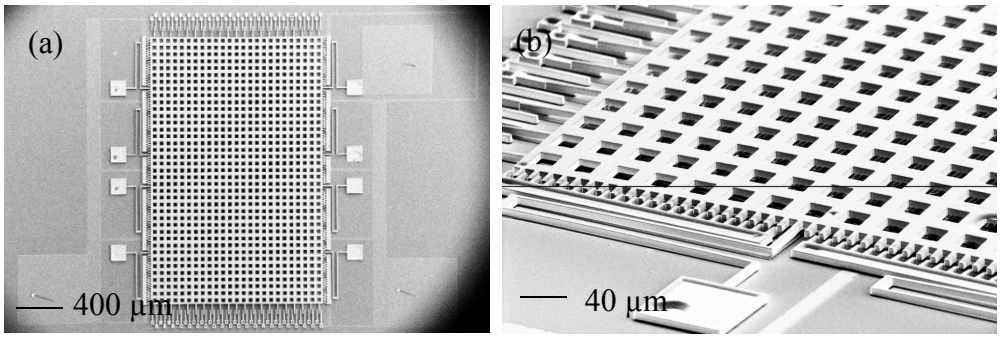

Figure 2-22 SEM images of fabricated devices. (a) The final released device F1500K10. (b) Proof-mass bowing up from the substrate.

2.4 Characterization

2.4.1 Characterization Setup

As discussed before, due to the fabrication issue with larger sized devices, only device F1500K10 was packaged and characterized. Three bond pads for the proof-mass, stationary finger pad1 and stationary finger pad2 were connected to a 28-pin dual in-line package (DIP) by ultrasonic gold wire bonding. The package was then mounted on an ED-10 shaker driven by a Crown DSi 1000 power amplifier and HP 3312A signal generator at varying frequencies and magnitude. A reference accelerometer with a sensitivity of 40 mV/g was also mounted on the shaker for calibration purpose. The characterization setup is shown in Figure 2-23 [31]. A 6 V dc bias voltage source was used to induce an initial charge on the 1 μF bias capacitor. AC output voltages across 5 MΩ of R_1 and R_2 each, were then measured by the oscilloscope. The load resistor values were chosen in the lower range of the simulation results shown in Table 2-3, to compensate for the increased capacitance due to parasitic effects in the measurement set-up, such that frequency band-width is not significantly reduced because of the increased RC time constant.

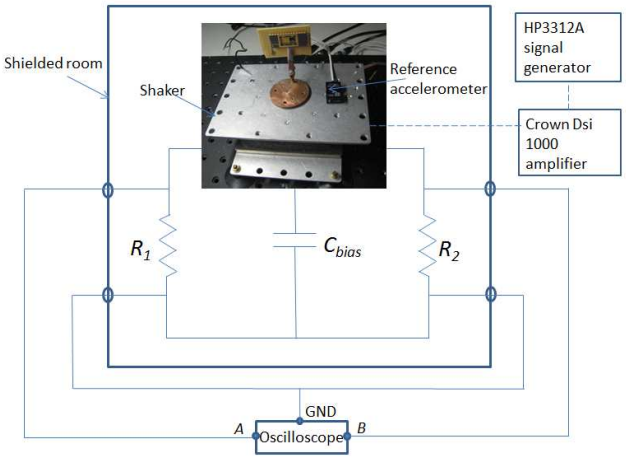

Figure 2-23 Characterization setup for the energy harvester [31].

2.4.2 Frequency Sweep

In order to find the resonant frequency of the device, the shaker was excited at different frequencies. Figure 2-24 shows the resonant frequency of the device is 1.90 kHz, which is higher than the expected value of 1.50 kHz. The resonant frequency *f* is related to lateral spring constant k_l and the proof-mass m_{pm} as following:

$$f = \sqrt{k_l / m_{pm}} / 2\pi = \sqrt{N_s \frac{Y t_{pm} w_s^{\,3}}{2 l_s^{\,3}} / (L_{pm} W_{pm} t_{pm} \rho)} / 2\pi = \sqrt{N_s \frac{Y w_s^{\,3}}{2 l_s^{\,3} L_{pm} W_{pm} \rho}} / 2\pi \quad (2.31)$$

Wider nickel springs resulted during fabrication due to the slight overdevelopment of the mold layer, thus yielding an actual resonant frequency higher than the expected value.

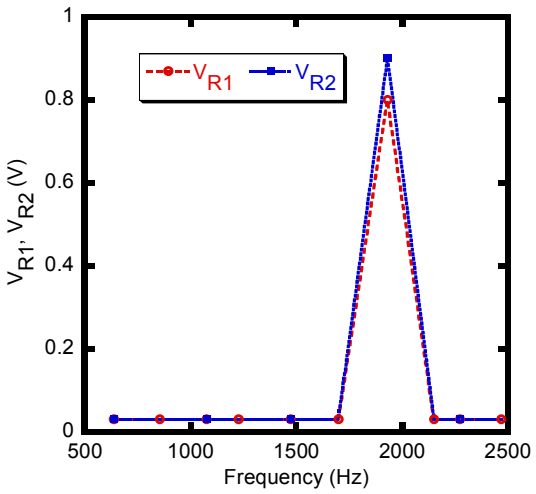

Figure 2-24 Frequency response of the device with a resonant frequency of 1.90 kHz.

2.4.3 Signal to Noise Ratio

Figure 2-25 (a) illustrates that the generated peak to peak ac voltage across R_1 and R_2 is 0.8 V and 0.9 V, respectively, when the device is mounted on the shaker at an excitation frequency of 1.90 kHz and an acceleration magnitude of 8g. To evaluate the noise pick-up, the measurement is repeated with the device mounted off the shaker with

the shaker still on. 8 mV peak to peak sinusoidal noise pick-up is detected (Figure 2-25 (b)). Thus, signal to noise ratio (SNR) is 100 or better.

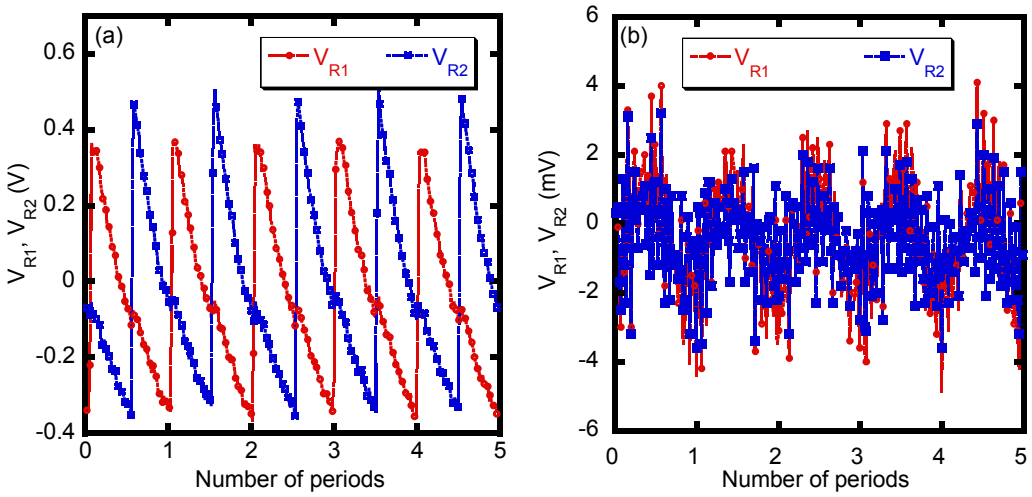

Figure 2-25 (a). Generated peak to peak ac voltage across R_1 and R_2 is about 0.8 V and 0.9 V respectively at an excitation frequency of 1.90 kHz and acceleration magnitude of 8g (at the moment the 6V DC bias voltage source is disconnected). (b) 8 mV peak-to-peak noise pick-up with the same conditions except that the device is mounted off the shaker.

2.4.4 Back Simulation Considering Fringe and Parasitic capacitances

Comb finger capacitors inherently exhibit fringing field capacitance because the electric field not only emanates between overlap areas but also other surfaces of the fingers. In Figure 2-26 (a), six of in-plane overlap capacitors with the proof-mass are modeled. In addition to the expected electric field E_1 between the side walls of the stationary and moving fingers, there are other fringing electric fields E_2, and E_3. E_2 exists between the end surface of the moving fingers and the stationary fingers. E_3 is between the top surfaces of the stationary and the moving fingers [37]. The fringing field

capacitors add to the harvesting of energy since the total change of capacitance increases. For instance, if the proof-mass moves away from the stationary fingers, ideal capacitance decreases. So does the fringing field capacitance. Likewise, fringing field and ideal capacitance increase when the proof-mass moves closer to the stationary fingers. Two scaling factors S_{gc}, S_{ol} are introduced for a more accurate capacitance calculation. Additionally, parasitic capacitance C_{para} exists between the aluminum lines on the substrate and the proof-mass. This, however, does not contribute to harvesting. Revised C_1 and C_2 are then expressed as:

$$C_1(x) = C_{ol1} + 2C_{gc1} = S_{ol}\frac{2N\varepsilon_0 b_1(h-x)}{\delta} + S_{gc1}\frac{2N_{gc}\varepsilon_0 b_1 h_{gc}}{g_{gc}+x} + Cpara1 \quad (2.32)$$

$$C_2(x) = C_{ol2} + 2C_{gc2} = S_{ol}\frac{2N\varepsilon_0 b_1(h-x)}{\delta} + S_{gc2}\frac{2N_{gc}\varepsilon_0 b_1 h_{gc}}{g_{gc}+x} + Cpara2. \quad (2.33)$$

Based on the section discussed before, V_1, V_2, F_1, and F_2 are recomputed.

Scaling factors are defined according to FEM simulations using CoventorWare®. The capacitance simulation is performed for one to six of in-plane overlap capacitors. S_{ol} is then evaluated as the ratio of the simulated capacitance to the theoretically evaluated capacitance assuming a simple parallel plate expression with no fringing effects. In order of find out S_{gc1} and S_{gc2}, similar simulations are performed for in-plane gap closing capacitors. Six of in-plane gap closing capacitors are shown in Figure 2-26 (b). According to Figure 2-27, S_{ol} is found out to be 4.15, S_{gc1} is 5.85 and S_{gc2} is 6.84. C_{para1}, C_{para2} are chosen as 1.10 pF, 0.70 pF respectively based on experimental readings.

Back simulation results with the scaling factors are shown in Figure 2-28. The peak to peak values of generated ac voltage across R_1 and R_2 are 0.700 V and 0.800 V respectively. These simulated values agree well with the measured data.

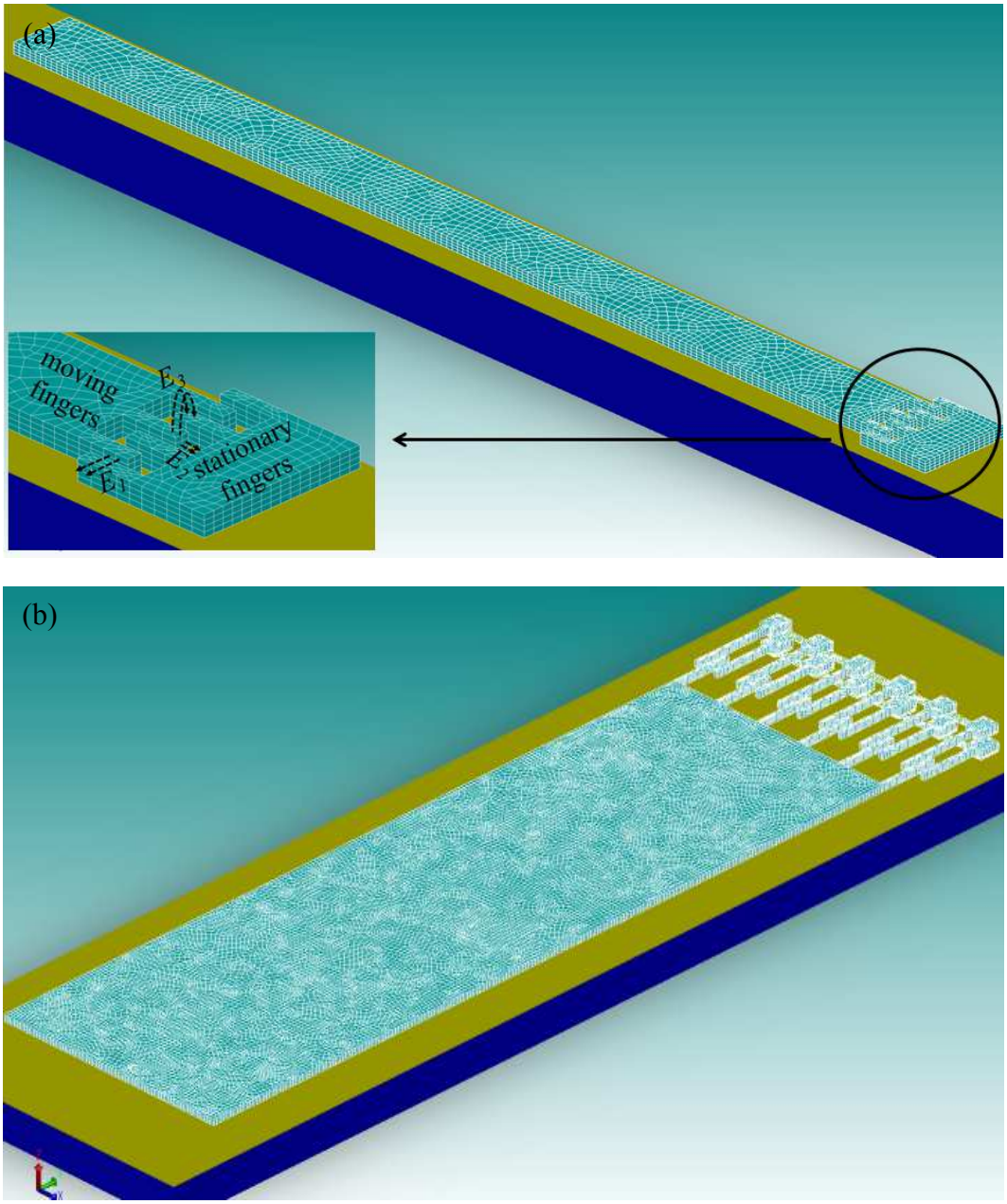

Figure 2-26 (a) Six of in-plane overlap capacitors with electric fields, and (b) gap closing capacitor groups.

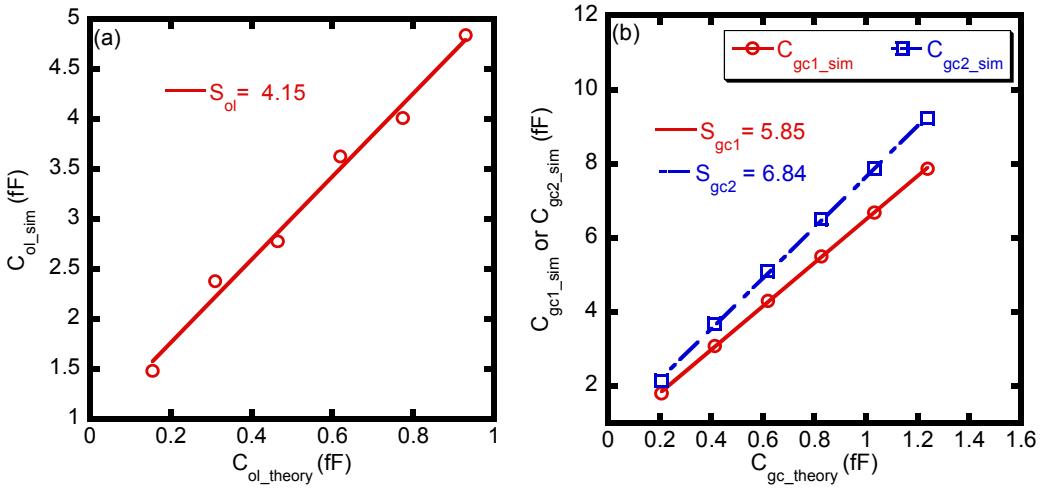

Figure 2-27 The capacitance scaling factors (a) S_{ol} and (b) S_{gc1}, S_{gc2} are extracted from the ratio of simulated capacitance values with the fringing effect to the classical parallel-plate capacitance.

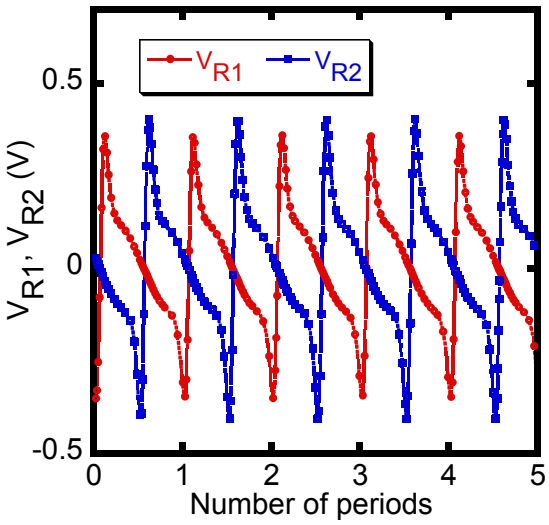

Figure 2-28 Simulation results for the revised model: V_{R1}, V_{R2} at 1.90 kHz with an acceleration magnitude of 8g (5 MΩ R_1, R_2, 1 μF C_{bias} and 6 V V_{bias}).

2.4.5 Impact of Bias Voltage

Since charge leakage takes place on the bias capacitor, V_{R1} and V_{R2} gradually decrease to zero. In order to provide a constant charge, the measurements were repeated with the 6 V dc source connected across the bias capacitor. Figure 2-29 shows a higher ac peak to peak output voltage of 1.20 V and 1.50 V across R_1 and R_2, respectively, compared to 0.800 V and 0.900 V in Figure 2-25 (a) with the bias voltage source disconnected.

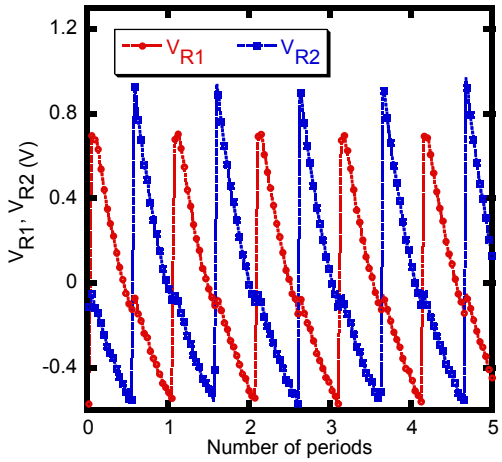

Figure 2-29 Generated peak-to-peak ac voltage across R_1 and R_2 is about 1.20 V and 1.50 V, respectively at 1.90 kHz with an acceleration magnitude of 8g (6V dc bias voltage source is connected).

2.4.6 Statistical Analysis of Measurements

In order to gain statistical information, six devices were characterized. According to Figure 2-30, average ac peak to peak value for V_{R1} and V_{R2} is 0.800 V and 0.900 V. Standard deviations are 27% and 32% from the average values.

The possible reason for a relatively higher average value of V_{R2} is that C_2 probably experiences a larger change of capacitance. C_2 includes in-plane gap closing

capacitors with longer stationary fingers, therefore scaling factor S_{gc2} is relatively higher than S_{gc1} which results in more contribution from fringing field capacitance. The relatively high standard deviation is most likely related to processing variations, especially electroplating, as it is difficult to control the thickness of nickel layer precisely.

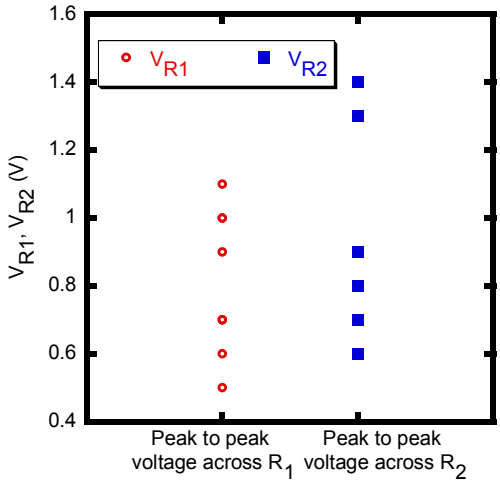

Figure 2-30 Statistical analysis of V_{R1} and V_{R2} at 1.90 kHz with an acceleration magnitude of 8g (6V dc bias voltage source is disconnected).

2.4.7 Comparison of State-of-the-art Designs

Table 2-10 is a comparison of results reported here and other state-of-the-art designs predicted or experimentally observed. The presented device achieved a power density of 2.07 x 10^4 μW/cm^3 which is competitive among this group of designs. According to aforementioned simulations, this hybrid structure design can achieve much higher output power compared to the single mode design incorporating only either in-plane overlap or gap-closing motion. From the fabrication point of view, UV-LIGA allows thickness control which is not available for SOI technologies in the table.

Table 2-10 Comparison table of state-of-the-art designs.

Source	Model	Volume (cm^3)	Material	Input Acceleration (m/s^2)	Input frequency (Hz)	Bias voltage (V)	Power (μW)	Power density-PD ($\mu W/cm^3$)	PD/A^2 ($\mu Ws^4\ cm^{-3}\ m^{-2}$)[a]	Observed/ predicted
This work	In-plane overlap and gap closing	1.40×10^{-5}	Ni	7.84×10^{1}	1.90×10^{3}	6	2.90×10^{-1}	2.07×10^{4}	3.37	O
2	In-plane gap closing		SOI	2.25	1.20×10^{2}	10		1.16×10^{2}	2.29×10^{1}	P
38	In-plane overlap	5.63×10^{-4}*	SOI		9.10×10^{2}	73	5.00×10^{1}	8.88×10^{4}*		P
39	In-plane overlap	5.20×10^{-4}*	SOI	1.64×10^{2}	9.11×10^{2}	150	5.00×10^{1}	9.62×10^{4}*	3.58	P
40	In-plane overlap		SOI	1.27×10^{2}	$1.3–1.5 \times 10^{2}$	50	3.50			O
41	In-plane overlap	4.40×10^{-3}*	SOI		1.05×10^{2}		9.24×10^{-2}	2.10×10^{1}		P
42	Out of plane gap closing	3.50×10^{-4}	SU-8		1.10×10^{2}	6	1.12×10^{-2}*	3.20×10^{1}		P
43	Out of plane overlap	1.98×10^{-2}*	Si/glass	2.45	2.50×10^{2}	6	6.10×10^{-2}	3.08*	5.13×10^{-1}	O

*Calculated from the given information in the referenced paper.

2.5 Summary

A novel, hybrid capacitive electrostatic energy harvester is fabricated utilizing in-plane overlap as well as in-plane gap closing variation modes simultaneously to maximize the vibration conversion efficiency. MATLAB simulation is employed to optimize the harvester geometry for the highest power. Under external acceleration magnitude of 8g, 0.800 V peak-to-peak ac output voltage is detected across a 5 MΩ load resistor at the resonant frequency of 1.90 kHz (6 V dc source was used to pre charge the 1 μF bias capacitor). The non-uniformity of the electroplated nickel layer was the primary reason for the observed 30% standard deviation from device to device. The power density of this novel design ranks in third place among seven other state-of-the-art designs. Some designs with higher power or power density require a higher polarizing voltage for the bias capacitors.

In the current design, a dc bias voltage source is used to provide initial charges in the system to prove this design idea. Further work includes embedding the pre-charged electret into the system to realize a more practical application.

Chapter 3

Piezoelectric Zinc Oxide Nanowire Micro Energy Harvester

3.1 Introduction

Nanosystems have numerous applications including medical, military and commercial fields for their capability of sensing and actuating. Self-powered nanosystems exhibit enormous advantages compared to conventional battery supported ones. On one hand, the total size and weight can be greatly reduced due to the elimination of the battery. On the other hand, its maintenance-free feature helps to ease the time and inconvenience caused by the replacement of the battery. This benefit is even more attractive when the nanosystem is applied in implantable biomedical fields. In order to realize self-powered nanosystems, micro energy harvesters are developed to harness the environmental waste energy, furthermore to convert into electricity [44, 45, 46, 47].

Photovoltaic [48, 49], thermal [50, 51] or electromagnetic radiation [52] energy harvesters have been widely utilized. Under the circumstance that above energy sources in surrounding environment are not sufficient or stable whereas mechanical vibrations are available, vibrational energy harvesting is a good option. Vibrations from a running car, helicopter or portable home air compressor are all alternative sources for energy harvesting [53, 54, 55, 56].

Piezoelectric, electrostatic [57] or electromagnetic [58, 59] are three major mechanisms for mechanical vibration energy harvesters. Piezoelectric energy harvester is based on piezoelectric effect of materials which can generate distributed electrical charges due to mechanical strain [60]. Zinc oxide nanowire (NW) or nanorod structure exhibits excellent piezoelectricity due to the ability of reacting to small physical deflections. The bandwidth of excitation is typically wide from 1 Hz to several thousand

Hz, which can greatly expand application fields. A piezoelectric nanogenerator with zinc oxide nanowire has been first demonstrated by Z. Wang *et al* [61].

As for the design presented here, the micro energy harvester utilizes vertically aligned zinc oxide nanowires as the piezoelectric material. Mechanical stress or strain along *c*-axis is induced by a top attaching layer of suspended membrane proof-mass structure which vibrates in response to the external mechanical excitation. This design successfully integrates the low temperature growth process of crystalline zinc oxide nanowires and conventional MEMS surface micromachining technology. Another novelty is that this design is expected to have better reliability because nanowires are compressed and released by the membrane proof-mass structure, but are not in direct contact with the external vibration source. In this way, it protects nanowires from tear and wear due to repeated deformation.

3.2 Properties and Synthesis of Zinc Oxide Nanowire

3.2.1 Properties and Application of ZnO

ZnO is a compound of group II element, zinc, and group VI element, oxygen. By nature, pure ZnO is a white powder that can be produced in a synthesis process in most cases.

Crystalline ZnO is usually in hexagonal wurtzite structure (Figure 3-1) which is the most common and stable form [62]. Either zinc or oxygen forms a tetrahedral unit. The lattice constants of hexagonal structure are *a* = 0.330 nm and *c* = 0.520 nm. The cations Zn^{2+} and the anions O^{2-} form an ionic bond. According to Figure 3-1, electrically positive charged zinc planes (0001) and negative charged oxygen planes $(000\bar{1})$ form alternatively along *c*-axis. These charged surfaces are called polar surfaces which construct a dipole moment and polarization. This feature accounts for the strong piezoelectric effect of ZnO. ZnO has many kinds of nanostructures including nanowire,

nanorod, nanobelt etc. as shown in Figure 3-2 [63]. The top surface is the polar surface (0001) which is perpendicular to the fast growth direction ± [0001]. ZnO nanowire or nanorod structure is attractive because it can be realized using low temperature chemical methods compatible with flexible substrate or conventional silicon fabrication processes.

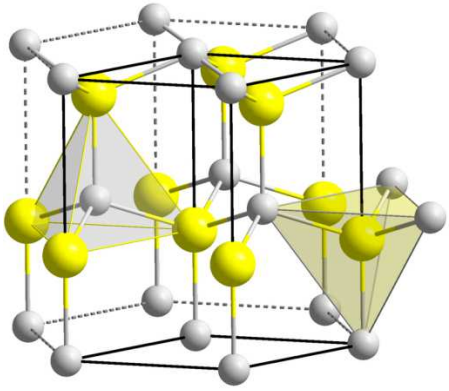

Figure 3-1 Hexagonal Wurtzite structure of ZnO. White ball represents Zn^{2+}. Yellow ball represent O^{2-} [62].

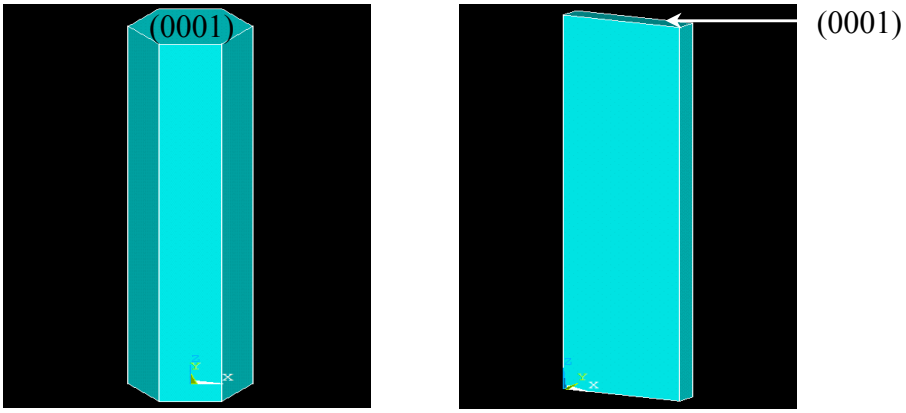

Figure 3-2 ZnO nanowire/nanorod/nanobelt [63].

ZnO is a direct band gap semiconductor material with a wide band gap of 3.3 eV at room temperature. Therefore ZnO can endure high electric fields or power applications

with a large breakdown voltage. Some of the optoelectronic applications are laser diodes and light emitting diodes since ZnO has a large exciton binding energy which makes excitonic process persist at room temperature [64, 65]. ZnO nanorods can also be used as a field emitter due to the strong electric field accumulated on the sharp tips [66]. Front contact of solar cell can be produced by aluminum doped ZnO since it can function as good transparent electrodes [67]. Hydrogen gas sensors can be realized by ZnO nanorod as well, that respond to the absorption of hydrogen molecules by change in the electrical current flowing through [68, 69].

3.2.2 Synthesis Process for ZnO Nanostructure

3.2.2.1 Vapor-Solid Process

ZnO nanowire/nanobelt can be synthesized by a vapor-solid process. ZnO powder is first evaporated into a gas phase in a high temperature furnace, and then condensed to from a crystalline nanostructure. The advantage of this method is that no catalyst is needed. Figure 3-3 shows the equipment for the vapor-solid process [63].

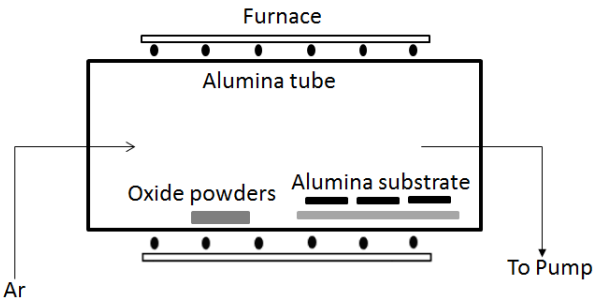

Figure 3-3 Equipment for the vapor-solid process [63].

3.2.2.2 Vapor-Liquid-Solid Process

Another method for synthesis of ZnO nanowires is vapor-liquid-solid (VLS) process which is typically used for one dimensional nanostructure growth. Unlike the vapor-solid process, a catalyst in liquid alloy phase is introduced that absorbs ZnO vapor,

and precipitates nucleation. This speeds up the crystalline nanostructure growth. Therefore, the properties of the liquid catalyst control the aspects of the resultant nanostructure. Figure 3-4 explains the basic steps of the VLS process [70].

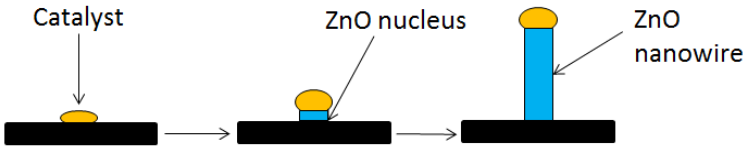

Figure 3-4 Basic steps of VLS process [70].

3.2.2.3 Pulsed Laser Deposition

ZnO nanowires growth can also be realized by a pulsed laser deposition (PLD) process. Typically this process is used for thin film deposition during which high energy laser beam strikes the zinc target within the chamber filled with oxygen gas. A vaporized plasma is formed and deposited on the substrate. Figure 3-5 shows the schematic view of the PLD system [71]. Deposition conditions such as substrate temperature and chamber pressure control the morphology of the nanostructure.

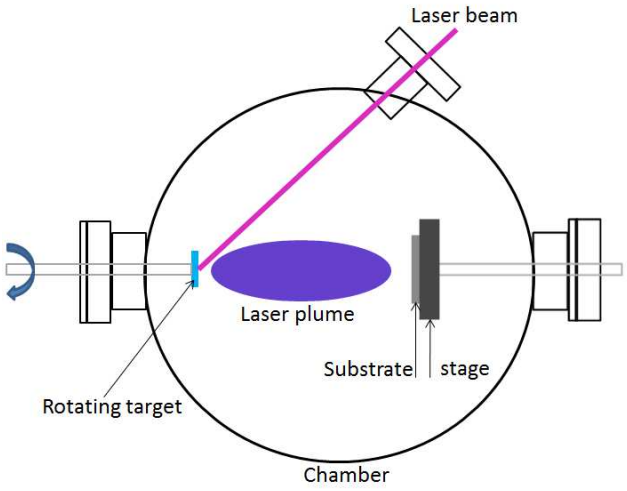

Figure 3-5 Schematic view of the PLD system [71].

3.2.2.4 Our Approach- Hydrothermal Growth

Compared to the methods discussed above, hydrothermal growth is commonly used for low temperature processing. One advantage is that by utilizing a ZnO seed layer either in the form of nanoparticles or thin film, growth process does not depend on the type of substrate. The other benefit is that it can be processed at low temperatures, which is attractive for compatibility with conventional silicon fabrication technology, and plastic substrates.

The most common chemicals used for hydrothermal growth are zinc nitride and hexamethylenetetramine (HMTA) [72, 73]. Zinc nitride supplies Zn^{2+} ions. O^{2-} ions come from the water molecules. HMTA slowly hydrolyzes and gradually produces OH^-. HMTA assists nanowire/nanorod crystallization along fast growth direction *c*-axis by acting as a polymer, preferentially attaching to non-polar surfaces. This can prohibit Zn^{2+} ions from landing on the non-polar surfaces. Therefore, the polar surface (0001) is supplied with enough Zn^{2+} and nanowires will continue to grow in the direction [0001] [74, 75]. This process is governed by [63]:

$$(CH_2)_6 N_4 + 6\,H_2O \leftrightarrow 4\,NH_3 + 6\,HCHO \tag{3.1}$$

$$NH_3 + H_2O \leftrightarrow NH_3 \cdot H_2O \tag{3.2}$$

$$NH_3 \cdot H_2O \leftrightarrow NH_4^+ + OH^- \tag{3.3}$$

$$Zn^{2+} + 2\,OH^- \leftrightarrow Zn(OH)_2 \tag{3.4}$$

$$Zn(OH)_2 \leftrightarrow ZnO + H_2O \tag{3.5}$$

ZnO seed layer is realized by the PLD process. A laser with a wavelength of 248 nm and energy of 500 mJ at O_2 environment is used to strike at a 99.999 % purity ZnO target to deposit the ZnO seed layer. The chamber pressure is kept at 100 mTorr. Laser

repetition rate is 10 Hz. A 400 nm thick ZnO thin film forms on the 3" silicon substrate heated to 300 ^{o}C during 10 mins of deposition. Figure 3-6 shows the SEM picture of the top view of a 400 nm thick ZnO seed layer deposited under the above conditions.

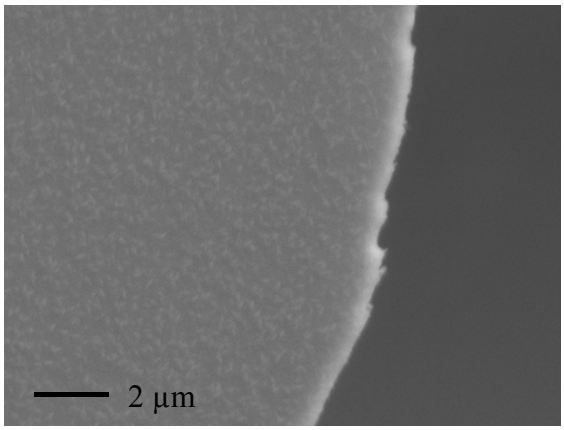

Figure 3-6 SEM picture of the top view of a 400 nm thick ZnO seed layer fabricated by PLD process.

After ZnO seed layer deposition, equimolar solution of 20 mM zinc nitride and HMTA are prepared for the nanowire growth. Several conditions including chemical concentration, solution temperature and growth time play an important role in determining the density, diameter, aspect ratio, and morphology of the nanowire. It has been observed that the diameter of the resultant nanowire increases when the concentration increases. The solution temperature is kept at 85 ^{o}C during the whole 3-hour growth period. Besides the above well-known conditions, maintaining a close contact between the silicon wafer and the nutrient solution is also important. In order to keep the silicon wafer steadily floating on the surface of the solution, a lid of 2" wafer box used as the floating assistant is attached to the 3" silicon wafer by tapes. The wafer is then put facing down into the solution.

3.2.2.5 Photoresist Template for ZnO Nanowire Growth

In order to control growth area of the nanowire, one solution is to pattern the ZnO seed layer. Another option is to use the negative photoresist such as NR1500 or SU-8 as a template to define an opening area for ZnO NW growth. The ZnO seed layer is not patterned in the latter approach. Figure 3-7 shows the nanowire growth directly on top of the patterned seed layer. One potential problem with this method is that non-orderly growth occurs on the silicon substrate that might impact the electrical conductivity if it happens between separate metal lines, thus causing a short.

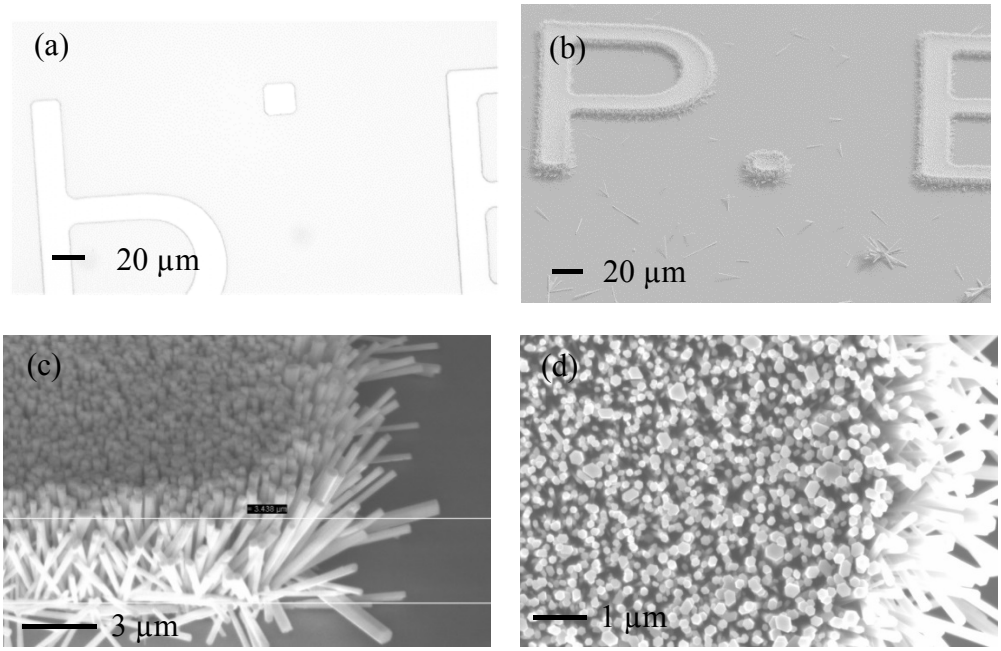

Figure 3-7 (a) A patterned ZnO seed layer on a silicon substrate. (b) NW growth on top of the seed layer. (c) NWs with the height of 4.5 μm, and (d) the diameter of 250 nm.

Figure 3-8 shows a 500x500x1.7 μm NR1500 opening area on top of a 500x500 μm patterned seed layer. No nanowire growth occurs in the overlapping area between the opening area and the seed layer. NR1500 photoresist template has been destroyed

in the heated nutrient solution during the 3-hour growth, as the photoresist is not thermally stable enough to endure 85°C growth solution for such a long time.

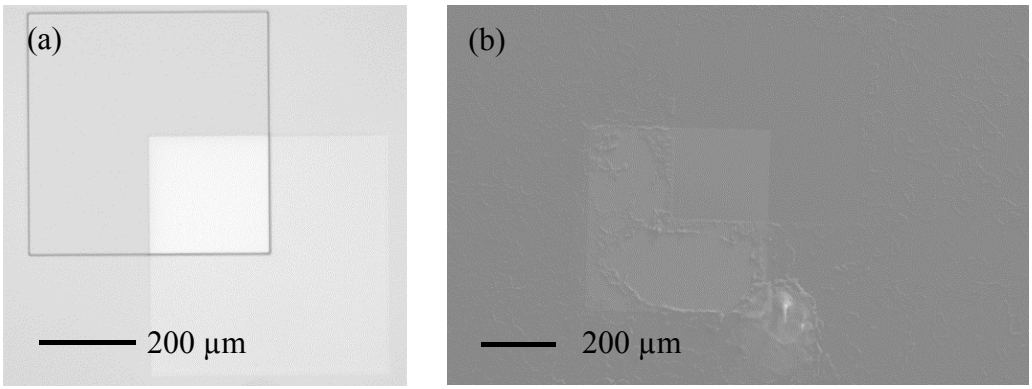

Figure 3-8 (a) A 500x500x1.7 µm NR1500 opening area on top of a 500x500 µm seed layer. (b) No NW growth in the overlapping area.

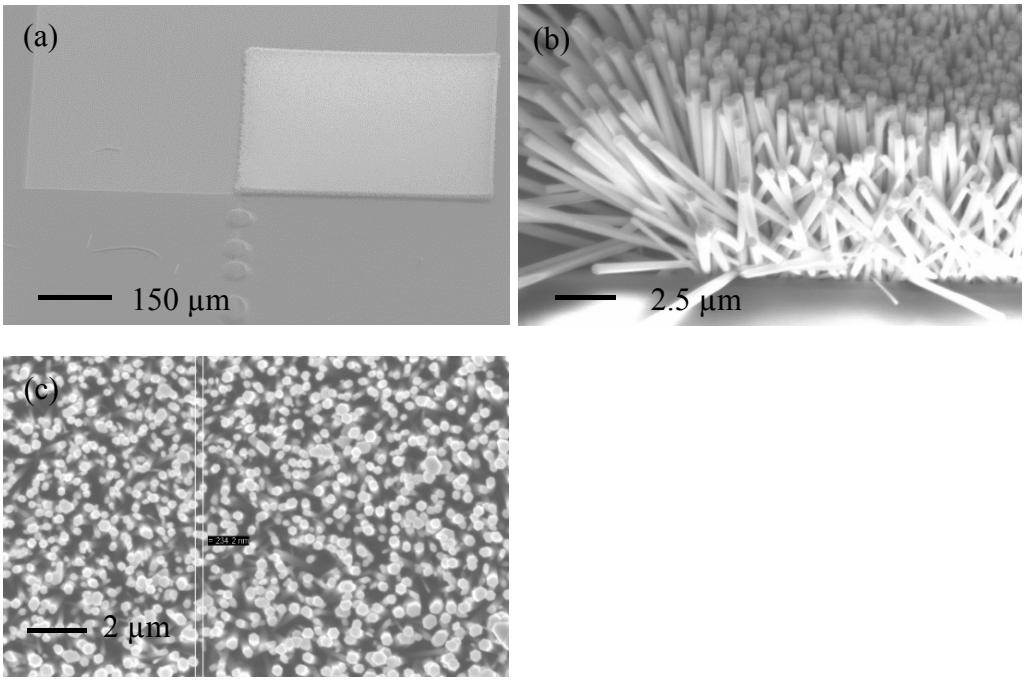

Figure 3-9 (a) SEM picture for 500x500x1.7 µm SU-8 opening area on top of a 500x500 µm seed layer. (b) NWs with the height of 5 µm. (c) NWs with the diameter of 234 nm.

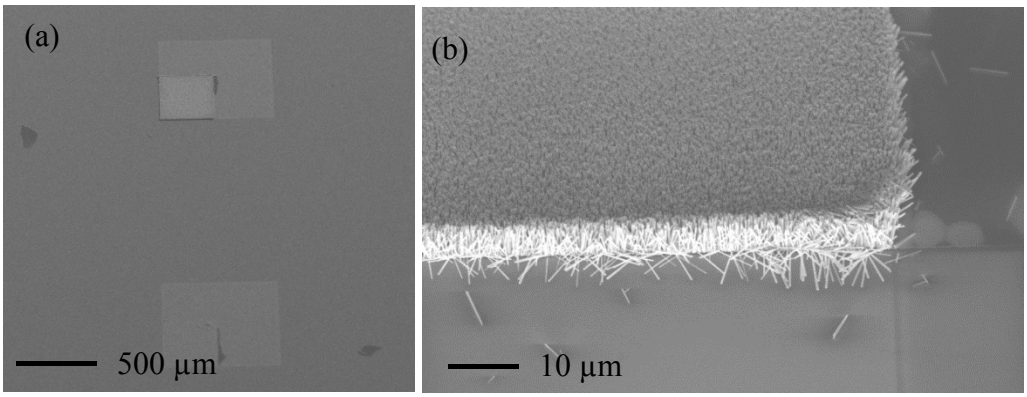

Figure 3-10 (a) SEM picture after SU-8 is removed in 1165 remover. (b) Zoom in picture of the NW block edge.

Aligned nanowires with the height of 5 µm and the diameter of 234 nm grow in the overlapping area of 500x500x1.7 µm SU-8 opening area on top of the 500x500 µm seed layer (Figure 3-9). This proves that SU-8 is a suitable template for nanowire growth. SU-8 is furthermore removed in heated 1165 remover for 30 mins. Figure 3-10 shows SEM picture after SU-8 is removed.

3.2.3 Piezoelectricity of ZnO Nanowire

3.2.3.1 Bending of ZnO Nanowire

The piezoelectric effect of a material is due to the lack of inversion symmetry in its lattice structure, which leads to electromechanical interaction between the electrical and mechanical status. It is an exchangeable process. Electrical charges accumulate in the material once mechanical strain exists; on the other hand, electric field applied to material can result in mechanical strain. This effect can be explained mathematically by [76]:

$$\begin{cases} \sigma_p = c_{pq}\varepsilon_q - e_{kp}E_k \\ D_i = e_{iq}\varepsilon_q + \kappa_{ik}E_k \end{cases} \tag{3.6}$$

where, σ is mechanical stress matrix (Pa), c is elastic constant matrix (GPa), ε is mechanical strain matrix, e is piezoelectric coefficient matrix (C/m^2), E is electric filed (V/m), D is electric displacement (C/m^2), κ is dielectric constant matrix (F/m). ε_0 is vacuum permittivity. Their respective values for bulk or thin film ZnO are given by the matrix below [76]:

$$c_{pq} = \begin{pmatrix} c_{11} & c_{12} & c_{13} & 0 & 0 & 0 \\ c_{12} & c_{11} & c_{13} & 0 & 0 & 0 \\ c_{13} & c_{13} & c_{33} & 0 & 0 & 0 \\ 0 & 0 & 0 & c_{44} & 0 & 0 \\ 0 & 0 & 0 & 0 & c_{55} & 0 \\ 0 & 0 & 0 & 0 & 0 & \frac{c_{11}-c_{12}}{2} \end{pmatrix} = \begin{pmatrix} 207 & 117.7 & 106.1 & 0 & 0 & 0 \\ 117.7 & 207 & 106.1 & 0 & 0 & 0 \\ 106.1 & 106.1 & 209.5 & 0 & 0 & 0 \\ 0 & 0 & 0 & 44.8 & 0 & 0 \\ 0 & 0 & 0 & 0 & 44.6 & 0 \\ 0 & 0 & 0 & 0 & 0 & 44.65 \end{pmatrix},$$

$$e_{kp} = \begin{pmatrix} 0 & 0 & 0 & 0 & e_{15} & 0 \\ 0 & 0 & 0 & e_{15} & 0 & 0 \\ e_{31} & e_{31} & e_{33} & 0 & 0 & 0 \end{pmatrix} = \begin{pmatrix} 0 & 0 & 0 & 0 & -0.45 & 0 \\ 0 & 0 & 0 & -0.45 & 0 & 0 \\ -0.51 & -0.51 & 1.22 & 0 & 0 & 0 \end{pmatrix},$$

$$\kappa_{ik} = \begin{pmatrix} \kappa_{11} & 0 & 0 \\ 0 & \kappa_{22} & 0 \\ 0 & 0 & \kappa_{33} \end{pmatrix} = \begin{pmatrix} \kappa_{\perp} & 0 & 0 \\ 0 & \kappa_{\perp} & 0 \\ 0 & 0 & \kappa_{\square} \end{pmatrix} = \begin{pmatrix} \varepsilon_0 \times 7.77 & 0 & 0 \\ 0 & \varepsilon_0 \times 7.77 & 0 \\ 0 & 0 & \varepsilon_0 \times 8.91 \end{pmatrix}.$$

Instead of anisotropic elastic constants, equivalent isotropic values are used for the following FEM analysis with modulus E_M of 129 GPa and Poisson ratio v of 0.349. The validity of this approximation has been shown by Y. Gao *et al* [76].

Typically two parameters are considered in the piezoelectric effect of a nanowire. One is the piezoelectric potential distribution along the cross section surface due to bending. The other is the electrostatic potential distribution along *c*-axis due to compressing or stretching. Theoretical calculations have been done for the case of a nanowire pushed by the lateral force f_y on the tip. For a single nanowire with radius *a*,

and length *l*, the electrical potential *φ(r, θ)* (in cylindrical coordinates) along the cross section surface is given by [76]:

$$\varphi = \begin{cases} \dfrac{f_y}{8\kappa_\perp I_{xx} E_M}[2(1+\nu)e_{15} + 2\nu e_{31} - e_{33}][\dfrac{\varepsilon_0 + 3\kappa_\perp}{\varepsilon_0 + \kappa_\perp}\dfrac{r}{a} - \dfrac{r^3}{a^3}]a^3 \sin\theta & (r < a) \\ \dfrac{f_y}{8\kappa_\perp I_{xx} E_M}[2(1+\nu)e_{15} + 2\nu e_{31} - e_{33}][\dfrac{2\kappa_\perp}{\varepsilon_0 + \kappa_\perp}\dfrac{a}{r}]a^3 \sin\theta & (r \geq a) \end{cases} \quad (3.7)$$

where, I_{xx} is area moment of inertia $I_{xx} = \pi a^4 / 4$. The maximum potential occurs at the location where $r = a$. For the tensile side, θ = -90°; for the compressive side, θ = 90°. The electrical potential distribution for a nanowire (a = 150 nm, l = 2 μm) under a lateral force of 1 μN in y direction is computed using FEM in ANSYS (Figure 3-11 (a)). The compressive side shows a maximum electrical potential of -0.662 V, while the tensile side has a maximum value of 0.662 V which is approximately close to the theoretical calculation value of 0.592 V. Displacement in y direction is 54 nm (Figure 3-11 (b)).

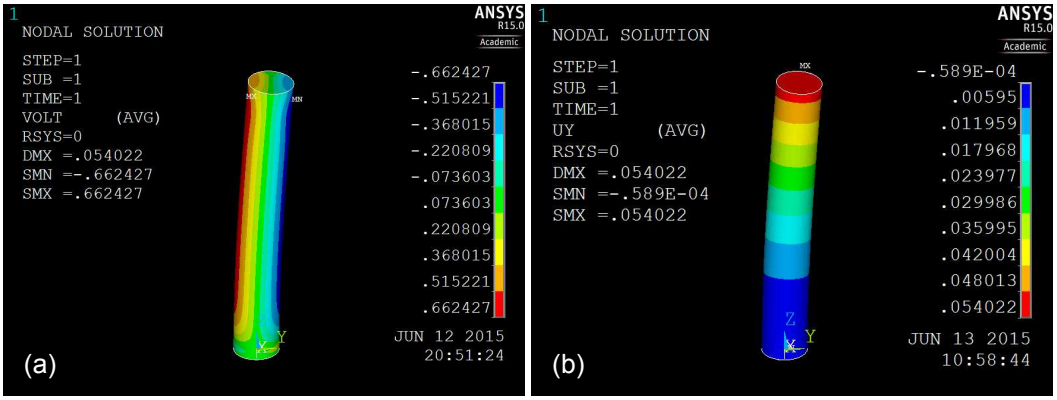

Figure 3-11 ANSYS simulation for ZnO NW (a = 150 nm, l = 2 μm) under lateral force of 1 μN in y direction. (a) Electrical potential distribution. (b) Displacement in y direction.

3.2.3.2 Compression of ZnO Nanowire

Another common type of mechanical deformation of ZnO NW is compression or stretching along *c*-axis. Figure 3-12 shows the electrical potential distribution in a single NW (diameter = 200 nm, length = 1200 nm) which is compressed by 0.020 nm on the top surface. The bottom surface is fixed and grounded. The maximum value of the electrical potential occurs on the top surface with a value of -0.394 V. A similar simulation has been reported by Z. Gao *et al* with a very close value of -0.400 V [77].

Based on above simulation results, in order to achieve a certain amount of electrical potential, deflection required in transvers direction is much higher than that in vertical direction, which is parallel to the polarization *c*-axis.

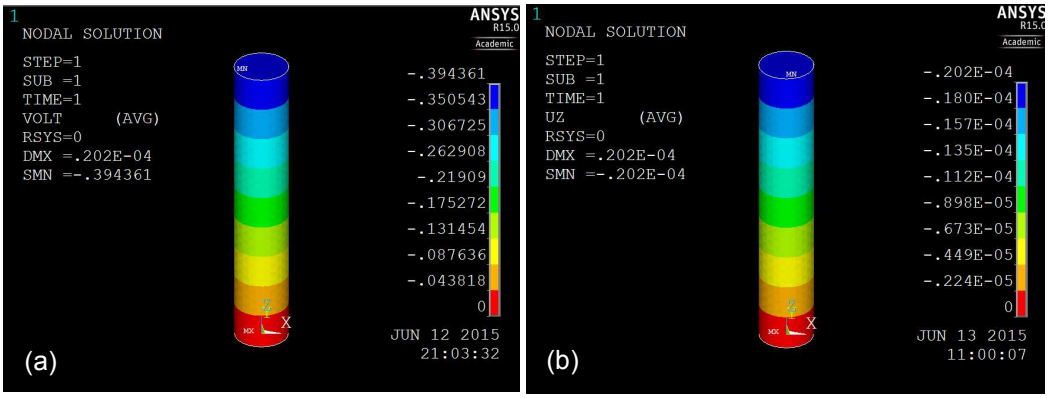

Figure 3-12 ANSYS simulation for a ZnO nanowire (diameter = 200 nm, length = 1200 nm) which is compressed by 0.020 nm on the top surface. (a) Electrical potential distribution. (b) Displacement in the *z* direction

3.3 Design and Structure

Based on the previous analysis for the piezoelectric properties of ZnO nanowires, several design structures for the piezoelectric energy harvesters utilizing the compression of the vertically aligned nanowires are presented. The following procedure is used to refer

to the different device structures. NW1-G refers to the design, where, there is a single ("1") patch of nanowires and Si_3N_4 is deposited in a grid ("G") structure (Figure 3-13 (a)). The cross section of such a device is shown in Figure 3-13 (b). On top of the ZnO seed layer, a solid ZnO block is used to represent a patch of NWs growing in a confined area defined by the photoresist template. A thick layer of polyimide is coated as the mechanical support material for the subsequent layers. The top and bottom electrodes connect to the top and bottom surfaces of the ZnO block, respectively. The top electrode connects to the metal lines on the substrate through an opening in the polyimide layer. The silicon substrate is covered by a layer of silicon nitride for the isolation purpose. The silicon nitride membrane is built on top of the NW block. Moreover, nickel layer is used as a proof-mass. Finally, the membrane proof-mass structure is suspended by ashing the polyimide sacrificial layer. Such a structure will compress the NWs in the *z* direction in response to the external vibration. The electrical potential difference between the top and bottom surface of NWs due to the piezoelectric effect will be collected by the top and bottom electrodes.

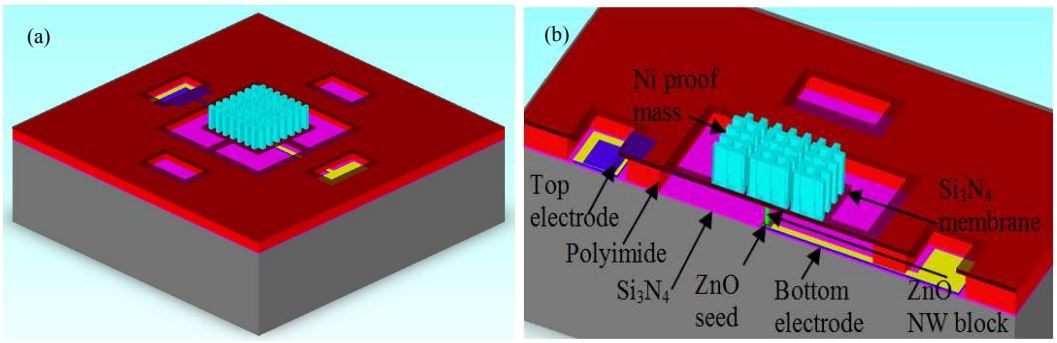

Figure 3-13 (a) Overview and (b) cross section of the piezoelectric micro energy generator NW1-G.

In order to increase the output voltage, several NW blocks can be connected in series. Device named as "NW4-G" has four NW blocks connected in series electrically

under a single proof-mass (Figure 3-14 (a)). Two “NW4-G” devices can be further connected in series (Figure 3-14 (b)) which is called “NW4-G-TWO” accordingly since it includes two “NW4-G” devices. Four NW blocks connected in clockwise sequence are shown in Figure 3-14 (c, d). The center NW block is a dummy one for balancing mechanical compression. Due to the increase of the number of NW blocks, higher equivalent stiffness causes the compressing of NWs more difficult. In order to compensate such a negative effect, the mass of the proof-mass needs to be increased.

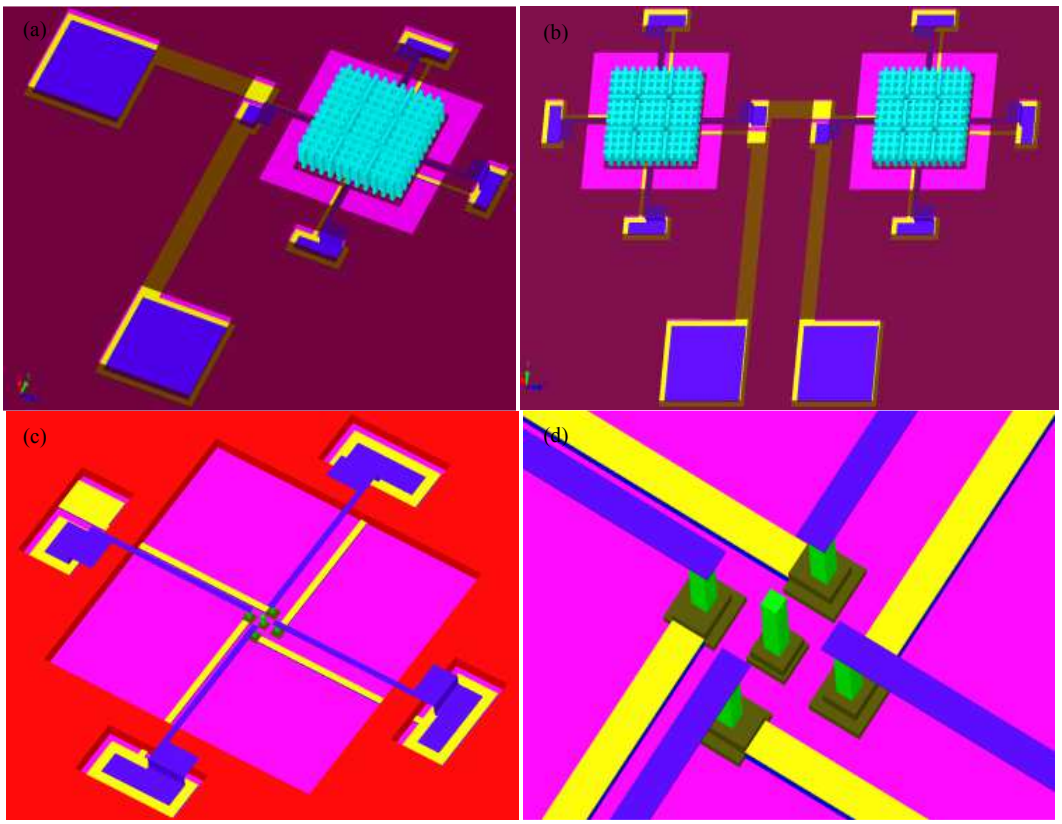

Figure 3-14 (a) Device NW4-G. (b) Device NW4-G-TWO. (c) Metal lines connection layout for NW4-G and (d) its zoom in picture.

Besides the above mentioned structures, Si_3N_4 can be deposited in diagonal structure as well. The similar devices with the name of “NW1-D” (Figure 3-15 (a)), “NW4-

D" (Figure 3-15 (b)), and "NW4-D-TWO" (Figure 3-15 (c)) are presented as well. The metal lines connection layout for NW4-D is shown in Figure 3-15 (d). Based on the fabrication results, the detailed values of design parameters are listed in Table 3-1.

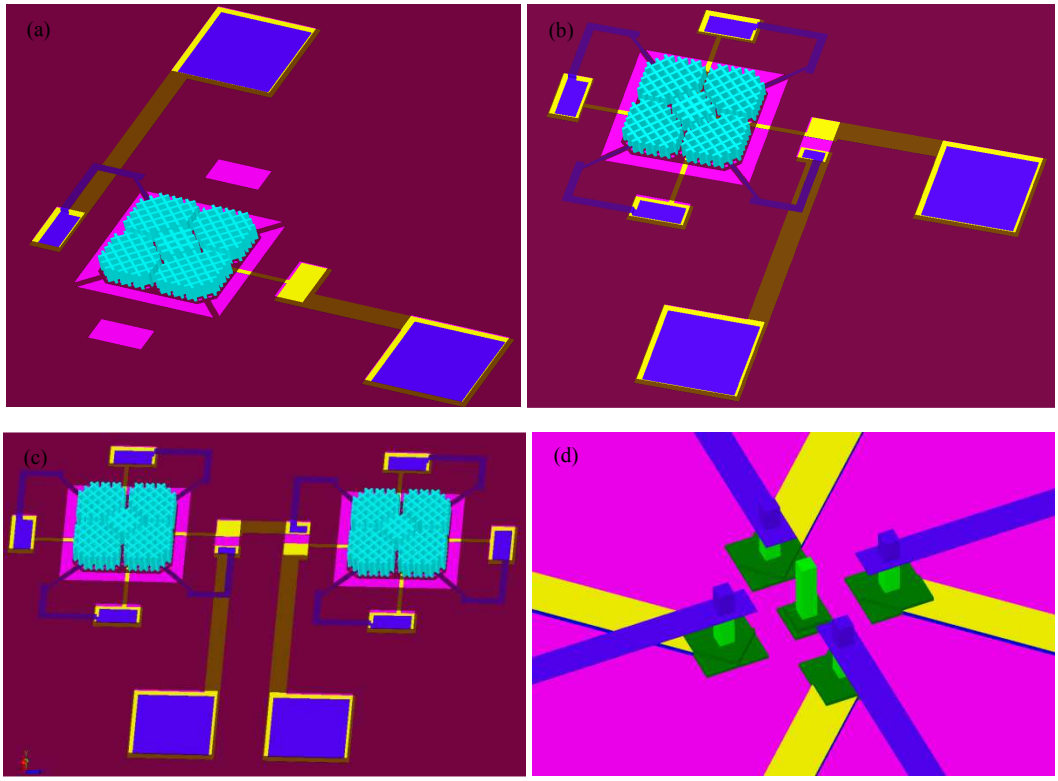

Figure 3-15 (a) Device NW1-D. (b) Device NW4-D. (c) Device NW1-D-TWO. (d) Metal lines connection layout for NW4-D. Note that *z* scale is exaggerated.

Table 3-1 Piezoelectric micro energy harvester design details

Design name	NW block			Spring			Ni thickness (μm)
	Size (μm)	Height (μm)	Tip exposure length (μm)	Width (μm)	Length (μm)	Thickness (μm)	
NW1-G	8x8	5	0	36	124	1.3	10
NW4-G, NW4-G-TWO	8x8	5	0	36	124	1.3	10
NW1-D	8x8	7	2.70	28	126	1.3	20
NW4-D, NW4-D-TWO	8x8	7	2.70	28	126	1.3	20

3.4 FEM Analysis

The simulation for the mechanical displacement of the NW block is done when the device has been excited by 1.4g acceleration in z direction. The solid model used in the simulation includes Ni layer, Si_3N_4 layer, top electrode layer and NW block layer. Anisotropic elastic constant of bulk ZnO can be approximately represented by the equivalent isotropic one as discussed before. Both the bottom surface of the NW blocks and the anchoring area of the top electrodes are fixed mechanically. The mechanical displacement of the NW blocks for NW1-G and NW4-G in the *z* direction is shown in Figure 3-16 (a,c). The von Mises stress of NW1-G and NW4-G is shown in Figure 3-16 (b,d).

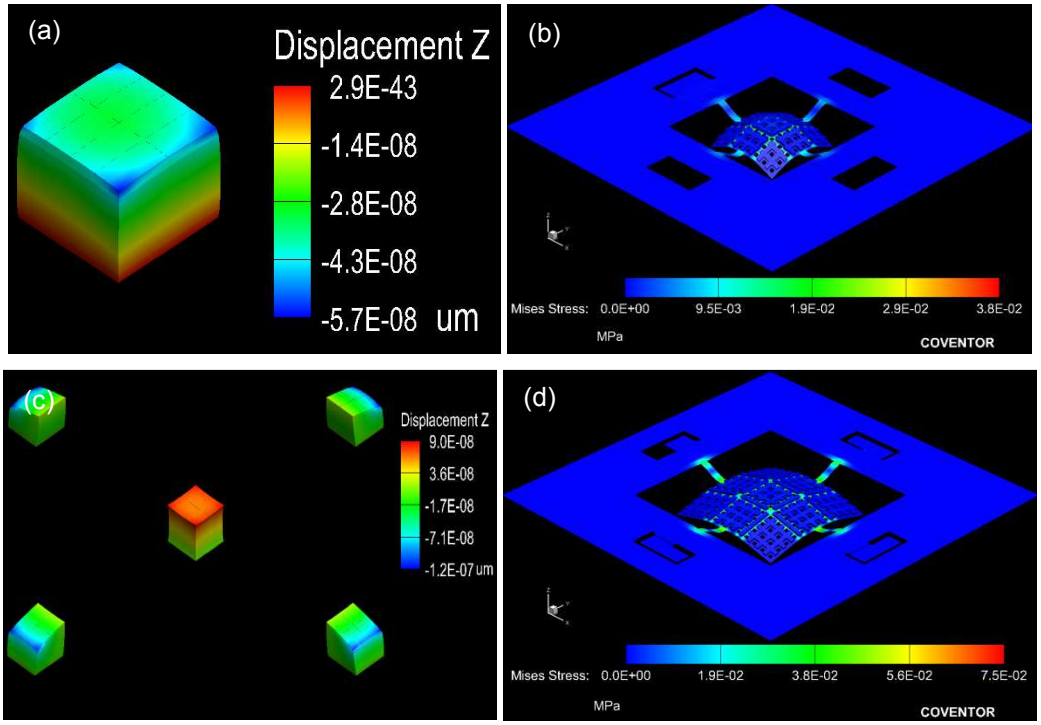

Figure 3-16 FEM analysis for device under 1.4g acceleration in the *z* direction. The displacement of NW blocks in the *z* direction for (a) NW1-G (c) NW4-G. The von Mises stress contour for device (b) NW1-G (d) NW4-G.

The mechanical displacement of the NW blocks for NW1-D and NW4-D in the *z* direction is shown in Figure 3-17 (a,c). The von Mises stress of NW1-D and NW4-D is shown in Figure 3-17 (b,d).

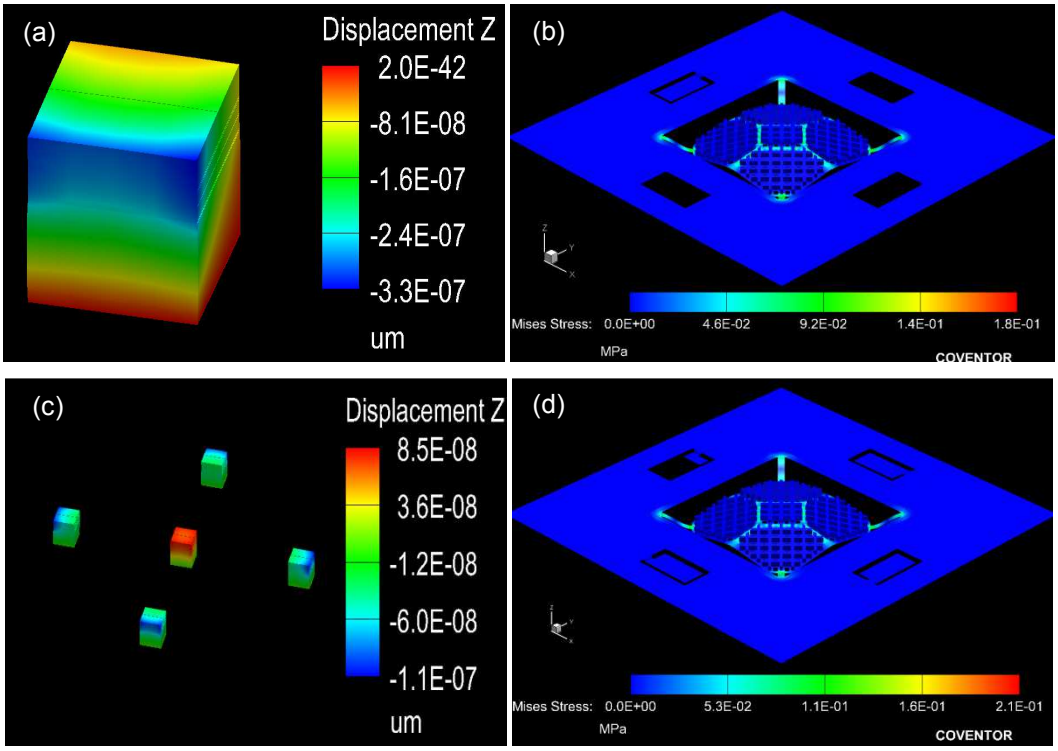

Figure 3-17 FEM analysis for device under 1.4g acceleration in the *z* direction. The displacement of NW blocks in the *z* direction for (a) NW1-D (c) NW4-D. The von Mises stress contour for device (b) NW1-D (d) NW4-D.

Except for device NW1-G that shows even displacement on four corners, the NW blocks of other devices are compressed unequally. Especially for the four NW blocks connecting in series case, the center NW block has been pulled up. This block serves no sensing purpose. The function of this block is to alleviate the unequal compression of the other four blocks. Device NW1-D exhibits the highest displacement due to the heavier

proof-mass. The maximum von Mises stress is well below tensile strength of thin film Si_3N_4 which is 6.4 GPa [78].

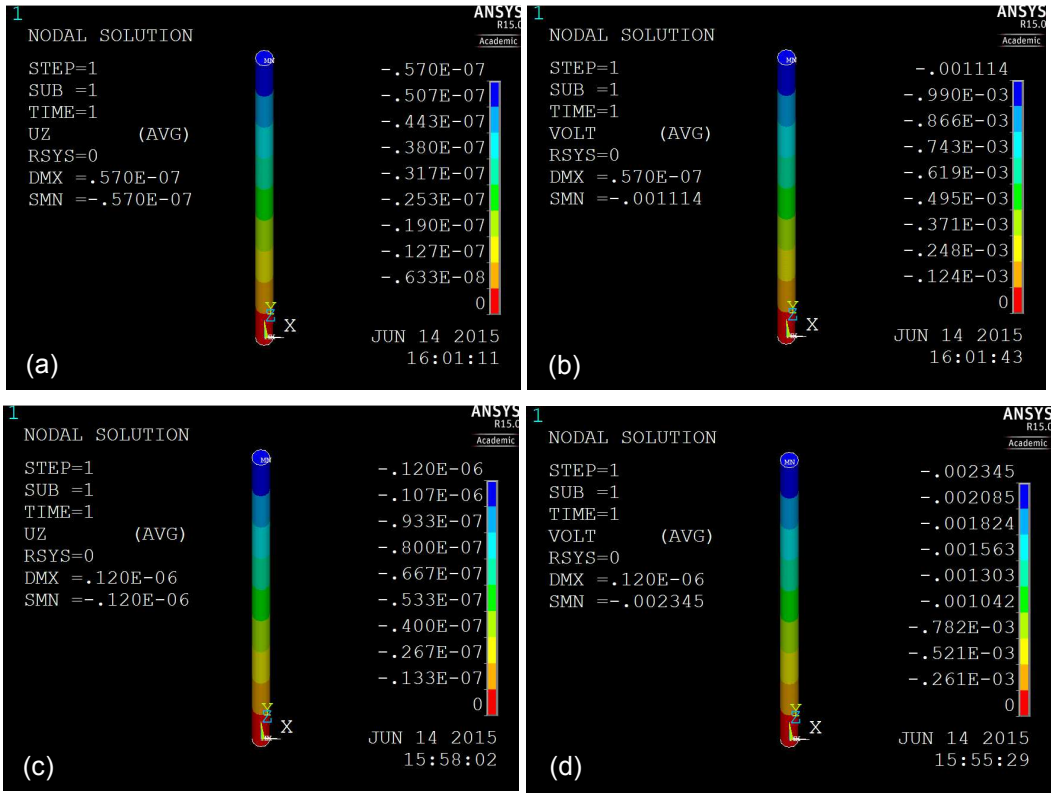

Figure 3-18 ANSYS analysis for a single NW under compression. Displacement in the *z* direction for device (a) NW1-G, (c) NW4-G. Electrical potential distribution for device (b) NW1-G, (d) NW4-G.

Furthermore, a single NW is modeled in ANSYS to estimate the electrical potential distribution along the *c*-axis direction when it is compressed based on the displacement values resulting from the mechanical simulations discussed above. The boundary conditions are that the bottom surface of the NW is fixed mechanically and grounded electrically. The top surface is compressed. The linear piezoelectric coefficient and the relative dielectric constant are defined according to the previous discussion.

Figure 3-18 shows the electrical potential distribution and displacement in *z* direction for a single NW under compression. Devices NW1-G (Figure 3-18 (a, b)) and NW4-G (Figure 3-18 (c, d)) were represented by a single NW with the height of 5 μm and the diameter of 150 nm.

Devices NW1-D (Figure 3-19 (a, b)) and NW4-D (Figure 3-19 (c, d)) were represented by a single NW with the height of 7 μm and the diameter of 250 nm. Based on the fabrication results, here the sizes of NW are different from the device NW1-G and NW4-G. Table 3-2 summarizes the simulation results for all devices.

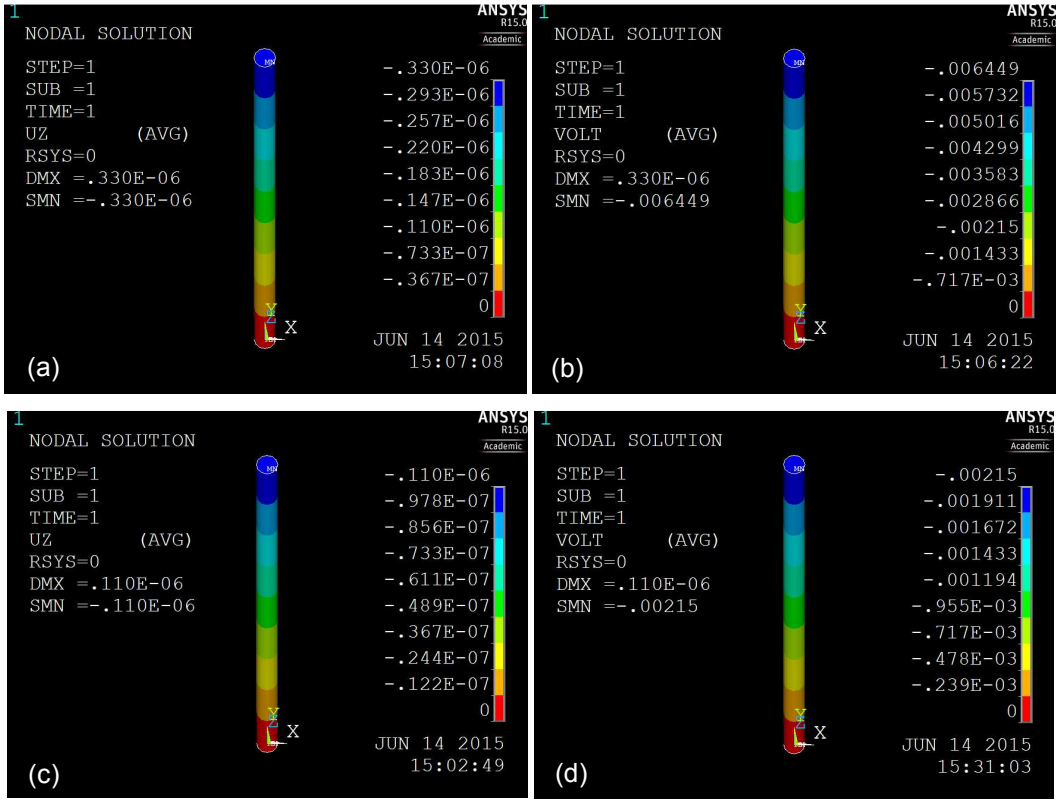

Figure 3-19 ANSYS analysis for a single NW under compression. Displacement in the *z* direction for device (a) NW1-D, (c) NW4-D. Electrical potential distribution for device (b) NW1-D, (d) NW4-D.

Table 3-2 Simulation results for the mechanical displacement and electrical potential

Device	CoventorWare simulation		ANSYS simulation for single NW		
	Mass of proof-mass (kg)	Max displacement (μm)	NW height (μm)	NW diameter (nm)	Electrical potential on top surface (mV)
NW1-G	6.05×10^{-9}	-5.70×10^{-8}	5	150	-1.11
NW4-G	1.41×10^{-8}	-1.20×10^{-7}	5	150	-2.34
NW1-D	2.56×10^{-8}	-3.30×10^{-7}	7	250	-6.45
NW4-D	2.56×10^{-8}	-1.10×10^{-7}	7	250	-2.15

Figure 3-16 shows the relation between the electrical potential on the NW top surface and compression in *z* direction. According to the fitting line, electrical potential is linearly proportional to the compression. Another interesting result is that electrical potential does not dependent on the NW size.

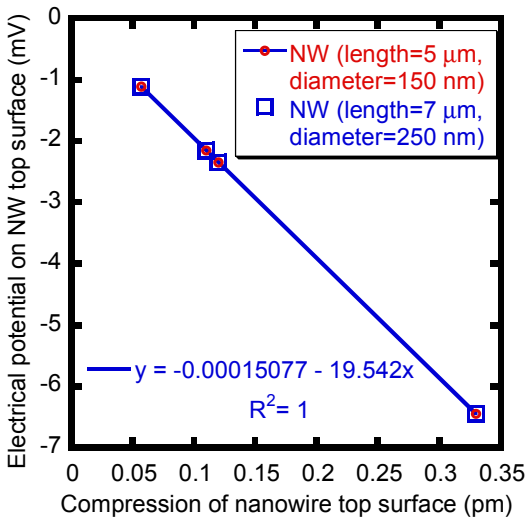

Figure 3-20 ANSYS simulation results for electrical potential on the NW top surface for different compression values in the *z* direction.

3.5 Fabrication

Fabrication is done in two batches in order to investigate the effect of different design parameters. Three steps including NW growth, polyimide layer fabrication and electroplating of Ni have been processed differently. For the first batch, fabrication process starts with a (100) silicon wafer. Next, a 0.4 μm thick silicon nitride is sputtered as an isolation layer (Figure 3-21 (a)). A 30 nm thick chrome adhesion layer plus a 100 nm thick gold layer are evaporated sequentially and patterned by liftoff as the bottom electrode (Figure 3-21 (b)). Thereafter, a 30 nm thick titanium is evaporated in order to form an Ohmic contact between ZnO and the bottom electrode. A thin layer of PLD-deposited ZnO seed layer is employed to assist the NW growth. A 400 nm thick seed layer is deposited on the silicon substrate heated to 300 ^{o}C in O_2 environment (the chamber pressure is 100 mTorr). The Ti and ZnO seed layer are patterned by hydrofluoric acid with positive photoresist S1813 as an etch mask (Figure 3-21 (c)).

Next, SU-8 photoresist is spin-coated and patterned to define the opening areas on top of the ZnO seed layer [79, 80]. Wafer is then put facing down into the growth solution mixed with 20 mM zinc nitrate and 20 mM hexamethylenetetramine (HMTA) heated to 85^{o}C [81, 82]. In order to achieve different length of NWs, one batch uses three hours growth time, another uses two hours growth time. SU-8 template is then removed in 1165 remover solution heated to 65^{o}C for 30 mins (Figure 3-21 (d)). Thereafter, NWs are embedded in the polyimide sacrificial layer which is further patterned for pad opening. O_2 plasma ashing has been carefully monitored. In one batch, 2.7 μm of the NW tips are exposed. In another batch, the tiny tips of NWs are exposed (Figure 3-21 (e)). A 30 nm thick titanium and 100 nm thick gold layer are patterned to connect to the top surface of NW block (Figure 3-21 (f)). NR9-3000 is used as the lift off photoresist to pattern a 1.3 μm thick sputtered silicon nitride membrane layer (Figure 3-21 (g)).

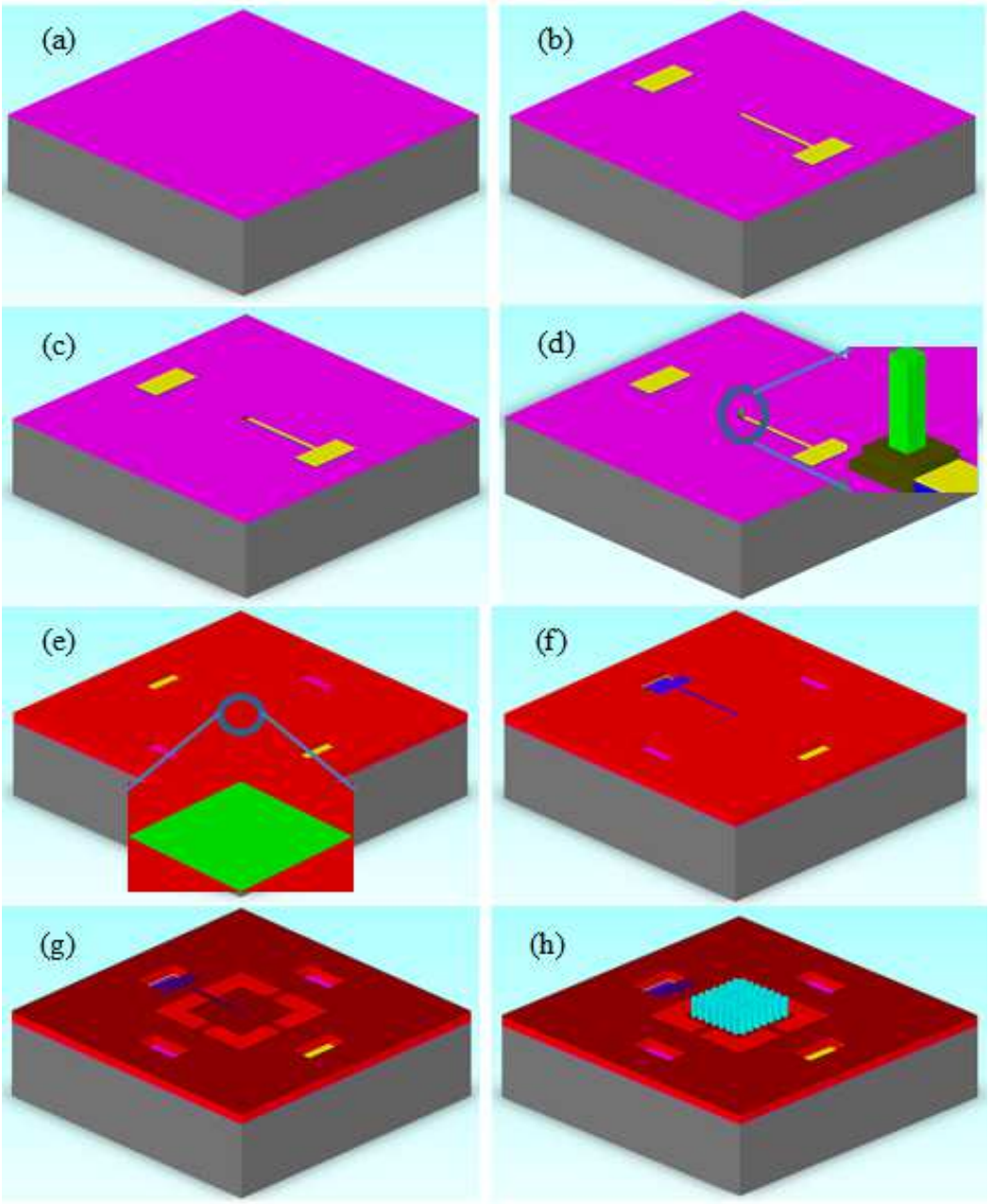

Figure 3-21 Fabrication process flow. (a) Si wafer sputtered with Si_3N_4 isolation layer. (b) Cr/Au bottom electrode. (c) Ti/ZnO seed layer. (d) Single ZnO NW block. (e) Polyimide layer and exposed NW tip by ashing. (f) Ti/Au top electrode. (g) Si_3N_4 membrane. (h) Electroplated Ni layer. Note that *z* scale is exaggerated 10 times.

A 100 nm thick gold layer is evaporated as a seed layer for nickel electroplating which takes place in a nickel sulphamate solution. The negative photoresist NR9-8000P is utilized as the mold layer. Plating time is different in two batches. In one batch, a 20 μm thick nickel proof-mass layer is achieved with current density of 15 mA/cm^2 in the sulphamate solution heated to 45^{o}C for 110 mins of plating [83]. In another batch, a 10 μm thick nickel is electroplated during 80 mins of plating. The exposed gold seed layer is then etched by the argon-plasma anisotropic sputter etching process [84]. Device is released after the sacrificial layer underneath the proof-mass is ashed (Figure 3-21 (h)).

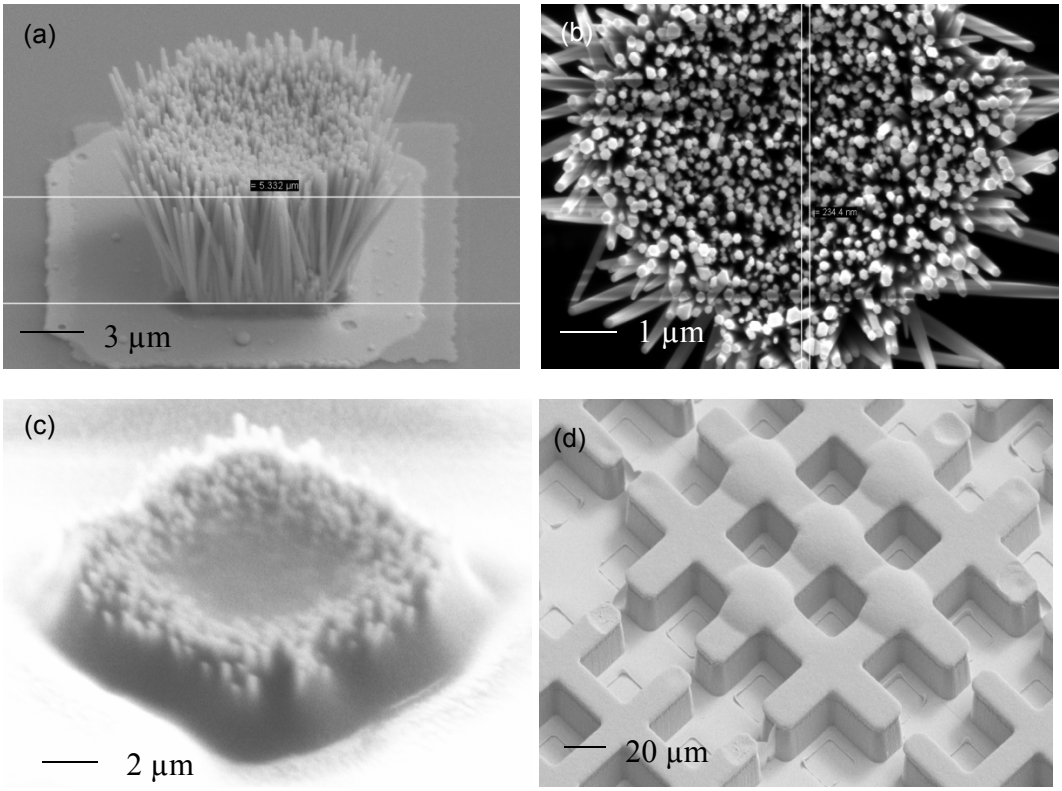

Figure 3-22 Fabrication results for the first batch. (a, b) 8x8 μm ZnO NW block with the height of 7 μm and diameter of 250 nm (tilted by 50^o). (c) NW block embedded in polyimide layer with exposed tip (tilted by 50^o). (d) Electroplated 20 μm thick Ni layer (bumps exist due to the NW blocks underneath, tilted by 50^o).

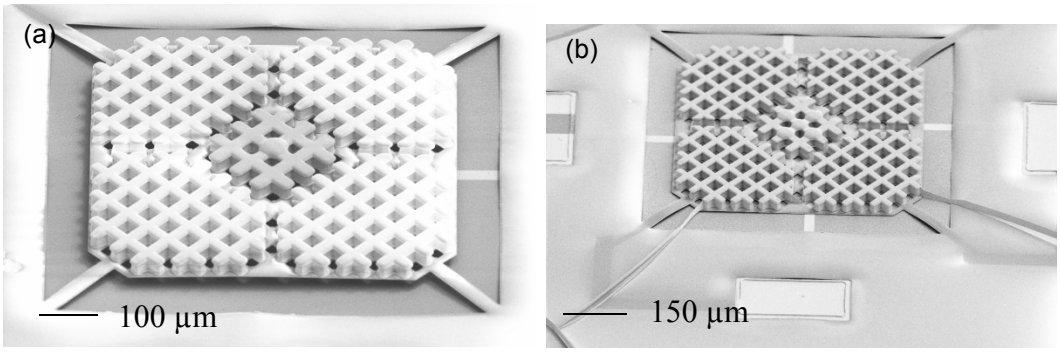

Figure 3-23 Fabrication results for the first batch. (a) NW1-D. (b) Sagging issue.

SEM or microscope images are taken for some important fabrication steps. For the first batch, the resultant size of a single NW block is 8x8 µm. The resultant height of NW is 7 µm and the diameter of NW is about 250 nm (Figure 3-22 (a,b)). 2.7 µm of NW tips are exposed after the polyimide layer has been ashed away (Figure 3-22 (c)). 20 µm thick nickel layer is shown in Figure 3-22 (d). The final device NW1-D is shown in Figure 3-23 (a). Due to heavier proof-mass in this batch, serious sagging is found on larger devices (Figure 3-23 (b)).

For the second batch, the resultant size of a single NW block is again 8x8 µm. The resultant height of NW is 5 µm and the diameter is 150 nm on the average (Figure 3-24 (a,b)). A tiny tip of NW is exposed (Figure 3-24 (c)). The top electrode which covers the NW blocks is in focus in Figure 3-24 (d), while the bottom electrode is out of focus. The top and bottom electrodes are visible through the transparent Si_3N_4 membrane layer (Figure 3-25 (a)). A 10 µm thick electroplated Ni layer on top of the Si_3N_4 membrane layer is shown in Figure 3-25 (b). Due to the internal stress built in the Si_3N_4 layer, some springs are broken after the sacrificial layer has been ashed. This issue is worse for the devices with diagonal-like spring structures. The released device NW4-G, NW1-G and NW4-G-TWO are shown in Figure 3-26 (a,b,c).

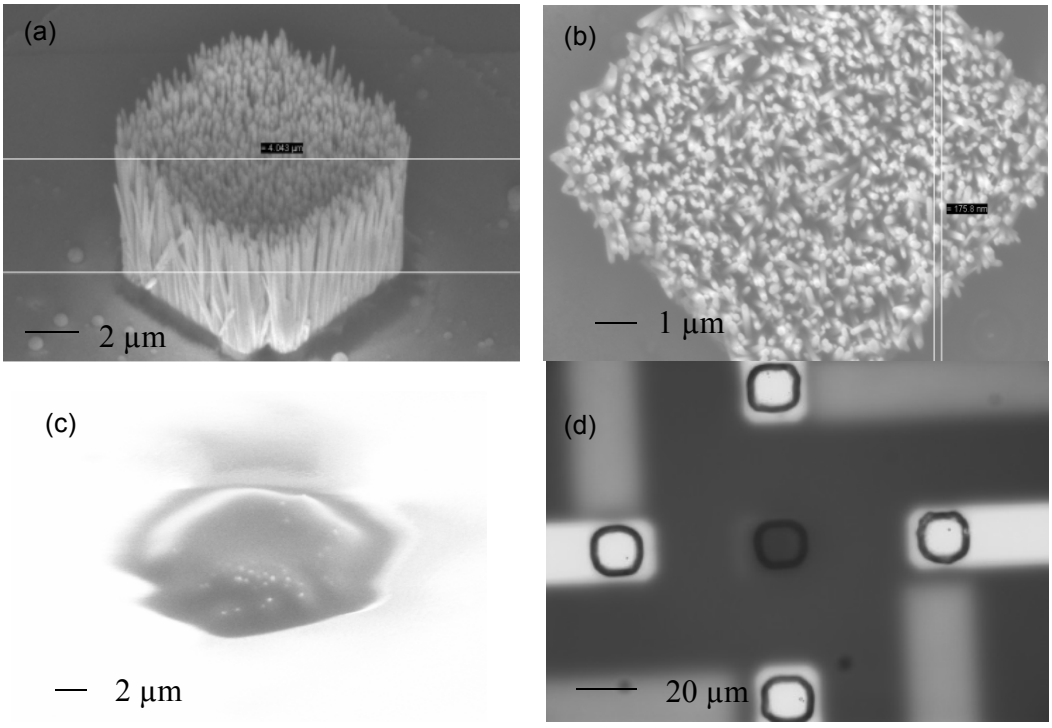

Figure 3-24 Fabrication results for the second batch. (a, b) 8x8 μm ZnO NW block with NW height of 5 μm and diameter of 150 nm (tilted by 50°). (c) NW block embedded in polyimide layer with exposed tip (tilted by 50°). (d) Top electrode layer.

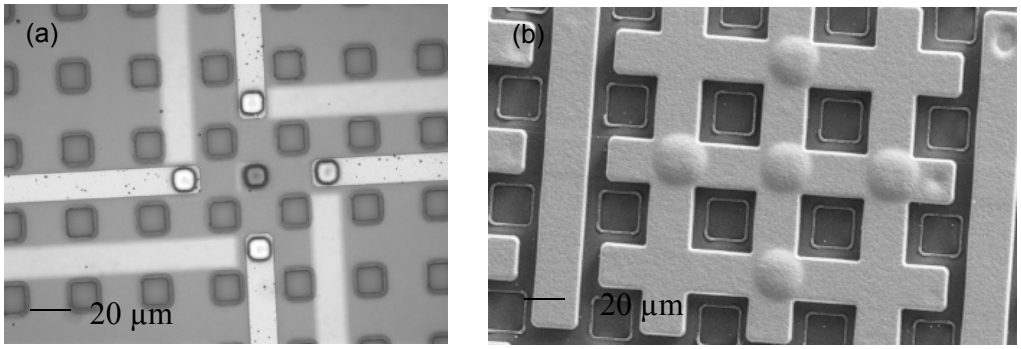

Figure 3-25 Fabrication results for the second batch. (a) Transparent Si_3N_4 layer on top of top electrode layer. (b) Top view of Ni layer, Si_3N_4 membrane layer and NW blocks. (Five bumps exist due to the NW blocks underneath).

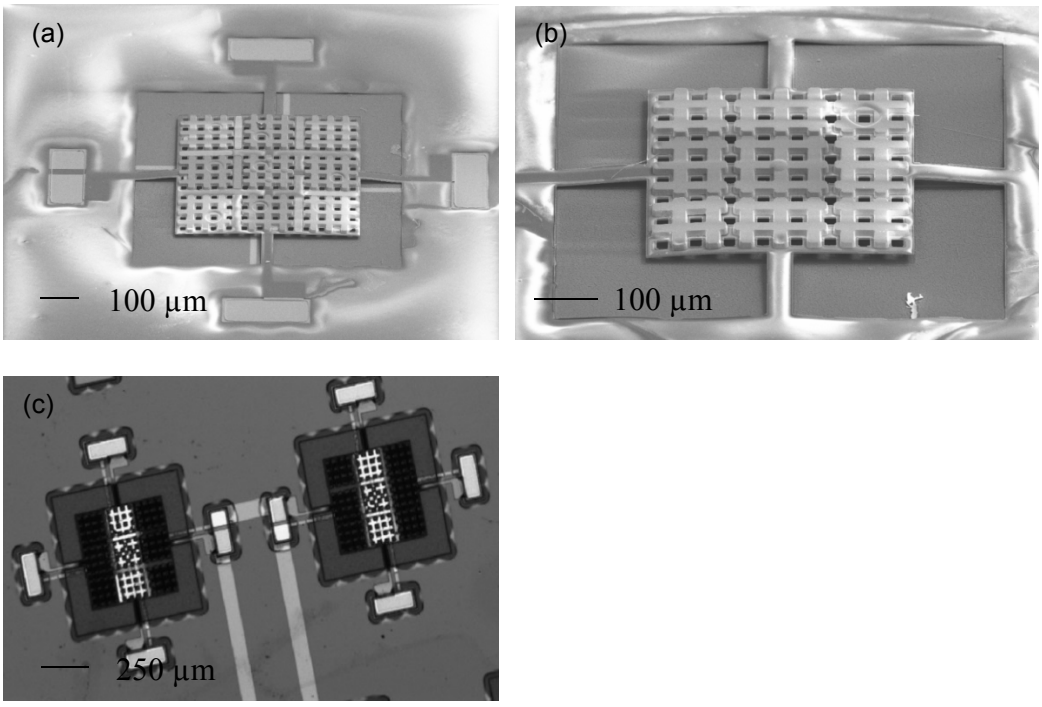

Figure 3-26 Fabrication results for the second batch. (a) Final device NW4-G. (b) Final device NW1-G. (c) Final device NW4-G-TWO.

3.6 Characterization

3.6.1 Characterization Setup

Electrodynamic shaker ED-10 is used as the vibration source. LFG-1300s function generator generates the sinusoidal signal which is furthermore amplified by Crown Dsi amplifier before it is fed into a shaker (Figure 3-27). Along with a commercial reference accelerometer 2260-100, the packaged device is mounted on the shaker [84]. The purpose of the reference accelerometer is to monitor the actual acceleration during vibration. Two kinds of measurements are done: the time domain and the frequency domain. In the time domain measurement, the voltage between the top and bottom electrodes is amplified by SR560 low noise preamplifier before it is connected to the

oscilloscope. On the other hand, in the frequency domain measurement, the output voltage is directly connected to Agilent 35670 signal analyzer. The generated power across the load resistor is calculated based on the measured output voltage.

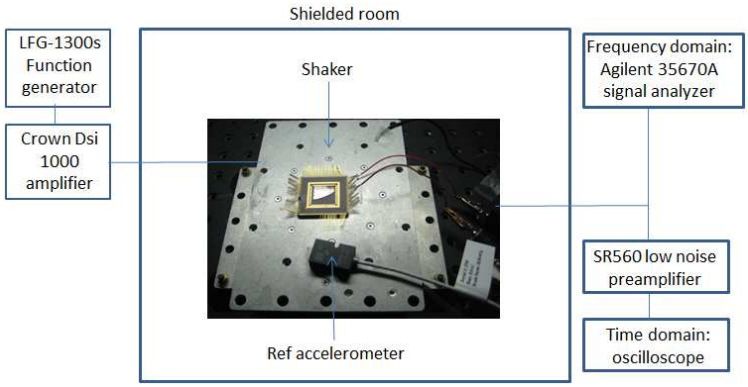

Figure 3-27 Characterization setup for piezoelectric micro energy harvester.

3.6.2 Load Resistor Optimization

Time domain measurements are done across load resistors including 0.5, 1, 2.5, 3, 3.3, 5, 7, 10, 20 and 50 MΩ when the shaker is excited at 40 Hz with an acceleration amplitude of 1.4g. 40 Hz is the resonant frequency of a helicopter or running car [54,55].

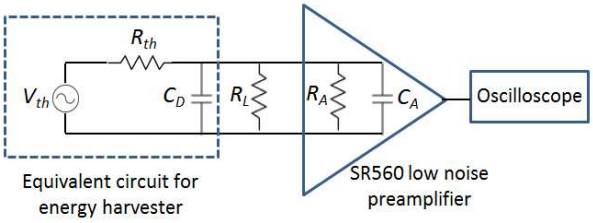

Figure 3-28 Circuit model for load resistor optimization.

A circuit model is built to fit to the experimental results (Figure 3-28). Device is modeled by three electrical components: Thevenin voltage V_{th}, Thevenin resistor R_{th} and device equivalent capacitor C_D which are used as back simulation parameters. R_L is the

load resistor. 100 MΩ R_A and 20 pF C_A represent the input impedance of SR560 low noise amplifier. By introducing the impedances Z_{CD}, Z_{CA} of capacitors C_D, C_A at 40 Hz, the voltage across the load resistor can be deduced as follows:

$$V_{R_L} = V_{th} \frac{Z_{C_D} \| Z_{C_A} \| R_L \| R_A}{Z_{C_D} \| Z_{C_A} \| R_L \| R_A + R_{th}}. \tag{3.8}$$

The generated power can be calculated accordingly as:

$$P_{R_L} = | V_{R_L} |^2 / R_L. \tag{3.9}$$

The experimental and simulation results for device NW1-G, NW4-G, NW4-G-TWO and NW1-D are shown in Figure 3-29. The output voltage increases with the load resistance. However, the maximum power occurs at an optimal load determined by R_{th}. As expected, device NW4-G generates more power than device NW1-G since four NW blocks are connected in series. Moreover, device NW4-G-TWO generates the highest power compared to the others. The generated power from device NW1-D ranks in second place due to the heavy proof-mass. The fitting curves agree with the measurement results very well when the proper fitting parameters V_{th}, R_{th}, C_D are chosen. V_{th} impacts the maximum power value. R_{th} impacts the optimal load resistance. The fitting curve has weak dependence on C_D since characterization is performed at low frequencies. The detailed summary is presented in Table 3-3.

Table 3-3 Experimental and fitting simulation results at 40 Hz with 1.4g acceleration

Device	Optimized load resistance (MΩ)	Magnitude of max output voltage (mV)	Max power (pW)	Fitting curve parameters		
				V_{th} (mV)	R_{th} (MΩ)	C_D (pF)
NW1-G	10	8.05	7.13	17.8	10	20
NW4-G	7	8.33	10.6	19.2	8	20
NW4-G-TWO	7	21.4	70.0	56	10	20
NW1-D	5	13.6	38.7	30	6	20

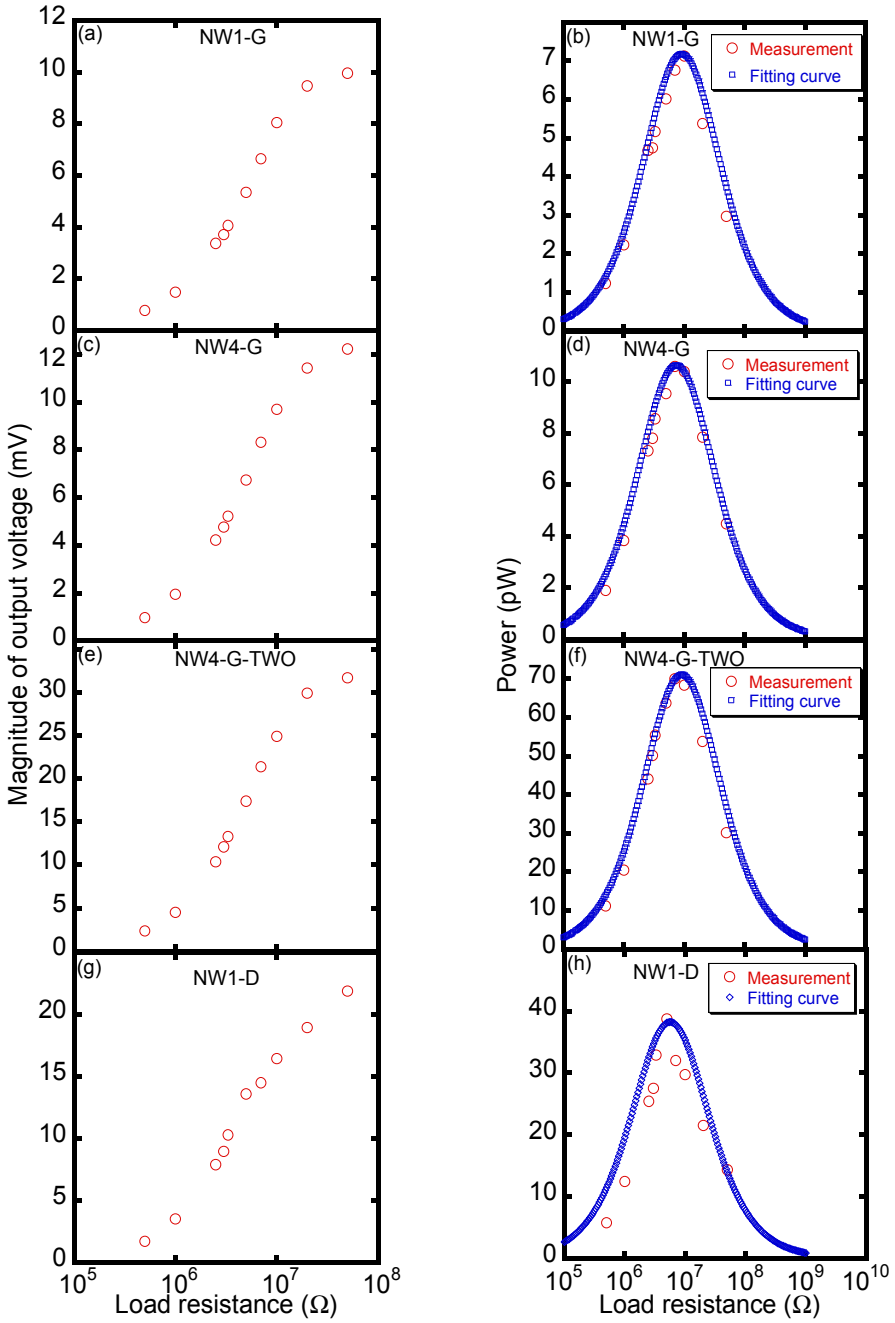

Figure 3-29 The voltage for (a) NW1-G, (c) NW4-G, (e) NW4-G-TWO, and (g) NW1-D. The power for (b) NW1-G, (d) NW4-G, (f) NW4-G-TWO, and (h) NW1-D. (excitation with 1.4g acceleration at 40 Hz)

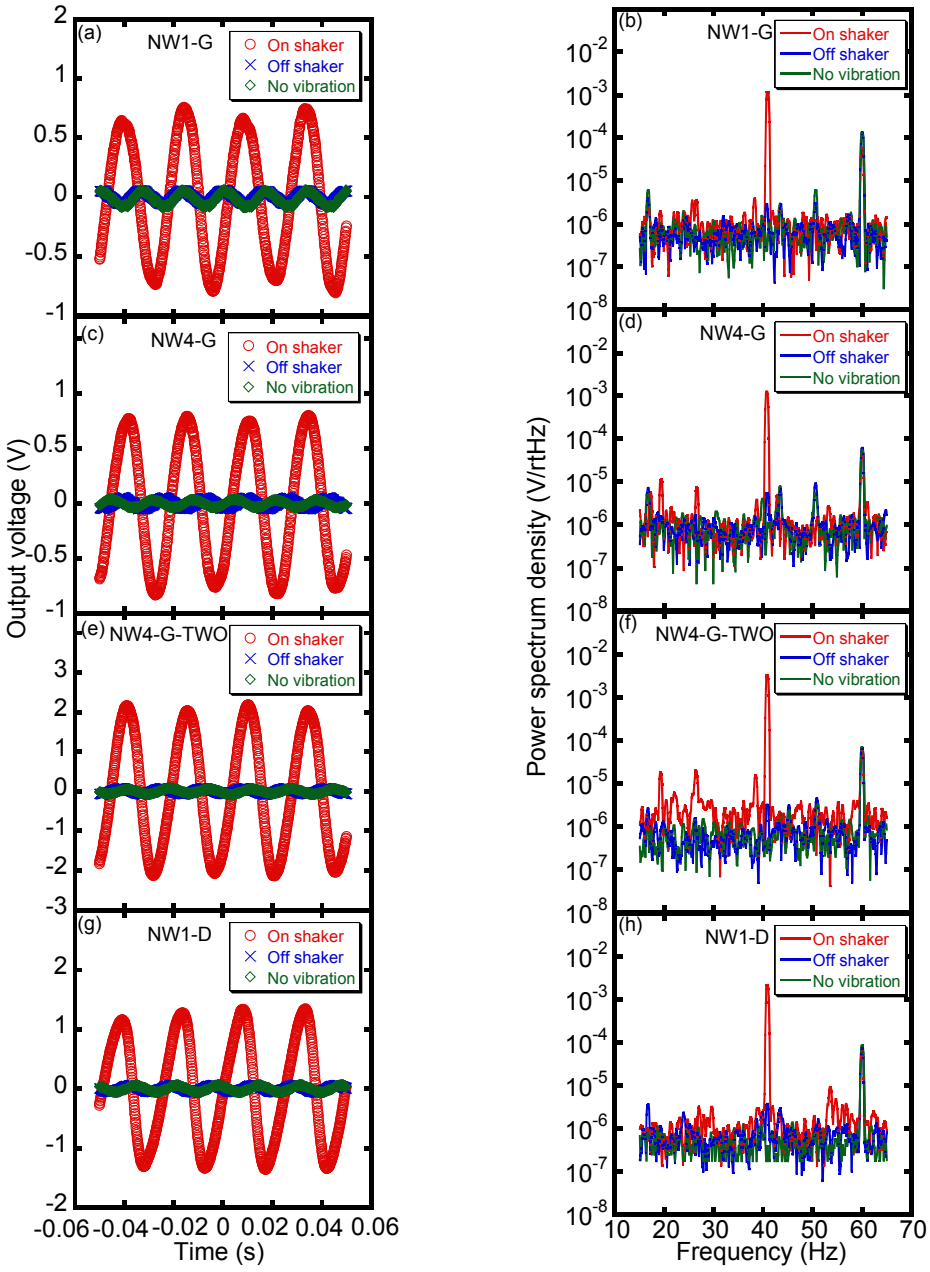

Figure 3-30 The time domain result for (a) NW1-G, (c) NW4-G, (e) NW4-G-TWO, and (g) NW1-D. The frequency domain results for (b) NW1-G, (d) NW4-G, (f) NW4-G-TWO, and (h) NW1-D. (40 Hz vibration with acceleration amplitude value of 1.4g when the optimal load resistor is connected). Note that all time domain signals are amplified by 100.

3.6.3 Noise Analysis

Experimental measurements are taken under three conditions: (1) the device is on the shaker, (2) the device is off the shaker, and (3) there is no vibration. Figure 3-30 shows the time and frequency domain results for devices excited by 40 Hz vibration with acceleration amplitude value of 1.4g when the optimal load resistor is connected. Time domain signal for the case of device on the shaker is clearly stronger than that obtained from the other two cases as would be expected. 60 Hz electromagnetic noise pickup from the environment is the dominant signal when the device is off the shaker or there is no vibration. At the 40 Hz vibration frequency, signal obtained when the device is on the shaker is at least 3 orders of magnitude higher than that detected when the device is off the shaker. If there is no vibration, nothing is detected at the vibration frequency.

3.6.4 Frequency Response

The above analysis is based on the vibration frequency of 40 Hz. We also studied device performance under other frequencies including 49, 101, 203, 1116 Hz with the optimal load resistor connected. Higher acceleration magnitude is detected at higher frequencies. In order to keep the same comparison criteria, the generated power is extracted based on the same acceleration value of 1.4g. Figure 3-31 (a) shows the time domain experimental result for NW4-G at 101 Hz with an acceleration amplitude of 6.5g. Accordingly, the relation between the output voltage and acceleration is plotted in Figure 3-31 (b). The fitting curve equation is given as:

$$output\ voltage = 0.0022 - 0.1756 \times (acceleration). \tag{3.10}$$

According to this equation, the output voltage is -2.44 mV at the 1.4g acceleration. Hence, the generated power is 0.907 pW.

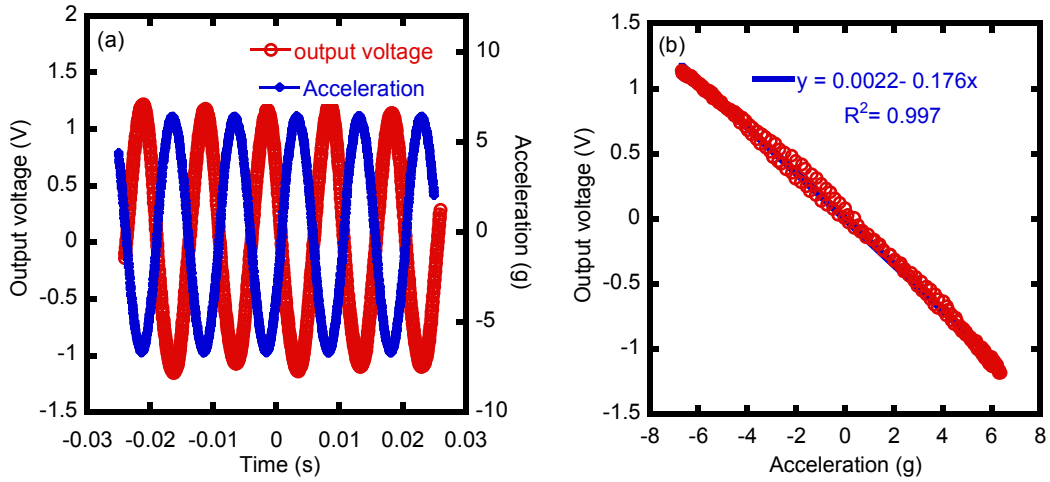

Figure 3-31 (a) The time domain results for the output voltage and acceleration at 101 Hz with an acceleration amplitude of 6.5g (NW4-G). (b) Derived relation between the output voltage and acceleration. Note that output voltage signals are amplified with a gain of 100.

A similar method is used to find out the generated power at other frequencies (Figure 3-32). The generated power decreases when frequency increases. The possible explanation is that at higher frequency, parasitic capacitance effects become more dominant. The output voltage results across the optimal load in the time domain for all tested frequencies are further shown in Figures 3-33, 3-34, 3-35, and 3-36.

Devices presented here have been compared to other state-of-the-art designs including nanogenerators and conventional micro generators (Table 3-4). The mechanical excitation methods for the nanogenerators are different from that for the conventional micro generators. The latter ones are usually excited by a specified acceleration. For nanogenerators, on the other hand, different approaches have been employed based on the design structure to induce the mechanical deformation in the nanostructure such as bending the flexible substrate or exerting pressure. The generated

power calculation varies as well. The power generated from nanogenerators usually equals to the product of open circuit voltage and short circuit current, while for the conventional micro harvester, power is calculated across a load resistor. The power density is normalized by the volume of NW blocks for the design presented in this dissertation. It is competitive among this group of designs.

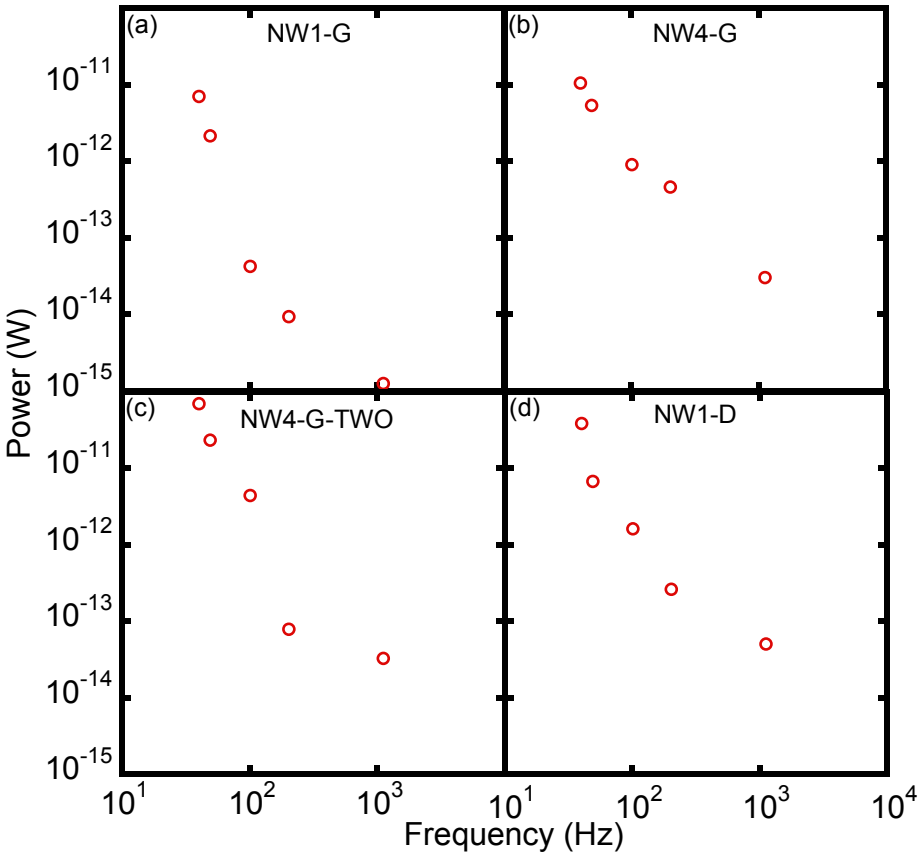

Figure 3-32 The generated power across the optimal load resistor versus frequencies of 40, 49, 101, 203, 1116 Hz under the same acceleration 1.4g. (a) Device NW1-G. (b) Device NW4-G. (c) Device NW4-G-TWO. (c) Device NW1-D.

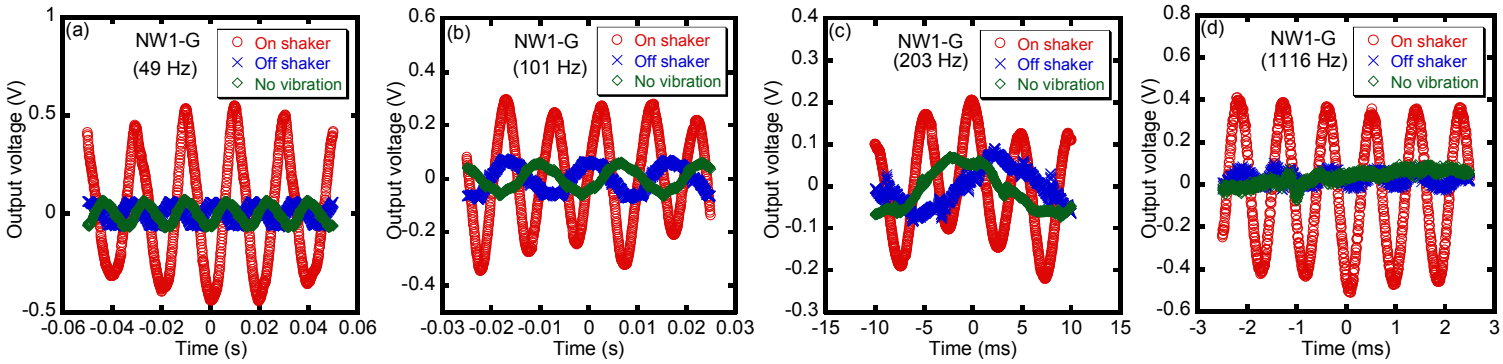

Figure 3-33 Device NW1-G time domain output voltage across the optimal load (10 MΩ) at frequencies (a) 49, (b) 101, (c) 203, and (d) 1116 Hz.

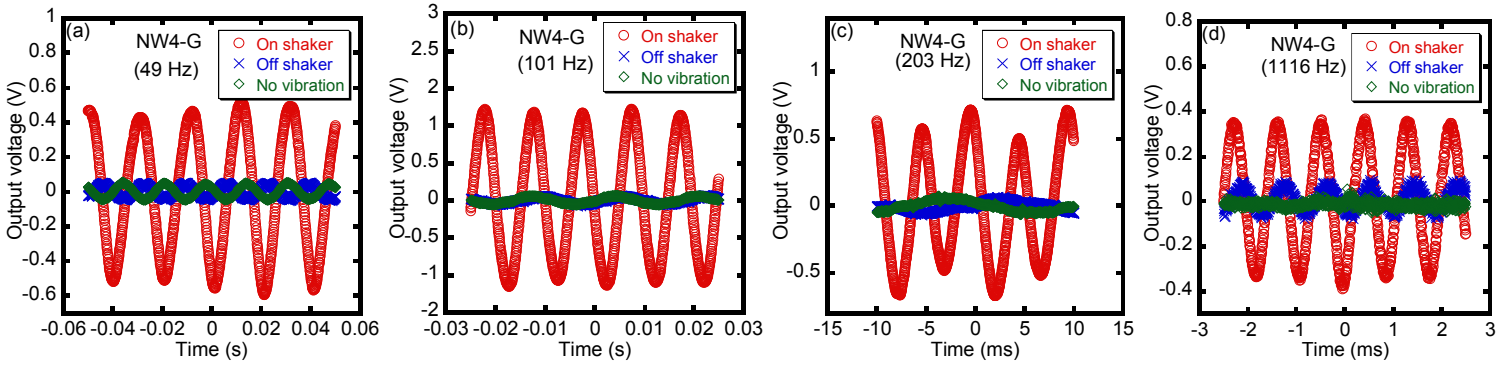

Figure 3-34 Device NW4-G time domain output voltage across the optimal load (7 MΩ) at frequencies (a) 49, (b) 101, (c) 203, and (d) 1116 Hz.

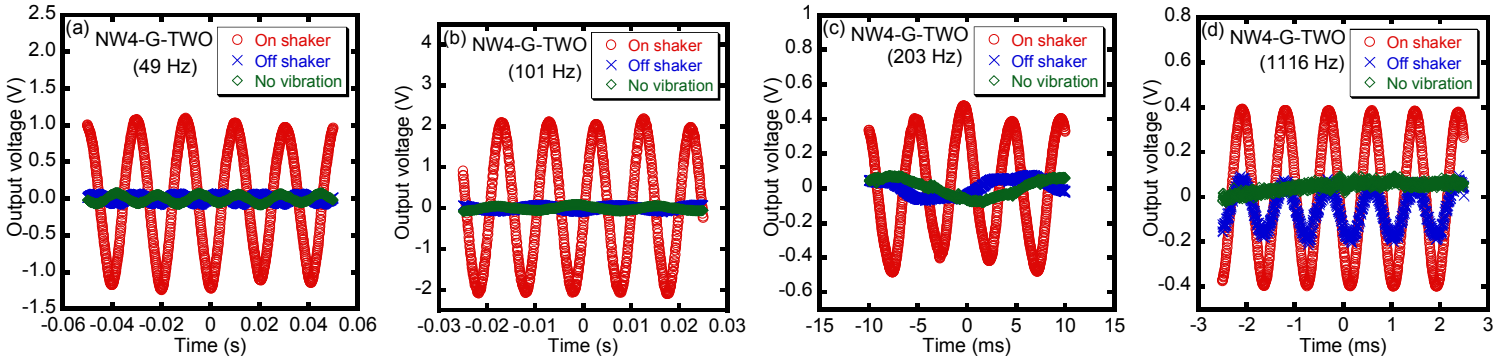

Figure 3-35 NW4-G-TWO time domain output voltage across the optimal load (7 MΩ) at frequencies (a) 49, (b) 101, (c) 203, and (d) 1116 Hz.

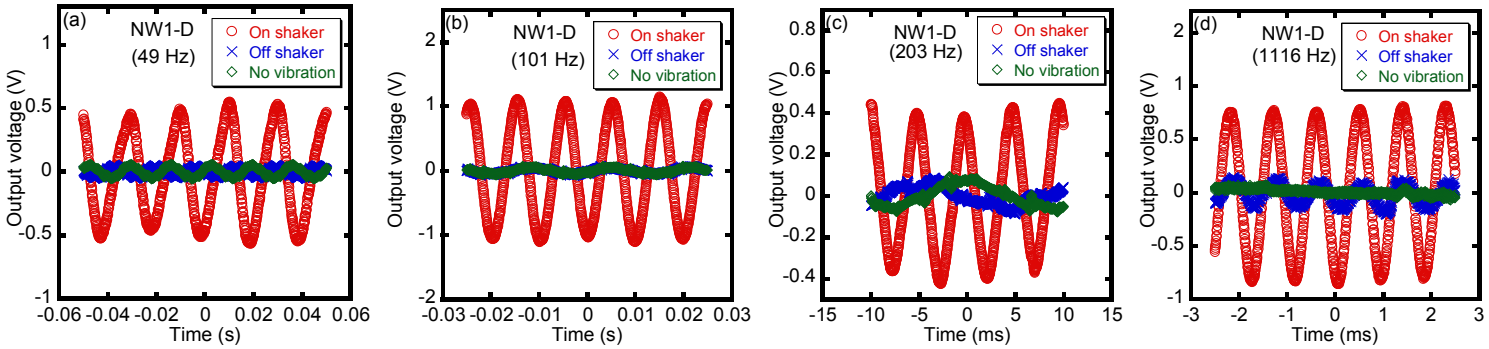

Figure 3-36 NW1-D time domain output voltage across the optimal load (5 MΩ) at frequencies (a) 49, (b) 101, (c) 203, and (d) 1116 Hz.

Table 3-4 Comparison table of state-of-the-art designs.

Material and structure	Dimension	Mechanical excitation	Voltage	Current	Current Density	Power	Power Density
Horizontally aligned ZnO NW on the kapton film [85]	Working area is 1 cm^2, diameter of NW is 200 nm	Strain is 0.1%	2.03 V (open circuit)	107 nA (short circuit)			11 mW/cm^3
Vertically aligned ZnO nanowire/wall between graphene substrate and Au-coated polyethersulfone (PES) [86]		0.5 kgf compressive force on the top surface	20 mV (multimeter)		0.5 $\mu A/cm^2$ (multimeter)		
GaN NW [87]		Scan by a conductive AFM	20 mV				
Single polyvinylidene fluoride (PVDF) nanofiber attached to a plastic substrate [88]		Substrate is bent and released	5–30 mV (multimeter)	0.5–3 nA (multimeter)			
Multiple lateral ZnO NW array integrated nanogenerator (LING) on flexible substrate [23]	NW is 5 μm high and the diameter is ~x100 nm, total size 1x3 cm^2	Strain of 0.19%, strain rate of 2.13 %/s	1.26 V (open circuit)	28.8 nA (short circuit)			70 nW/ cm^2
Vertical ZnO NW array integrated nanogenerator (VING) between two silicon wafers [23]	NW with a tip diameter of 300 nm and length of 4 μm, size of VING is 4 mm^2	Pressure on the top surface	0.243 V for 3 VINGs in series (open circuit)		18 nA/cm^2 for 3 VINGs in parallel (short circuit)		2.7 mW/cm^3
Nanogenerator (NG) made of vertical NW. Bending by upper wafer coated with nanotip (NTP) arrays [24]	Surface area for each NG is 6 mm^2	Ultrasonic wave of 41 kHz	62 mV for 4 NGs in series (open circuit)	105 nA for 4 NGs in series (short circuit)			0.11 $\mu W/cm^2$

Table 3-4 – continued

Piezoelectric PZT cantilever [89]	Beam size: 3.31e-3 cm^3[3a]	8g acceleration, 870 Hz				1.13 µW on 288.5 kΩ load	301 $\mu W/cm^3$
Multilayer unimorph PZT cantilever with Si proof-mass based on SOI [90]	Proof-mass plus beam: 0.7690mm^3	0.75 g acceleration, 183.8 Hz	101 mV (magnitude)			0.32 µW on16 kΩ load	416 $\mu W/cm^3$
Piezoelectric PZT cantilever [91]	Cantilever: 800×100x10 μm^3, proof-mass: 1000 × 1000× 500 μm^3	0.39 g acceleration, 528 Hz	4.4 V (peak to peak)			1.1 µW on 2.2 MΩ load	1.09 mW/cm^3
NW1-G (This work)	3.20 x 10^2 μm^3	1.4 g acceleration, 40 Hz	8.05 mV on load			7.13 pW on10 MΩ load	22.3 mW/cm^3
NW4-G (This work)	1.60 x 10^3 μm^3	1.4 g acceleration, 40 Hz	8.33 mV on load			10.6 pW on 7 MΩ load	6.63 mW/cm^3
NW4-G-TWO (This work)	3.20 x 10^3 μm^3	1.4 g acceleration, 40 Hz	21.4 mV on load			70 pW on 7 MΩ load	21.9 mW/cm^3
NW1-D (This work)	4.48 x 10^2 μm^3	1.4 g acceleration, 40 Hz	13.6 mV on load			38.7 pW on 5 MΩ load	86.4 mW/cm^3

[a] Calculated from the given information in the referenced paper.

3.7 Summary

A Piezoelectric micro energy harvester utilizing the piezoelectricity of the vertically aligned ZnO nanowires has been fabricated by MEMS surface micromachining technology in conjunction with the low temperature hydrothermal growth of nanowires. Several designs have been implemented with varying proof-mass, spring structures and nanowire sizes. Characterization results are described for devices NW1-G, NW4-G, NW4-G-TWO and NW1-D. When the shaker is excited at 40 Hz with an acceleration value of 1.4g, device NW4-G-TWO generates the highest power of 70 pW across the optimal 7 MΩ load resistor. Even though device NW4-G has 4 NW blocks in series, this advantage is compromised by the increase of the mechanical stiffness. Therefore, in order to achieve an even higher power, series connection of several devices is the solution. When the harvester is on the shaker, the output voltage in time domain is much stronger than that detected when device is off the shaker. Frequency domain result indicates that signal to noise ratio is about 1000:1. Frequency response of the harvesters is characterized when the acceleration is kept at a constant value of 1.4g. Devices generate higher power at lower frequency most likely because at lower frequency the effect of parasitic capacitors has been suppressed. Compared to the simulation result, the measured output voltage is generally higher. One reason for smaller simulation values could be ZnO nanowires are modeled as a solid block which is stiffer than a group of nanowires. Thus, smaller mechanical displacement results in lower output voltage in simulations.

Chapter 4

Conclusion

A wireless sensor node generally has a power generator, sensing, computing and communications subsystems. The sensing subsystem consumes 6-20% of the total power. Different types of sensors such as light, temperature, pressure, vibration or humidity require certain amount of power to keep their normal operations. Energy harvesters are generally more favorable than batteries due to their limited lifetime. Efforts have been made to realize the integration of the effective energy harvesters into the wireless sensor nodes in the past years [92].

Vibrational energy harvesters can be best utilized when the vibrations are stable and constant. According to the analysis for the generic vibration-to-electricity conversion model, the generated power is maximized when it is designed to resonate with the input vibration frequency. The power is inversely proportional to the frequency with the defined acceleration [6]. Moreover, the power is proportional to the square of acceleration magnitude and mass of the proof-mass. The three types of vibrational energy harvesters are: electromagnetic, electrostatic, and piezoelectric generators.

Inductive electromagnetic generators utilize the principle of electromagnetics: electromotive force will be induced in a closed circuit due to the change of the magnetic flux. Additional voltage source is not required for this type of converter, while the strong magnetic field from the magnet might impact the normal operations of other electrical components.

Electrostatic energy harvester employs the MEMS variable capacitor structure. The mechanical vibration drives the change of overlap area or gap distance between the capacitors. A voltage source is used to polarize the capacitor at the beginning. The voltage increases due to the decrease of capacitance when the charge is constrained.

Furthermore, the newly gained voltage will be stored to the storage capacitor. Another option is to explore the possibility of an embedded electret which can permanently store the injected the charges, whereas, it requires high voltage electron charging equipment. As for the different topologies of MEMS capacitors, the comb drive structures form either in-plane gap closing or in-plane overlap capacitors. The out-of-plane topology can be constructed by two parallel plates. The first two designs are easy to be integrated with the mechanical stoppers which are helpful in preventing the pull-in effect.

A novel electrostatic energy harvester design is presented with the in-plane gap closing and overlap comb fingers incorporated into one structure to enlarge the output power. A bias capacitor and voltage are used to provide the initial charges. Electromechanical coupling model is built to optimize the design parameters. Some design parameters are predefined due to the fabrication limitation. Four design structures are finalized according to the optimal values obtained from simulations. MEMS surface micromachining technology is used to fabricate the devices. A thick layer of nickel is electroplated as the proof-mass. The electroplated nickel bows up after the sacrificial layer underneath is ashed away since the internal stress is built up during plating. This issue is worse for the larger devices. The smallest device is characterized on a shaker excited by a signal generator. Across a 5 MΩ load resistor, 0.8 V peak to peak value is detected under 1.9 kHz with the acceleration magnitude of 8g (1 μF bias capacitor is pre-charged by a 6 V dc source). Signal to noise ratio has been proven to be 100:1 by comparing the voltages obtained when device is on the shaker and device is off the shaker. The corresponding power is 0.29 μW and the power density is 20.7 mW/cm^3. This power density value ranks in third place among seven other state-of-the-art designs. The more practical improvement should be done to replace the bias capacitor and voltage with an incorporated pre-charged electret.

Piezoelectric energy harvesters use the piezoelectric effect of materials and can be ceramics, semiconductors or polymers. Formation of an electric dipole moment in the solid is the reason for the piezoelectricity. Cantilever structures have been commonly used for conventional piezoelectric micro energy harvesters which can be fabricated on the SOI wafers or by MEMS bulk micromachining process. d_{33} mode (the electric field direction is parallel to the mechanical stress/strain direction) is more attractive than the d_{31} mode (the electric field direction is perpendicular to the mechanical stress/strain direction) since d_{33} is usually higher than d_{31}.

Recently, the idea of the piezoelectric nanogenerator has been presented. Such kind of generator uses the nanostructure of semiconductor materials such as ZnO or GaN. ZnO as a direct band gap semiconductor has many optoelectronic applications including laser diodes and light emitting diodes. It can be employed in the field emitter, the front contact of solar cells, or the hydrogen gas sensors as well. The nanogenerator utilizing ZnO nanostructure has been first demonstrated by Z. L. Wang *et al*. ZnO crystal has hexagonal wurtzite structure with Zn as cation and O as anion. Electric dipole is formed between the positive charged zinc planes and negative charged oxygen planes. The mechanical strain in a bent or compressed nanowire induces the electrical potential due to the direct piezoelectric effect. For a single nanowire bent by a certain force on the top surface, the electrical potential distribution on the cross section surface has been analytically modeled. The maximum positive potential is located at the tensile surface, while, the negative potential is located at the compressive surface with the maximum absolute value. The electrical potential is proportional to the bending force. A nanowire with large aspect ratio tends to have a high electrical potential. For a single nanowire compressed on the top surface with the bottom surface fixed and grounded, the highest negative electrical potential is located on the top surface. Such an electrical potential is

proportional to the displacement on the top surface, regardless of the size of the nanowire. According to the simulation results, the mechanical compression is more favorable than bending since a larger electrical potential is generated from the compression with the same amount of deflection. Different kinds of design structures have been developed to induce the mechanical deformation of nanowires. For example, nanowires laterally attached to the flexible substrate will be stretched when the substrate is bent, while vertically standing nanowires between two silicon wafers will be compressed when the pressure is exerted on the top wafer.

Compared to the conventional piezoelectric energy harvesters, nanogenerators employ semiconductor materials which are friendly to the environment and compatible with the biomedical applications. Piezoelectric ceramic materials have better piezoelectricity. However, this advantage has been compromised since the fabrication requires high temperature processes.

In this dissertation, the vertically standing nanowires are compressed by a Si_3N_4 membrane and a Ni proof-mass which are excited by the external vibration. There are different growth methods for the ZnO nanostructure. The low temperature chemical growth on a seed layer is chosen here. The selective growth of an 8x8 μm nanowires block is realized by the hydrothermal growth method in conjunction with the SU-8 photoresist template. SU-8 can survive in the heated nutrient solution for several hours and can be removed after growth. Several designs are presented with different spring structures. Devices are designed to have either a single NW block or several NW blocks connected in series. Some devices have severe sagging issues due to the heavier proof-mass. Device NW4-G-TWO shows the highest power of 70 pW on the optimal 7 MΩ load resistor when it is excited at 40 Hz with acceleration value of 1.4g. The corresponding output voltage is 21.4 mV across the load resistor. The authenticity of the signal has been

verified by eliminating any possibility of feedthrough from the shaker circuitry. Signal to noise ratio is 1000:1. The energy harvester generates higher power at lower frequency under the same acceleration of 1.4g.

These are breakthrough but preliminary results. More effort is needed to improve the output power of the energy harvesters in order to meet the requirements of the wireless sensor nodes. On one hand, this involves the materials with superior piezoelectric properties or progress in the design structures. On the other hand, an effective power management system is desired for the wireless sensor nodes which can manage the power usage more efficiently by storing the scavenged power into a storage element when the node is in inactive state. Hence, the total amount of required power can be reduced.

Appendix A

Electrostatic Energy Harvester Simulation Settings

A.1 Mechanical Simulation

Here the simulation results for device F1500K10 are presented. The meshed model for the nickel layer is shown in Figure A-1. The mesh type is chosen as the extruded brick with split and merge algorithm. The element order is parabolic. The element size in the planar directions is 25 μm. The element size in the extrude direction is 2.5 μm.

Regarding the solver settings, two boundary conditions are defined: surfaceBCs and volumeBCs. The highlighted anchoring surfaces in Figure A-2 are fixed in the surfaceBCs. In the volumeBCs, all parts are exerted by 20g acceleration in positive *X* direction and 1g in the negative *Z* direction to represent gravity (Figure A-3,4).

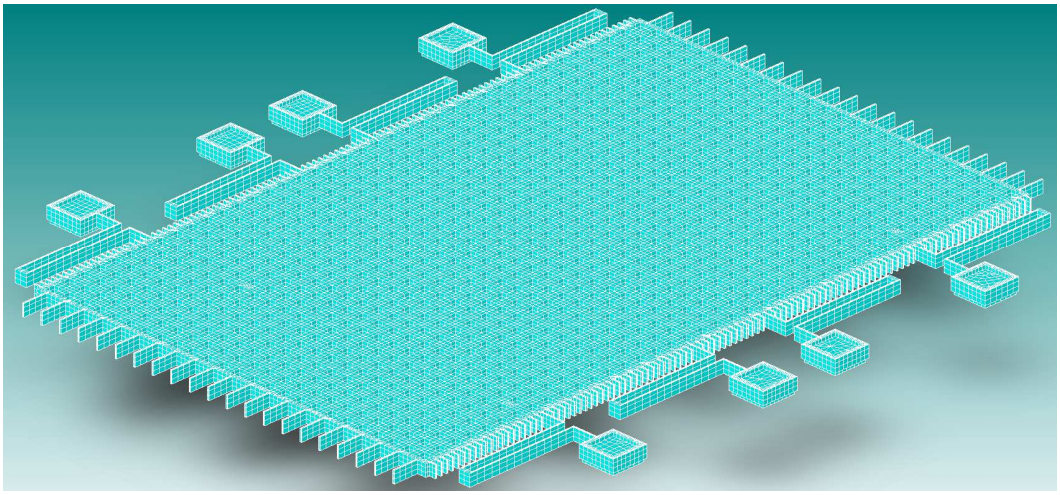

Figure A-1 The meshed model of device F1500K10 for mechanical simulaiton.

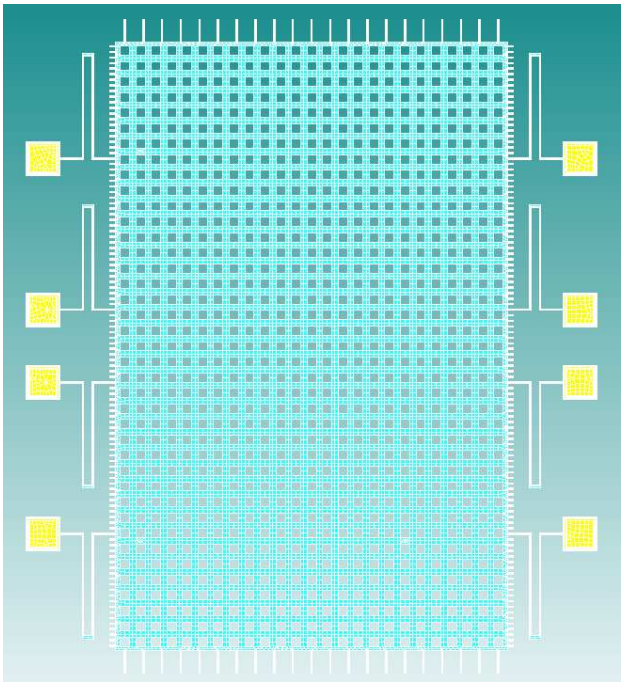

Figure A-2 The anchoring surfaces are fixed in the surfaceBCs.

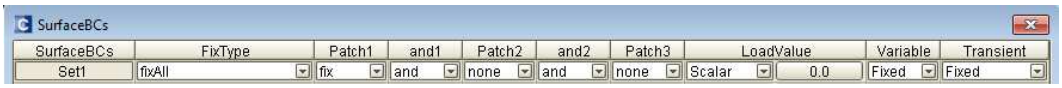

Figure A-3 SurfaceBCs settings for mechanical simulation.

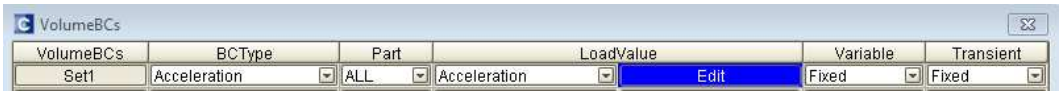

Figure A-4 VolumeBCs settings for mechanical simulation.

A.2 Modal Harmonic Simulation

The same meshed model is used for this type of simulation. The solver settings are shown in Figure A-5. The same surfaceBCs are defined for the boundary conditions. In the volumeBCs setting, only 1g acceleration is exerted in the negative *Z* direction. In the harmonic_volumeBCs, 1g acceleration is exerted in the positive *X* direction (Figure A-6).

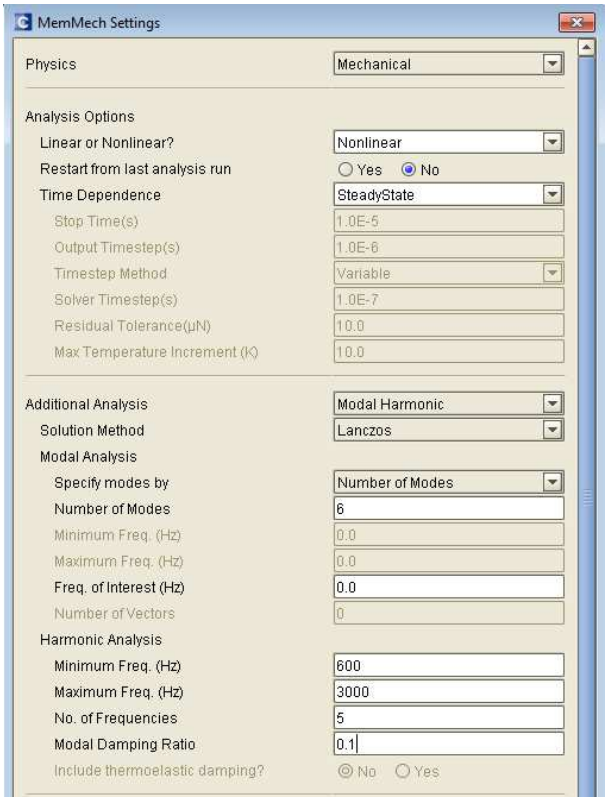

Figure A-5 Solver settings for modal harmonic simulation.

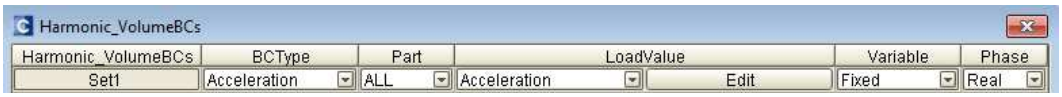

Figure A-6 Boundary condition settings for modal harmonic simulation.

A.3 Capacitance Simulation

The meshed model is shown in Figure A-7. Three layers are added into the meshed model: nickel layer, aluminum interconnection layer and pad layer. The mesh type is chosen as the extruded brick with split and merge algorithm. The element order is parabolic. The element size in the planar directions is 50 μm. The element size in the extrude direction is 2 μm. In the boundary condition setting, 6 V is added to the proof-mass pad (conductor 2), while other two pads are grounded (Figure A-8).

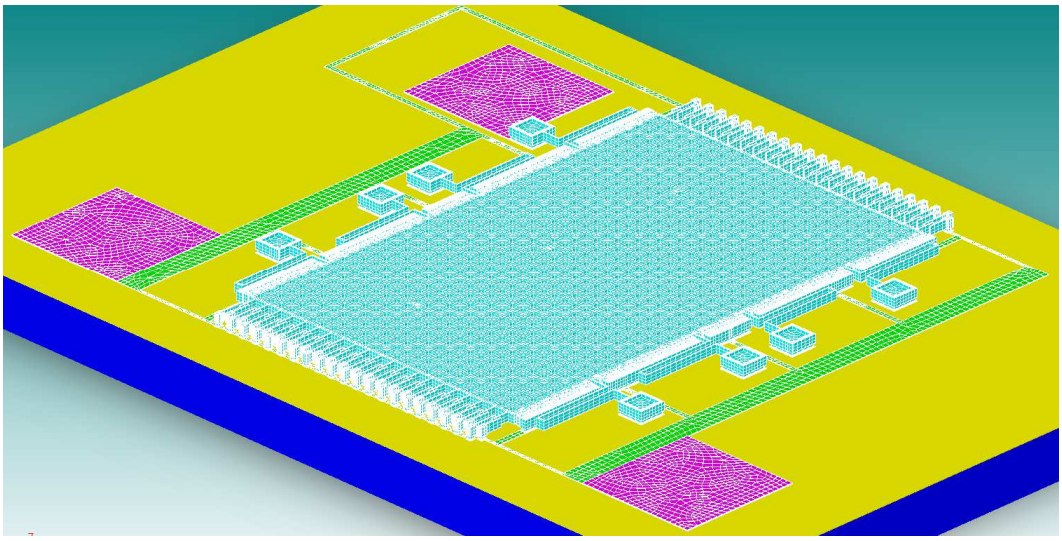

Figure A-7 The meshed model of device F1500K10 for capacitance simulation.

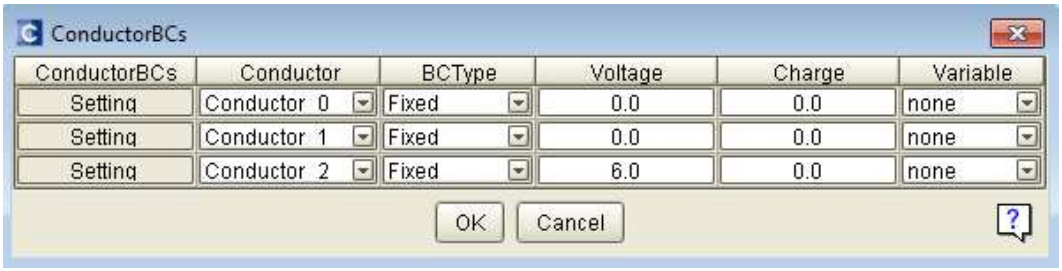

Figure A-8 ConductorBCs setting for capacitance simulation.

A.4 Summary

Three types of simulation setting have been presented: mechanical simulation for device under certain acceleration, modal harmonic simulation and capacitance simulation.

Appendix B

Piezoelectric Energy Harvester Simulation Settings

B.1 Mechanical Simulation

Here the simulation results for device NW1-G are presented. The meshed model for the nickel layer, Si_3N_4 layer, top electrode layer and nanowire layer are shown in Figure B-1. The mesh type is chosen as the extruded brick with split and merge algorithm. The element order is parabolic. Si_3N_4 layer has been partitioned into two parts with different mesh size. Si_3N_4 part 1 is free to vibrate due to the undercutting of the sacrificial layer, while Si_3N_4 part 2 is anchored to substrate through the sacrificial layer. Table B-1 lists the mesh size for different layers. The element size in the planar directions is 25 μm. The element size in the extrude direction is 2.5 μm.

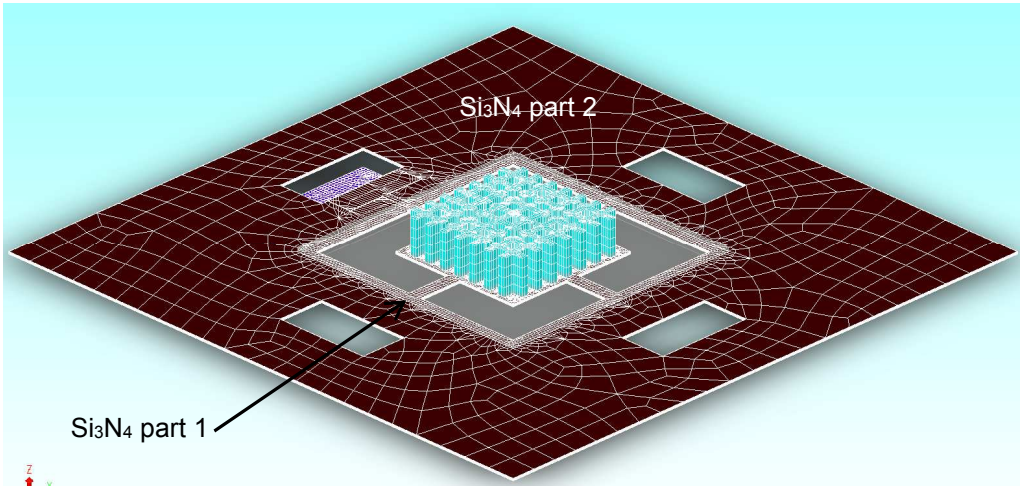

Figure B-1 meshed model for device NW1-G

Table B-1 element size for different layers

	element size in the planar direction (μm)	element size in the extrude direction (μm)
Nickel	100	5
Si_3N_4 part 1	10	0.05
Si_3N_4 part 2	100	0.5
Top electrode	10	0.05
Nanowire	5	1

Two boundary conditions are defined for the solver settings: surfaceBCs and volumeBCs. The highlighted surfaces are the bottom surface of nanowire, the anchoring surface of top electrode and the bottom surface of Si_3N_4 part 2 (Figure B-2). All these surfaces are fixed in the surfaceBCs (Figure B-3). In the volumeBCs, all parts are exerted by 1.4g acceleration in the negative *Z* direction to represent gravity (Figure B-4).

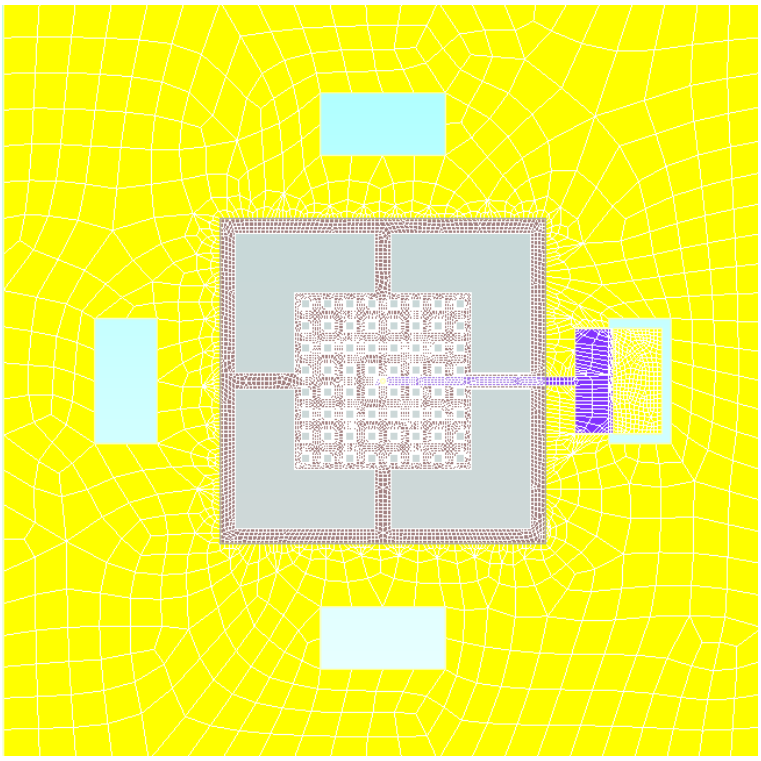

Figure B-2 Fixed surfaces

SurfaceBCs

SurfaceBCs	FixType	Patch1	and1	Patch2	and2	Patch3	LoadValue		Variable	Transient
Set1	fixAll	fix	and	none	and	none	Scalar	0.0	Fixed	Fixed
Set2	fixAll	fix2	and	none	and	none	Scalar	0.0	Fixed	Fixed
Set3	fixAll	fix3	and	none	and	none	Scalar	0.0	Fixed	Fixed

Figure B-3 SurfaceBCs setting

VolumeBCs

VolumeBCs	BCType	Part	LoadValue		Variable	Transient
Set1	Acceleration	ALL	Acceleration	Edit	Fixed	Fixed

Figure B-4 VolumeBCs setting

B.2 Ansys Simulation Settings

In the preprocessor, several properties are defined. In the modeling, a solid cylinder with the radius of 75 nm, depth of 5 μm has been created. The bottom surface is centered at (0, 0). The mesh shape is chosen as “mapped hex” in the “mesh tool”. The element type is chosen as solid226 (Figure B-5). The analysis type is chosen as “electroelast/piezoelectric” (Figure B-6). In the “material props” option, material models are defined. (Figure B-7)

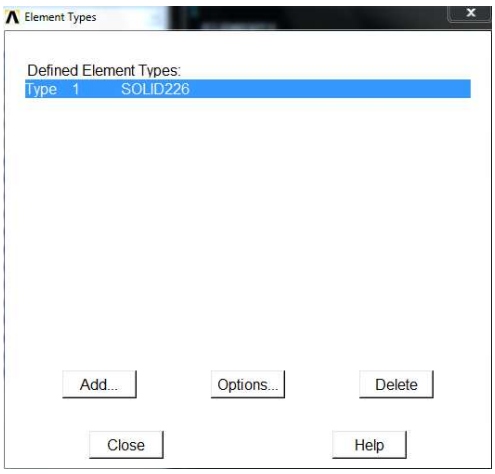

Figure B-5 Element type

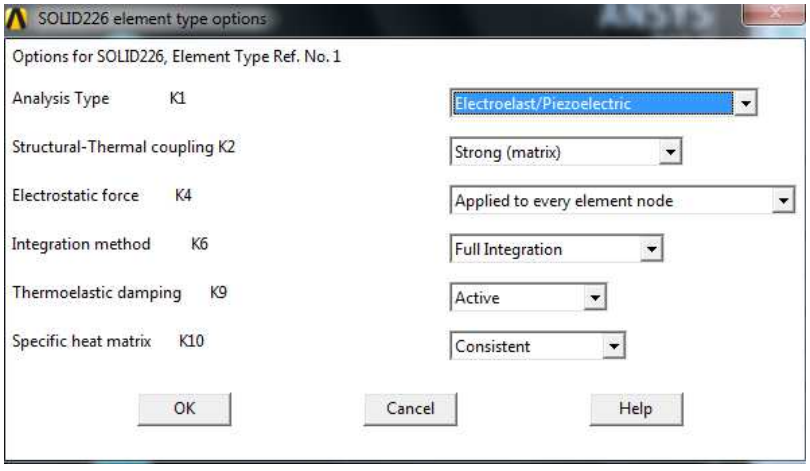

Figure B-6 Analysis type

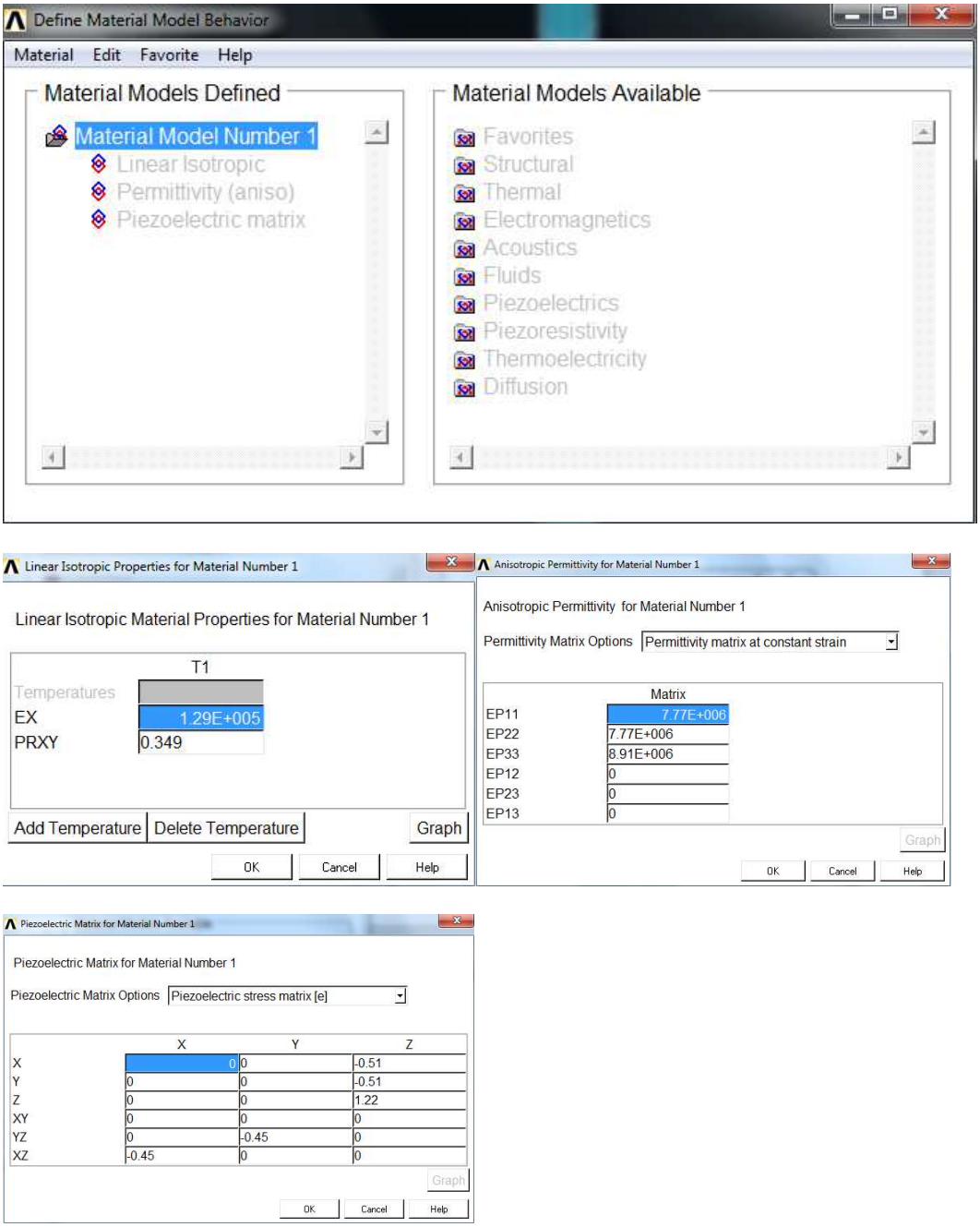

Figure B-7 Material models for ZnO.

In the solution, loads have been added to the meshed model. In the “structure” option, certain amount of displacement in the negative z direction has been added to the top surface of nanowire. All DOFs have been defined as 0 for the bottom surface. In the “electric” option, voltage has been defined as 0 for the bottom surface. Figure B-8 shows the main menu.

Figure B-8 Main menu

B.3 Summary

Two types of simulations have been done for the piezoelectric energy harvester: mechanical simulation for the whole device and single nanowire electrical potential distribution due to compression. Here the detailed simulation settings have been presented.

Appendix C

Power Optimization Code in MATLAB

MATLAB function ode15s is used to solve the differential equations. The main codes are shown below:

```
global W_pm % width of proof-mass
global L_pm % length of proof-mass
global t_pm % thickness of proof-mass
global m % mass of proof-mass
global V_bias % bias voltage source
global C_bias % bias capacitor
global A % magnitude of acceleration
global r1 % t_pm/gap of overlap fingers
global r2 % t_pm/width of fingers
global q_0 % initial charges shared between the C_bias and variable capacitors
global q_1 % charges on one variable capacitor
global q_2 % charges on another variable capacitor
global tstartind % index for the start cycle
global tstartcy% start cycle
global tendcy % end cycle
global R % load resistor
global N_ol % number of overlap fingers on one side of proof-mass
global ε_0 % vacuum permittivity
global h_ol % initial overlap of overlap fingers
global N_gc % number of gap-closing fingers on one side of proof-mass
global h_gc % initial overlap of gap-closing fingers
global g_gc % gap of gap-closing fingers
global visc % viscosity of air
```

```
global tPI % distance between the proof-mass and substrate
global ρ % density of nickel layer
global kl % lateral spring constant
global ω % input vibration frequency
% invoke function rigid to solve t and y (q1,q2,x,x')
options = odeset('RelTol',1e-6);
[t, y] = ode15s(@rigid,[0 tendcy*2*3.14/w],[q0 q0 0 0],options);
 % find the currents across the load resistors
for i=1:(size(y,1))
 % dq1/dt = k (i,1)
k(i, 1)= - y(i,1)/R/(2*Nol*(ε0)*r1*((hol)-y(i,3))+ 2*Ngc* ε0*tpm*hgc/(ggc+y(i,3)))
(y(i,1)+y(i,2))/(Cbias)/R+ Vbias/R;
% dq2/dt =k(i,2)
k(i, 2)= - y(i,2)/R/(2*Nol*( ε0)*r1*(( hol)+y(i,3))+ 2*Ngc* ε0* tpm *hgc/(ggc-y(i,3)))-
(y(i,1)+y(i,2))/(Cbias)/R+ Vbias/R;
% Pout(t)
k(i, 3)= (R) * ( k(i, 1)*k(i, 1)+ k(i, 2)*k(i, 2));
end
% find the index of t matrix at the start cycle
for i = 1:length(t)
            if (t(i)< (tstartcy*2*3.14/w))|(t(i)== (tstartcy*2*3.14/w))
                tstartind= i;
             end
end
% calculate the average power between start cycle and end cycle
```

```
P=0;
for i=(tstartind):(size(y)-1)
        u = k(i, 3)* ( t(i+1)-t(i));
        P = P + u;
end
Pout = P/(max(t)-t(tstartind));
% The invoked function rigid will solve for t and y (q1,q2,x,x').
function dy = rigid(t,y)
% y (q1,q2,x,x')
dy = zeros(4,1);   % q1'(0), q2'(0), x'(0), x''(0) =0
% dq1=dy(1)
dy(1) = - y(1)/R/(2*Nol*(ε0)*r1*((hol)-y(3))+ 2*Ngc*ε0*tpm*hgc/(ggc+y(3)))-
(y(1)+y(2))/(Cbias)/R+ Vbias/R;
% dq2=dy(2)
dy(2) = - y(2)/R/(2*Nol*(ε0)*r1*((hol)+y(3))+ 2*Ngc*ε0*tpm*hgc/(ggc-y(3)))-
(y(1)+y(2))/(Cbias)/R+ Vbias/R;
% dx=y(4)
dy(3) = y(4);
% dx''=dy(4)
dy(4) = (y(2))^2*(2*Nol*ε0*r1+ 2*Ngc*ε0* tpm*hgc/(ggc-y(3))/(ggc-
y(3)))/((2*Nol*(ε0)*r1*((hol)+y(3))+ 2*Ngc*ε0*tpm*hgc/(ggc-y(3))))^2/2/m -(y(1))^2*(2*Nol*ε0*r1+
2*Ngc*ε0* tpm*hgc/(ggc+y(3))/(ggc+y(3)))/((2*Nol*(ε0)*r1*((hol)-y(3))+
2*Ngc*ε0*tpm*hgc/(ggc+y(3))))^2/2/m -kl*y(3)/(m) - (visc*m/ρ/tpm/tPl + 4*Nol*visc*hol*r1/r3 +
16*2*Ngc*visc*(tpm^3)*hgc/((ggc+0)^3)+16*2*Ngc*visc*(tpm^3)*hgc/((ggc-0)^3)) * y(4)/(m) -
A*sin(ω*t) ;
```

References

[1] N. Action, A. Chawanda, and P. Luhanga, "Piezoelectric energy harvesting devices: an alternative energy source for wireless sensors," Smart Materials Research, vol. 2012, pp. 1-13, 2012.

[2] S. Roundy, P. K. Wright, and K. S. J. Pister, “Micro-Electrostatic Vibration-electricity Converters,” ASME International Mechanical Engineering Congress & Exposition, Proceedings of IMECE., pp. 487-496, 2002.

[3] J. A. Paradiso and T. Starner, “Energy Scavenging for Mobile and Wireless Electronics,” IEEE Pervasive Comput., vol. 4, pp.18-27, 2005.

[4] M. Strasser, R. Aigner, M. Franosch, and G. Wachutka, "Miniaturized thermoelectric generators based on poly-Si and poly-SiGe surface micromachining," Sensor Actuat A- Phys., vol. 97, pp. 535-542, 2002.

[5] S. Roundy, P. K. Wright, and J. Rabaey, “A Study of Low Level Vibrations as a Power Source for Wireless Sensor Nodes”, Comput Commun., vol. 26, pp. 1131–1144, 2003.

[6] S. Roundy, Energy Scavenging for Wireless Sensor Networks, Kluwer Academic Publishers, Boston, 2003.

[7] S. P. Beeby, R. N. Torah, M. J. Tudor, P. Glynne-Jones, T. O'Donnell, C. R. Saha, and S. Roy, "A micro electromagnetic generator for vibration energy harvesting," J. Micromech.Microeng., vol. 17, pp. 1257-1265, 2007.

[8] I. Kuehne, A. Frey, G. Eckstein, U. Schmid, and H. Seidel, "Design and analysis of a capacitive vibration-to-electrical energy converter with built-in voltage," In Solid-State Device Research Conference, Proceeding of the 36th European, IEEE, pp. 138-141, 2006.

[9] P. Wang, K. Tanaka, S. Sugiyama, X. Dai, X. Zhao, and J. Liu, “A micro electromagnetic low level vibration energy harvester based on MEMS technology,” Microsys. Technol., vol. 15, pp. 941–951, 2009.

[10] S. P. Beeby, M. J. Tudor, R. N. Torah, S. Roberts, T. O’donnell, and S. Roy, "Experimental comparison of macro and micro scale electromagnetic vibration powered generators," Microsys. Technol., vol. 13, pp. 1647-1653, 2007.

[11] D. Hoffmann, B. Folkmer, and Y. Manoli, “Fabrication, characterization and modeling of electrostatic micro-generators,” J. Micromech. Microeng.,vol. 19, pp. 1-11, 2009.

[12] Y. Arakawa, Y. Suzuki, and N. Kasagi, “Micro Seismic Power Generator using Electret Polymer Film,” Proc. PowerMEMS, pp. 187-190, 2004.

[13] V. Leonov, P. Fiorini, and C. Van Hoof, “Stabilization of Positive Charge in SiO2/Si3N4 Electrets,” IEEE Trans. Dielectr. Electr. Insul., vol. 13, pp. 1049-1056, 2006.

[14] T. Tsutsumino, Y. Suzuki, N. Kasagi, and Y. Sakane, “Seismic Power Generator Using High-Performance Polymer Electret”, 19th IEEE International Conference on MEMS, pp. 98-101, 2006.

[15] B. Jaffe, W. R. Cook, and H. Jaffe, Piezoelectric Ceramics, Academic, New York, 1971.

[16] K. A. Cook-Chennault, N. Thambi, and A. M. Sastry, "Powering MEMS portable devices-a review of non-regenerative and regenerative power supply systems with special emphasis on piezoelectric energy harvesting systems," Smart Mater. Struct., vol. 17, pp. 043001, 2008.

[17] P. X. Gao, J. Song, J. Liu, and Z. L. Wang. "Nanowire piezoelectric nanogenerators on plastic substrates as flexible power sources for nanodevices," Adv. Mater., vol. 19, pp. 67-72, 2006.

[18] M. P. Lu, J. Song, M. Y. Lu, M. T. Chen, Y.Gao, L. J. Chen, and Z. L. Wang, "Piezoelectric nanogenerator using p-type ZnO nanowire arrays," Nano lett., vol. 9, pp. 1223-1227, 2009.

[19] H. B. Fang, J. Q. Liu, Z. Y. Xu, L. Dong, L. Wang, D. Chen, B. C. Cai, and Y. Liu, "Fabrication and performance of MEMS-based piezoelectric power generator for vibration energy harvesting," Microelectr. J., vol. 37, pp. 1280-1284, 2006.

[20] Y. Jeon, R. Sood, J. Jeong, and S. Kim, "MEMS power generator with transverse mode thin film PZT," Sensor Actuat A-Phys., vol. 122, pp. 16-22, 2005.

[21] D. Shen, J. H. Park, J. H. Noh, S. Y. Choe, S. H. Kim, H. C. Wikle, and D. J. Kim, "Micromachined PZT cantilever based on SOI structure for low frequency vibration energy harvesting," Sensor Actuat A-Phys., vol. 154, pp. 103-108, 2009.

[22] M. J. Ramsay and W. W. Clark, "Piezoelectric energy harvesting for bio-MEMS applications," SPIE's 8th Annual International Symposium on Smart Structures and Materials. International Society for Optics and Photonics, pp. 429-438, 2001.

[23] X. Sheng, Y. Qin, C. Xu, Y. Wei, R. Yang, and Z. L. Wang, "Self-powered nanowire devices," Nat Nanotechnol., vol. 5, pp. 366-373, 2010.

[24] X. Sheng, Y. Wei, J. Liu, R. Yang, and Z. L. Wang, "Integrated multilayer nanogenerator fabricated using paired nanotip-to-nanowire brushes," Nano lett., vol. 8, pp. 4027-4032, 2008.

[25] S. Meninger, J. Mur-Miranda, R. Amirtharajah, A. Chandrakasan, and J. Lang, "Vibration-electric Energy Conversion," Very Large Scale Integration (VLSI) Systems, IEEE Transactions on, vol. 9, pp. 64-76, 2002.

[26] S. Roundy, Energy scavenging for wireless sensor nodes with a focus on vibration to electricity conversion, Diss. University of California, Berkeley, 2003.

[27] Soobum. Lee, and B. D. Youn, "A new piezoelectric energy harvesting design concept: multimodal energy harvesting skin," Ultrasonics, Ferroelectrics, and Frequency Control, IEEE Transactions on, vol. 58, pp. 629-645, 2011.

[28] F. D. Wall, M. A. Martinez, and J. J. Vandenavyle, "Corrosion behavior of a structural nickel electrodeposit," Microsys.Technol., vol. 11, pp. 319-330, 2005.

[29] T. Sterken, P. Fiorini, K. Baert, R. A. P. R. Puers, and G. A. B. G. Borghs, "An electret-based electrostatic μ-generator," In Transducers, Solid-State Sensors, Actuators and Microsystems, 12th International Conference on, IEEE, vol. 2, pp. 1291-1294, 2003.

[30] Y. Li, Z. Celik-Butler and D. P. Butler, “Design and optimization of an electrostatic micro-harvester for sensors applications,” in Proc. IEEE Sensors conf., Baltimore, MD, USA, pp. 1-4, 2013.

[31] I. E. Gonenli, Z. Celik-Butler and D. P. Butler, “Surface Micromachined MEMS Accelerometers on Flexible Polyimide Substrate,” IEEE Sensors. J., vol. 11, pp. 2318-2326, 2011.

[32] G. K. Fedder, "Simulation of microelectromechanical systems," PhD diss., University of California at Berkeley, 1994.

[33] W. C. Young and R. G. Budynas, Roark's formulas for stress and strain, McGraw-Hill, New York, 2002.

[34] W. Wai-Chi, A. A. Azid, and B. Y. Majlis, "Formulation of stiffness constant and effective mass for a folded beam," Arch. Mech., vol. 62, pp. 405-418, 2010.

[35] I. E. Gonenli, Failure assessment in aerospace systems via integrated multi-functional sensors, Diss. University of Texas at Arlington, Arlington, 2011

[36] H. K. Chang and Y. K. Kim, "UV-LIGA process for high aspect ratio structure using stress barrier and C-shaped etch hole," Sensor Actuat. A- Phys., vol. 84, pp. 342-350, 2000.

[37] H. Hammer, "Analytical model for comb-capacitance fringe fields," J. Microelectromech. Syst., vol. 19, pp. 175-182, 2010.

[38] T. Sterken, P. Fiorini, K. Baert, R. Puers and G. Borghs, “An electret-based electrostatic μ-Generator,” Prof. of TRANSDUCERS: 12th Int. Conf. on Solid-State Sensors, Actuators and Microsystems (Boston, MA 2003), vol. 2, pp. 1291–1294, 2003.

[39] F. Peano and T. Tambosso, “Design and optimization of a MEMS electret-based capacitive energy scavenger,” J. Microelectromech. Syst., vol. 14, pp. 429–435, 2005.

[40] D. Hoffmann, B. Folkmer and Y. Manoli, “Fabrication, characterization and modelling of electrostatic microgenerators,” J. Micromech. Microeng., vol.19, pp. 094001, 2009.

[41] G. J. Sheu, S. M. Yang, and T. Lee, “Development of a low frequency electrostatic comb-drive energy harvester compatible to SoC design by CMOS process,” Sensor Actut A-Phys., vol. 167, pp. 70–76, 2011.

[42] K. Ramadan and I. G. Foulds, "Fabrication of SU-8 low frequency electrostatic energy harvester," In Energy Aware Computing (ICEAC), 2011 International Conference on, IEEE, pp. 1-5, 2011.

[43] P. Basset, D. Galayko, A. M. Paracha, F. Marty, A. Dudka, and T. Bourouina, “A batch-fabricated and electret-free silicon electrostatic vibration energy harvester,” J. Micromech. Microeng., vol. 19, pp. 115025, 2009.

[44] R. J. Vullers, R. V. Schaijk, H. J. Visser, J. Penders, and C. V. Hoof, “Energy harvesting for autonomous wireless sensor networks,” IEEE Solid-State Circuits Mag., vol. 2, pp. 29-38, 2010.

[45] J. A. Paradiso and T. Starner, “Energy scavenging for mobile and wireless electronics,” IEEE Pervasive Comput., vol. 4, pp. 18-27, 2005.

[46] Z. L. Wang and W. Wu, "Nanotechnology-Enabled Energy Harvesting for Self-Powered Micro-/Nanosystems," Angew. Chem. Int. Ed., vol. 51, pp. 11700-11721, 2012.

[47] Z. L. Wang, "Towards Self-Powered Nanosystems: From Nanogenerators to Nanopiezotronics," Adv. Funct. Mater., vol. 18, pp. 3553-3567, 2008.

[48] M. A. Green, Third Generation Photovoltaics: Advanced Solar Energy Conversion, Springer, London, 2003.

[49] K. M. Coakley and M. D. McGehee, "Conjugated polymer photovoltaic cells," Chem.Mater., vol. 16, pp. 4533-4542, 2004.

[50] M. Strasser, R. Aigner, M. Franosch, and G. Wachutka, “Miniaturized thermoelectric generators based on poly-Si and poly-SiGe surface micromachining,” Sensor Actuat A-Phys., vol. 97, pp. 535-542, 2002.

[51] M. Ujihara, G. P. Carman, and D. G. Lee, "Thermal energy harvesting device using ferromagnetic materials," Appl. Phys. Lett., vol. 91, pp. 1-4, 2007.

[52] V. Gupta, A. Kandhalu, and R. R. Rajkumar, "Energy harvesting from electromagnetic energy radiating from AC power lines," Proceedings of the 6th Workshop on Hot Topics in Embedded Networked Sensors, 2010.

[53] D. F. Berdy, B. Jung, J. F. Rhoads, and D. Peroulis, "Wide-bandwidth, meandering vibration energy harvester with distributed circuit board inertial mass," Sensor Actuat A-Phys., vol. 188, pp. 148-157, 2012.

[54] T. Ning and F. S. Wei, "Multichannel coherence analysis of helicopter vibrations," Signal Processing, 2002 6th International Conference on, vol. 2, pp. 1774-1777, 2002.

[55] E. K. Reilly, L. M. Miller, R. Fain, and P. Wright, "A study of ambient vibrations for piezoelectric energy conversion," Proceedings of the Power-MEMS, pp. 312-315, 2009.

[56] S. Priya, "Advances in energy harvesting using low profile piezoelectric transducers," J. Electroceram., vol. 19, pp. 167-184. 2007.

[57] T. Sterken, P. Fiorini, K. Baert, G. Borghs, and R. Puers, “Novel design and fabrication of a MEMS electrostatic vibration scavenger,” Proc. PowerMEMS, pp. 18-21, 2004.

[58] P. Wang, K. Tanaka, S. Sugiyama, X. Dai, X. Zhao, and J. Liu, “A micro electromagnetic low level vibration energy harvester based on MEMS technology,” Microsyst. Technol., vol. 15, pp. 941-51, 2009.

[59] S. P. Beeby, M. J. Tudor, R. N. Torah, S. Roberts, T. O'Donnell, and S. Roy, "Experimental comparison of macro and micro scale electromagnetic vibration powered generators," Microsyst. Technol. vol. 13, pp. 1647-1653, 2007.

[60] Y. B. Jeon, R. Sood, J. H. Jeong and S. G. Kim, "MEMS power generator with transverse mode thin film PZT," Sensor Actuat A-Phys., vol. 122, pp. 16-22, 2005.

[61] Z. L. Wang and J. Song, "Piezoelectric nanogenerators based on zinc oxide nanowire arrays," Science, vol. 312, pp. 242-246, 2006.

[62] https://en.wikipedia.org/wiki/Zinc_oxide

[63] Z. L. Wang, "Nanogenerators for self-powered devices and systems," 2011.

[64] J. Anderson and C. G. Van de Walle, "Fundamentals of zinc oxide as a semiconductor," Rep. Prog. Phys., vol. 72, pp. 1-22, 2009.

[65] A. Bakin, A. El-Shaer, A. C. Mofor, M. Al-Suleiman, E. Schlenker, and A. Waag, "ZnMgO-ZnO Quantum Wells Embedded in ZnO Nanopillars: Towards Realisation of Nano-LEDs," Phys. Stat. Sol.(c), vol. 4, pp. 158–161, 2007.

[66] Y. B. Li, Y. Bando, and D. Golberg, "ZnO nanoneedles with tip surface perturbations: Excellent field emitters, " Appl. Phys. Lett., vol. 84, pp. 3603-3605, 2004.

[67] B. Y. Oh, M. C. Jeong, T. H. Moon, W. Lee, J. M. Myoung, J. Y. Hwang and, D. S. Seo, "Transparent conductive Al-doped ZnO films for liquid crystal displays, " J. Appl. Phys., vol. 99 ,pp. 124505-1-124505-4, 2006.

[68] H. T. Wang, B. S. Kang, F. Ren, L. C. Tien, P. W. Sadik, D. P. Norton, S. J. Pearton, and J. Lin, "Hydrogen-selective sensing at room temperature with ZnO nanorods, " Appl. Phys. Lett., vol. 86, pp. 243503-1-24503-3, 2005.

[69] L. C. Tien, P. W. Sadik, D. P. Norton, L. F. Voss, S. J. Pearton, H. T. Wang, B. S. Kang, F. Ren, J. Jun, and J. Lin, "Hydrogen sensing at room temperature with Pt-coated ZnO thin films and nanorods, " Appl. Phys. Lett.,vol. 87, pp. 222106-1-222106-3, 2005.

[70] M. Sui, P. Gong, and X. Gu, "Review on one-dimensional ZnO nanostructures for electron field emitters," Front. Optoelectron., vol. 6, pp. 386-412, 2013.

[71] http://groups.ist.utl.pt/rschwarz/rschwarzgroup_files/PLD_files/PLD.htm

[72] L. Vayssieres, “Growth of arrayed nanorods and nanowires of ZnO from aqueous solutions,” Adv. Mater., vol. 15, pp. 464-466. 2003.

[73] S. Xu, C. S. Lao, B. Weintraub and Z. L. Wang, "Density-controlled growth of aligned ZnO nanowire arrays by seedless chemical approach on smooth surfaces," J. Mater. Res., vol. 23, pp. 2072-2077, 2008.

[74] S. Baruah and J. Dutta, “Hydrothermal growth of ZnO nanostructures,” Sci. Technol. Adv. Mater. , vol. 10, pp. 1-18, 2009.

[75] A. Sugunan, H. C. Warad, M. Boman,and J. Dutta, “Zinc oxide nanowires in chemical bath on seeded substrates: Role of hexamine,” J. Sol Gel Sci. Technol., vol. 39, pp. 49-56, 2006.

[76] Y. Gao and Z. L. Wang, "Electrostatic potential in a bent piezoelectric nanowire. The fundamental theory of nanogenerator and nanopiezotronics," Nano lett., vol. 7, pp. 2499-2505, 2007.

[77] Z. Gao, J. Zhou, Y. Gu, P. Fei, Y. Hao, G. Bao, and Z. L. Wang, “Effects of piezoelectric potential on the transport characteristics of metal-ZnO nanowire-metal field effect transistor,” J. Appl. Phys., vol. 105, pp. 113707-1-113707-6, 2009.

[78] A. Kaushik, H. Kahn, and A. H. Heuer, "Wafer-level mechanical characterization of silicon nitride MEMS, " J. Microelectromech. Syst., vol. 14, pp. 359-367, 2005.

[79] Z. Han, S. L, J. Chu, and Y. Chen, "Controlled growth of well-aligned ZnO nanowire arrays using the improved hydrothermal method," J. Semicond., vol. 34, pp. 1-6, 2013.

[80] Y. Wei, W. Wu, R. Guo, D. Yuan, S. Das, and Z. L. Wang, “Wafer-scale high-throughput ordered growth of vertically aligned ZnO nanowire arrays,” Nano letters, vol. 10, pp. 3414-3419, 2010.

[81] B. P. Nabar, Z. Celik-Butler, and D. P. Butler, "Self-powered, tactile pressure sensing skin using crystalline ZnO nanorod arrays for robotic applications," in Proc. IEEE Sensors conf., Baltimore, MD, USA, pp. 1-4, 2013.

[82] B. P. Nabar, Z. Celik-Butler, and D. P. Butler, "Self-Powered Tactile Pressure Sensors Using Ordered Crystalline ZnO Nanorods on Flexible Substrates Towards Robotic Skin and Garments," IEEE Sensors. J., vol. 15, pp. 63-70, 2015.

[83] J. K. Luo, M. Pritschow, A. J. Flewitt, S. M. Spearing, N. A. Fleck, and W. I. Milne, "Effects of process conditions on properties of electroplated Ni thin films for microsystem applications," J. Electrochem. Soc., vol. 153, pp. D155-D161, 2006.

[84] Y. Li, Z. Celik-Butler, and D. P. Butler, “A hybrid electrostatic micro-harvester incorporating in-plane overlap and gap closing mechanisms,” J. Micromech. Microeng, vol. 25, pp. 1-10, 2015.

[85] G. Zhu, R. Yang, S. Wang, and Z. L. Wang, "Flexible high-output nanogenerator based on lateral ZnO nanowire array," Nano lett., vol. 10, pp. 3151-3155, 2010.

[86] B. Kumar, K. Y. Lee, H. K. Park, S. J. Chae, Y. H. Lee, and S. W. Kim, "Controlled growth of semiconducting nanowire, nanowall, and hybrid nanostructures on graphene for piezoelectric nanogenerators," Acs Nano., vol. 5, pp. 4197-4204, 2011.

[87] C. T. Huang, J. Song, W. F. Lee, Y. Ding, Z. Gao, Y. Hao, L. J. Chen, and Z. L. Wang, "GaN nanowire arrays for high-output nanogenerators," J. Am. Chem. Soc., vol. 132, pp. 4766-4771, 2010.

[88] C. Chang, V. H. Tran, J. Wang, Y. K. Fuh, and L. Lin, "Direct-write piezoelectric polymeric nanogenerator with high energy conversion efficiency," Nano let., vol. 10, pp. 726-731, 2010.

[89] H. U. Kim, V. Bedekar, R. A. Islam, W. H. Lee, D. Leo, and S. Priya, "Laser-machined piezoelectric cantilevers for mechanical energy harvesting," Ultrasonics, Ferroelectrics, and Frequency Control, IEEE Transactions on, vol.55, pp. 1900-1905, 2008.

[90] D. Shen, J. H. Park, J. H. Noh, S. Y. Choe, S. H. Kim, H. C. Wikle, and D. J. Kim, "Micromachined PZT cantilever based on SOI structure for low frequency vibration energy harvesting," Sensor Actua. A-Phys., vol. 154, pp. 103-108, 2009.

[91] J. C. Park, D. H. Lee, J. Y. Park, Y. S. Chang, and Y. P. Lee, "High performance piezoelectric MEMS energy harvester based on D33 mode of PZT thin film on buffer-layer with PBTIO3 inter-layer," In Solid-State Sensors, Actuators and Microsystems Conference, IEEE, pp. 517-520, 2009.

[92] W. K. G. Seah, Z. A. Eu, and H. P. Tan, "Wireless sensor networks powered by ambient energy harvesting (WSN-HEAP)-Survey and challenges," In Wireless Communication, Vehicular Technology, Information Theory and Aerospace &

Electronic Systems Technology, Wireless VITAE 2009. 1st International Conference on. IEEE, pp. 1-5, 2009.

Biographical Information

Yi Li was born in Shanxi, China. Yi Li received her B.E in Microelectronics and Solid-State Electronics from the University of Electronic Science and Technology of China in 2001. She received her M.S in Microelectronics from the Peking University in 2004. She received her Ph.D in Electrical Engineering from the University of Texas at Arlington in 2015.

Her research interests include MEMS mechanical vibrational micro energy harvester design and fabrication.